SIMULATIONS OF HIGH-LATITUDE IONOSPHERE-MAGNETOSPHERE REGION PLASMA DENSITY STRUCTURES AND THE AlFVÉN WAVES EFFECTS

by

FAJER BITAR JAAFARI

Presented to the Faculty of the Graduate School of

The University of Texas at Arlington in Partial Fulfillment

of the Requirements

for the Degree of

DOCTOR OF PHILOSOPHY

THE UNIVERSITY OF TEXAS AT ARLINGTON

August 2009

ACKNOWLEDGEMENTS

I first have to thank God for offering me what I needed to peruse my goals of earning of a Doctoral Degree in physics, thanks for providing me with health and have a big healthy family.

I would like to thank my husband Khaldoun for his constant support and love through out my study. He gave me the strength when I was weak and tired. He gave me love and hope when I was overwhelmed and exhausted, his presence by my side allowed me to reach this milestone.

Thanks to my oldest two daughters Hana and Deena for their patience and support. At their tender age, when they need mom the most, they did provide me with needed space and time to invest in my studies.

My youngest two kids Rami and Selma, although oblivious to what mom is attempting to do, their innocence and peace shown in their eyes, emphasized my priorities in life, pursuit of science while raising a family.

I would like to thank my late advisor Dr. James Horwitz for his teachings, opening the door to space physics, providing all the tools to conduct my research work and propelling me to meet all the required standards during the course of my doctoral study. Thanks to Dr. Ramon Lopez for shepherding my research and his effort to motivate and encourage me to complete the work.

Thanks to my committee members, Dr. Sam Jones for his guidance, support, invaluable advice and patience. Also, thanks to Dr. Alex Weiss, Dr. Andy White and Dr. Manfred Cuntz for their support and interest in my research.

Thanks to Dr. Wen Zeng for his support and his help to find solutions to numerous computing and physics problems. Thanks to Dr. John Fry for his guidance, continuous support and his belief in my ability and ambitions.

Thanks to Mrs. Taeko Horwitz for her encouragement, kindness and support as a student of her late husband. Also, thanks to my entire friends at the Physics department for their love and support.

I want to express my love and gratitude to my Mom and Dad for their constant support and love, for their teaching of the importance of education and the pursuit of knowledge. Thanks to my sisters for their constant motivation to complete my PhD program.

Finally I would like to acknowledge the fact that this work was completed under financial support by NASA grant NNG05GF67G, and NSF grant ATM-0505918 to the University of Texas at Arlington. Also, thanks to CDA website for providing all the data and plots that helped my research work.

July 2, 2009

ABSTRACT

SIMULATIONS OF HIGH-LATITUDE IONOSPHERE-MAGNETOSPHERE
REGION PLASMA DENSITY STRUCTURES AND
THE AlFVÉN WAVES
AFFECTS

Fajer Bitar Jaafari, PhD

The University of Texas at Arlington, 2009

Supervising Professor: Ramon Lopez

O^+ density structures in the polar cap ionosphere-magnetosphere region near 6000 km altitude have been observed with numerous spacecraft, with O^+ densities ranging from above 10 cm^{-3} to lower than 0.01 cm^{-3}. Regions with densities in the low range have been referred to as O^+ density troughs [*Zeng et al*., 2004], or ion depletion zones [*Horita et al*., 1993]. Regions with high O^+ densities are likely caused by processes such as soft auroral electron precipitation and transverse wave heating. In this simulation work, we use the UT Arlington Dynamic Fluid-Kinetic (DyFK) ionospheric plasma transport model to model O^+ density profiles and other aspects of the ionosphere-magnetosphere plasma distribution under various conditions for two different studies. The first type of situation concerns the O^+ troughs in the polar cap, which were observed by the Thermal Ion Dynamics Experiment (TIDE) on the Polar spacecraft. We use solar wind parameters and IMF conditions as inputs to drive a time-varying high-latitude electric potential model [*Weimer*, 2001]. We also incorporate auroral processes involving the effects of

soft electron precipitation and wave-driven transverse ion heating, we simulate the ionosphere-magnetosphere plasma transport and the associated O^+ bulk parameter profiles of different flux tubes convecting in the high-latitude region. The simulation results for realistic parameters and specific geophysical conditions agree reasonably well with the O^+ density variations observed. The second study involves examination of the effects of inertial Alfvén waves propagating along auroral field lines producing parallel electric fields which accelerate auroral precipitating electrons. We examine the propagation of Alfvén waves within O^+ auroral ionosphere-magnetosphere density profiles. For the Alfvén wave description, a linear one-dimensional Gyro-Fluid code [*Jones et al*., 2003] is used, in which electron inertia, electron pressure gradient and finite ion gyroradius effects are incorporated. This Alfvén wave propagation code determines the characteristics of propagating Alfvén waves which generate the inertial parallel electric field responsible for energizing electrons. A test particle model developed by *Su et al* [2004] is then used to simulate the response of a distribution of electrons to these Alfvén wave electric fields. The integrated energy flux of the resulting precipitating electrons will be obtained to link back with DyFK model, which shows the effect of such Alfvénic electrons on the plasma evolution in the DyFK code and on Alfvénic phase speed profile.

TABLE OF CONTENTS

LIST OF ILLUSTRATIONS

Figure Page

LIST OF TABLES

CHAPTER 1

INTRODUCTION

1.1 Overview

Our Earth has a strong internal dipole magnetic field that is modified by the solar wind to create a huge region called the magnetosphere. The solar wind is fully ionized plasma that is capable of penetrating the earth's upper magnetosphere boundaries through the magnetosheath layer supplying it with hot magnetized ions and electrons. The upper neutral Earth atmosphere is ionized by the Sun's ultra violet radiation creating the ionosphere region that is coupled to the magnetosphere region. The ionosphere is divided into different conducting layers with different plasma densities; its maximum is about the *F* layer (upper part of this region) [*Kivelson and Russell*, 1997].

The ionosphere-magnetosphere region consists of several parts that created by the magnetic field topology. At the upper latitudes, the open field lines area or the open polar cap, create what we call the polar wind [e.g., *Ganguli*, 1996]. The closed field lines are the auroral field lines. At the region of the auroral oval where the open magnetosheath layers are, the cusp is formed. The cusp is a highly confined region which provides a direct entry for the dense energetic magnetosheath plasma into the magnetosphere [e.g*., Reiff et al*., 1977; *Marklund et al*., 1990; *Yamauchi et al*., 1996]. At the low latitude of the cusp, the cleft ion fountain is located [e.g., *Arnoldy et al.,* 1996]. The magnetosphere-ionosphere configuration and dynamics generate variable plasma densities, the density profiles at any region or altitude can be significantly altered due to the constant dynamics in the sun-earth complex system [e.g., *Russell et al.,* 1980].

The plasma density structures in the polar cap and the aurora regions have been of great interest to space scientists for many years. Still, there is a need to better understand the various

physical processes and dynamics governing the ionosphere-magnetosphere coupling region where the occurring events are ever changing.

Extensive research has confirmed that the ionosphere is a major plasma supplier to the magnetosphere system through ion transport processes [e.g., *Chappell et al.,* 1987*; Horwitz,* 1982; 1985; 1997*; Moore et al.,* 1986a; b; *Moore and Delcourt*., 1995, *Ganguli.*, 1996, *Horwitz and Moore*, 1997]. The topside ionosphere *F* region environment is where the majority of H^+, He^+, and O^+ ion are produced. The ion outflow along the magnetic field lines influences the ions density profiles along the magnetic field lines. Observation show that the plasmasphere at about (2-5 R_E altitude) is composed mainly of H^+ with smaller quantities of O^+ and He^+ [e.g., *Horwitz et al*., 1984; *Comfort et al*., 1988; *Craven et al*., 1997; *Lemaire and Gringauz*, 1998]. However, O^+ is the dominant ion species in the ionosphere up to about 4000 km altitude [e.g., *Chandler et al*, 1991]. Simulations by *Nsumei et al.* [2003] showed that the plasma densities from 1.4 - 5 R_E altitude are enhanced with increasing geomagnetic activity. The plasma densities vary as result of corotation and convection due to the corotation electric field and the convection electric field respectively. The ionosphere dynamics results in different initial plasma densities and pressures for different flux tubes, leading ultimately to a significant variation in ion outflow fluxes. Figure 1.1 shows different physical processes responsible for particles outflow that occur in both, the nominal polar cap and the auroral region.

1.2 Ionosphere-Magnetosphere Ion Outflow Processes

As mentioned before, there are different plasma regions divided into sectors including the polar wind, the cusp/cleft ion fountain and the auroral region. Observations have shown that the auroral oval is characterized by mostly upward moving heavy ions but downward moving in the nominal polar cap region [e.g., *Lorance et al*., 1991]. At the polar cap topside latitudes where the classical polar wind is the dominant feature, the plasma outflow is supersonic and is

composed mostly of Hydrogen [e.g., *Ganguli*, 1996]. However, the O^+ ion flow is predominantly downward in this region [e.g., *Heelis et al*., 1992]. Satellite observations have indicated the presence of a considerable amount of thermal or superathermal O^+ ions in the polar cap magnetosphere [e.g., *Horwitz et al.,* 1992*; Moore et al.,* 1985]. These polar cap ionosphere-magnetosphere O^+ ions are generally considered to originate in the dayside cleft/cusp region and to be transported into the polar cap by antisunward convection [e.g., *Waite et al*, 1985].

There are specific mechanisms involved in ions upflow/outflow, to high altitudes. The transition of the plasma from the O^+ dominant region (ionosphere) to H^+ dominant region (magnetosphere) has been extensively studied using different simulation models to understanding the mechanisms of plasma outflow [e.g., *Shunk and Sojka*., 1997; *Mitchell et al.,* 1992; *Wu et al*., 2000; *Tu et al*., 2004]. It has been found that O^+ ions travel upward at first, but they cannot escape the gravitational barrier unless they are heated to gain sufficient energy (10.5 eV). It is been suggested that the upward acceleration of O^+ ions is driven by the effects of ambipolar electric fields that are associated with enhanced electron temperatures and density gradients, or by pressure gradients [e.g., *Wilson*, 1994]. However, the O^+ ions cannot escape the gravitational barrier with only the electric field force. To energize and enhance the O^+ outflow, additional mechanisms were introduced such as frictional heating due to collisions between convecting ions and neutrals, electrostatic potential drops caused by photoelectron effects [e.g., *Tam et al*., 1995; *Su et al*., 1998a] , centrifugal force effects [*Horwitz et al*., 1994], mirror forces and other high-latitude processes. Another important factor is the solar illumination which is strongly effects the plasma production. The increase of the ionosphere temperature by EUV along with Joule heating and electron precipitation leads to enhancement in cold O^+ ions. The ion velocities are higher in the dayside than the night side as seen in Polar/TIDE observations [e.g., *Su et al*, 1998a]. Also, the outflow of O^+ ions is a response primarily to high altitude dynamics, the wave-particle interaction due to cyclotron-resonant interaction with the broad band electrostatic ELF [*Ganguli et al*., 1994; *Norqvist et al.*, 1998; *Yau*

and Andre, 1997, 1998]. The ion transverse wave heating events are restricted to the auroral region and observed over the auroral oval. Such waves were reported as a broadband electrostatic ELF, and electromagnetic waves which include Alfvén waves [e.g., *Chaston et al.*, 1999]. The low frequency Alfvén waves were observed in the aurora region propagating along magnetic field lines due to many processes such as instability and field-aligned currents [*Knudsen et al*., 1992, 1996; *Wahlunt et al.*, 1994; *Aikio et al*., 1996]. FAST observations showed an association between propagating Alfvén waves and ion out flow fluxes [e.g., *Chaston et al.,* 2002, 2004]. Dispersive Alfvén waves have been observed and studied extensively. These waves are associated with downward energized electron fluxes along the field line where they constantly transport energy from the magnetosphere to the ionospheric auroral oval [e.g., *Hasegawa*, 1976; *Goertz and Boswell*, 1979, *Wygant et al*., 2000; *Chaston et al.*, 2002]. This is discussed in more detail in sections 1.4-1.5.

The rate and amount of O^+ ion production on the other hand, affects the formation and production of H^+ ions. The source of H^+ as the main element of polar wind is the charge exchange reaction $O^+ + H \leftrightarrow O + H^+$. Thus the H^+ ion outflows are not influenced by the energy inputs or the solar cycle [*Moore et al*., 1999a] but are primarily affected by existing O^+ density in the *F* region.

In summary, ion outflow from the ionospheric region is affected by a variety of physics processes that change continuously the dynamics and characteristics of the magnetosphere system. That in turn causes response from the magnetosphere back into the ionosphere. Thus the system is highly coupled in a non-linear fashion. In this dissertation we will examine just one aspect of this coupled system, and discuss some of the factors that control ion outflow.

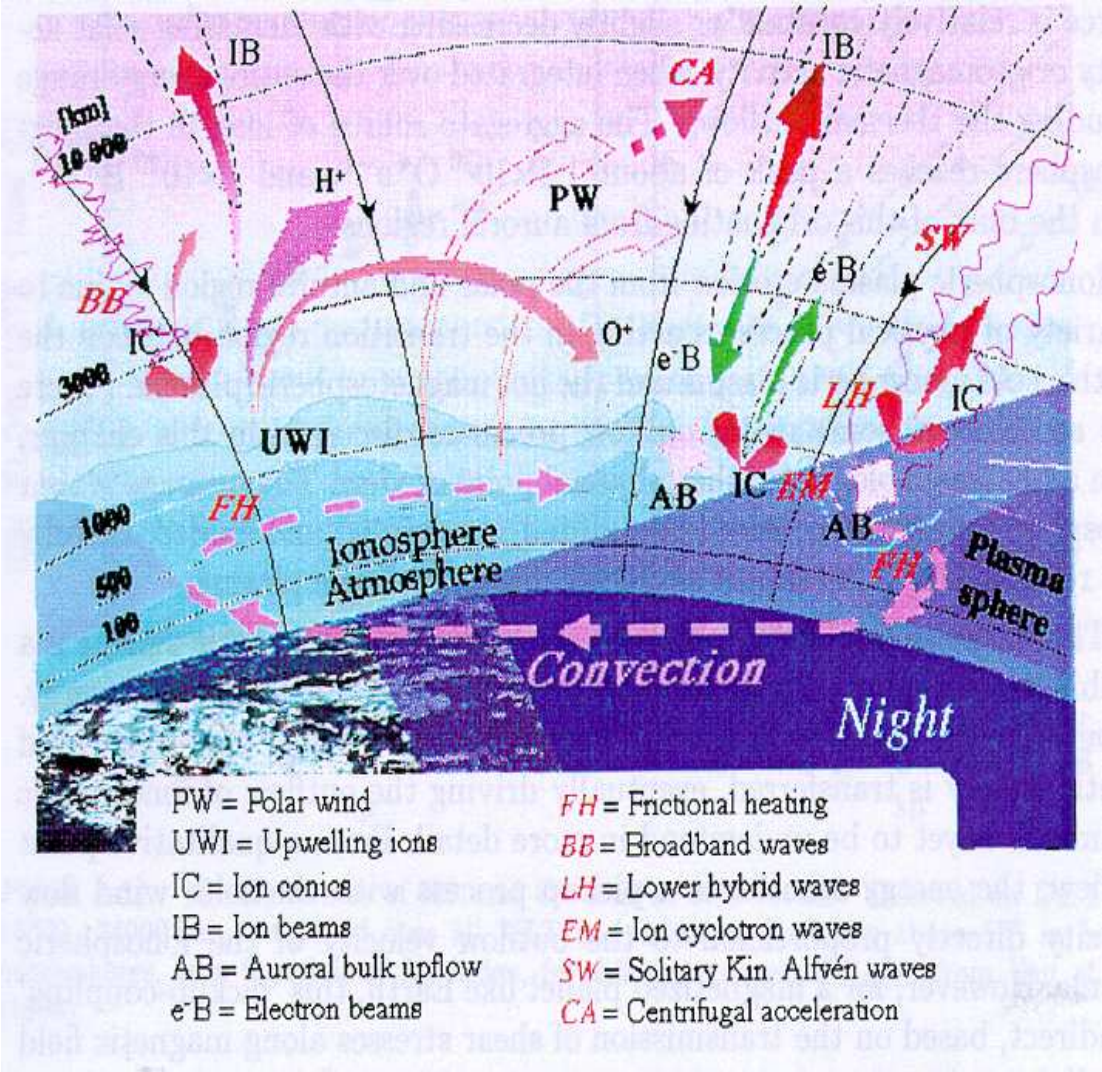

Figure 1.1 Schematic summary and categories of ions outflows processes in the polar cap magnetosphere- ionosphere regions [*By R. Lundin, in Moore et al*., 1999a].

1.3 Ionosphere-Magnetosphere Density Structures at High Latitudes

The plasma density in the polar cap topside ionosphere-magnetosphere coupling region is influenced by a variety of geophysical conditions, such as magnetic activity level, solar illumination and the characteristics of the cleft ion fountain. Akebono observations have indicated higher ion temperatures and parallel flow velocities in the dayside than in the nightside [*e.g., Abe et al.,* 1993; *Yau et al*., 1995]. Related results on the day/night asymmetries in ion densities and velocities were seen in observations by the Thermal Ion Dynamics Experiment (TIDE) on the Polar satellite, in which *Su et al*. [1998b] confirmed that the cleft ion fountain is the principal source for O^+ in the polar cap magnetosphere. In addition, *Stevenson et al*. [2001] found that across the southern polar region at altitude ~5000 km that O^+ parallel flows on auroral field lines are upward, while being downward on polar cap flux tubes whose *F*-region portions were in dark, non-auroral locations (see Figure 1.2). Simulation studies by *Schunk and Sojka* [1989; 1997] predicted a low ion density region, located in the magnetic latitude range of 70-90 degrees on the nightside of the polar cap, and extending from the F region to the topside ionosphere-magnetosphere coupling region. The ion depletion zones reported by *Horita et al*. [1993] were primarily located in the nightside region of the polar cap magnetosphere at invariant latitudes above 70º and altitudes between 8000 and 10,000 km. The statistical study by *Zeng et al* [2004] indicated that the occurrence of the O^+ density troughs over the polar cap region at 5000 km altitude could be influenced by factors such as the solar wind dynamic pressure, such that the trough occurrence decreased with increasing solar wind dynamic pressure, and the trough occurrence was observed to increase for decreasing solar illumination. However, the trough occurrence was found to be essentially independent of the K_p index as well as the Interplanetary Magnetic Field (IMF) B_y and B_z conditions. In the *Horita et al.* [1993] and *Zeng et al.* [2004] works, multiple mechanisms or geophysical conditions were discussed in connection with the formation of the low O^+ ion densities in the polar cap region. *Horita et al.* [1993] suggested that the ion depletion zones

might be caused by convection vortices which could form during magnetically quiet periods, where recombination of ions and electrons in a darkened *F* region and topside ionosphere could proceed for extended intervals. *Zeng et al*. [2004] suggested that effects of the $E \times B$ vertical component and the recombination of ions and electrons in darkened *F* region source locations might contribute to the formation of the observed O^+ density trough.

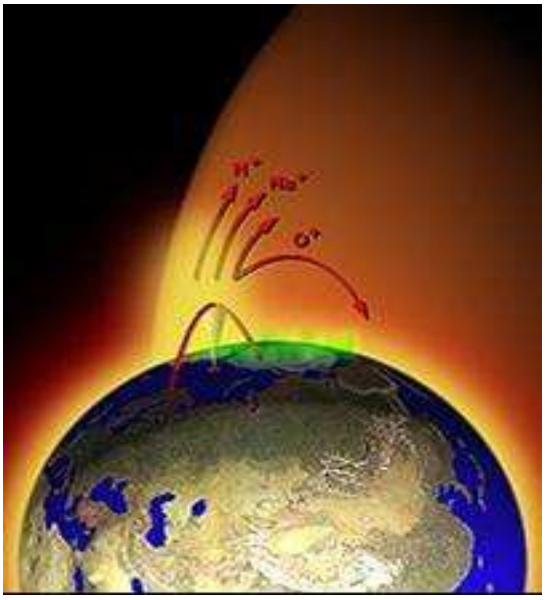

Figure 1.2 Schematic of the cleft ion fountain. The Cleft Ion Fountain may be the principal source of O^+ in the polar cap ionosphere-magnetosphere coupling region. [http://science.nasa.gov/ssl/pad/sppb/Scifer/].

1.4 Alfvén Waves

Alfvén waves carry energy into the ionosphere in the auroral oval [*Wygant et al*., 2000]. This energy could be transported to the surrounding plasma and converted to kinetic energy manifested in electron acceleration [e.g., *Thompson and Lysak.*, 1996**;** *Andersson et al.,* 2002; *Kletzing and Hu.,* 2001**;** *Chaston et al.,* 1999]. Exploring the roles of the dispersive Alfvén waves in particle acceleration and transport of energy down to the ionosphere was the motivation for numerous investigations. It has been demonstrated that under certain conditions, the propagating Alfvén wavelength projection perpendicular to the magnetic field (B_0) was of an order of an ion Gyro-Fluid or less (kinetic region) a parallel electric field $E_{||}$ could be generated [e.g., *Hasegawa.*, 1976]. Also, when the electron pressure gradient and electron inertia effects dominant (inertial region), the Alfvén wave can sustain a parallel electric field $E_{||}$ [*Goertz and Boswell.,* 1979; *Lysak and Carlson.,* 1981; *Lysak and Lotko.,* 1996]. This $E_{||}$ drives the electron acceleration downward to result in field-aligned electrons with super thermal fluxes [e.g., *Kletzing and Hu.,* 2001**;** *Chaston et al.,* 2001; 2002; *Anderson et al*., 2002].These accelerated electrons may produce ionization and thermal plasma heating as well as power the auroral luminosity forming one of earth's aurora regions at the high polar cap as shown in Figure 1.3 [e.g., *Su et al*., 2003]. The energetic down streaming electrons that carry energy form the upper aurora region (from 10 eV up to 1keV) have been observed and investigated [e.g., *Wygant et al*., 2000; *Knudsen and Wahlund.,* 1998; *Lotko et al*., 1998; *Hallinan et al*., 2001; *Chaston et al*., 2003]. Observations show that Alfvénic electron fluxes consist of electron bursts events where Alfvén waves accelerate electrons downward. However, the electron velocities might exceed the Alfvén speed and their distribution functions will be modified. The data showed also that the magnitude of $E_{||}$ is related to the existing physical quantities such as the surrounding plasma

environment, electron skin depth, Alfvén phase speed, perpendicular wave number ($k_\perp$) and the electric potential difference [e.g., *Stasiewicz et al*., 2000]. This $E_{||}$ can be given by

$$E_{\|} = -i\,k_{\|}\phi\left(1-\frac{\omega^2}{V_A^2 k_{\|}^2}\right) \approx -i\,k_{\|}\phi\left(\frac{k_\perp^2\lambda_e^2 - k_\perp^2\rho_s^2}{1+k_\perp^2\lambda_e^2}\right) \tag{1.1}$$

where V_A is the MHD Alfvén speed $\left(V_A = B \Big/ \sqrt{m_i n_i \mu_0}\right)$ (1.2)

and the ion acoustic gyroradius $\left(\rho_s = \sqrt{m_i T_e \Big/ e^2 B^2}\right)$ (1.3)

and the electron skin depth is $\left(\lambda_e = \sqrt{\frac{m_e}{e^2 \mu_0 n_e}}\right)$ (1.4)

Here m_i and n_i are the ion's mass and density respectively, n_e is the electron's density, μ_0 is permeability for vacuum and B is the background magnetic field.

Stasiewicz [2000] stated that, the $k_\perp$ leads to spreading of the wave energy across the magnetic field lines. This energy is significant and carried into the auroral oval expressed by Poynting flux propagating downward along the auroral field lines. *Chaston* [2003] showed that wave Poynting flux magnitude decreases with altitude where it converts to downgoing electron energy flux. However, the electron acceleration is also strongly dependent on the composition of the plasma and its density variation with altitude [*Kletzing and Hu.,* 2001; *Chaston et al*., 2000]. Therefore, the density structure plays a critical role of shaping Alfvén wave phase speed [e.g., *Lysak et al* 1998; *Su et al.,* 2004], where it could be responsible for generating the proper conditions and location of the electron burst. Furthermore, detailed studies and direct comparison between observations and simulations showed a link between Alfvén wave's propagation and energized ion out flows where the Alfvén wave frequency was smaller than the

encountered ion gyrofrequency [e.g., *Thompson and Lysak*., 1996; *Lotko et al* ., 1998; *Clark and Seyler*, 1999; *Su et al*, 2001].

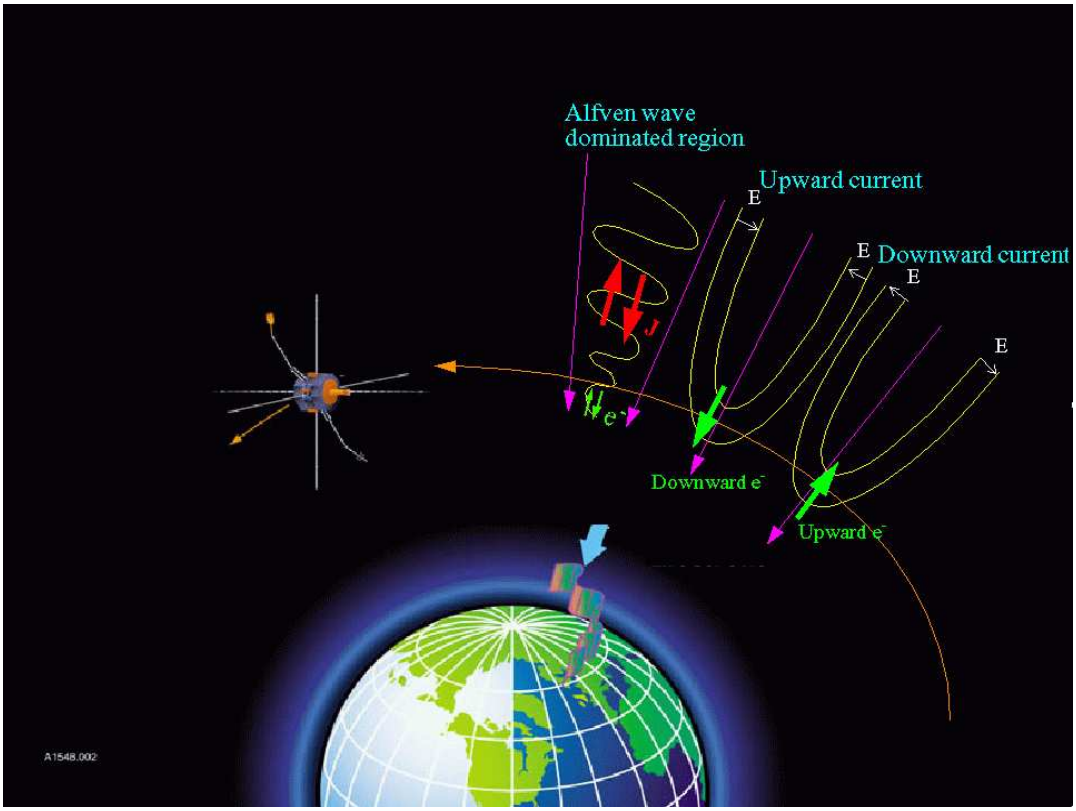

Figure 1.3 The three regions of the Earth's aurora at the high polar cap conducted by FAST Satellite. This FAST satellite picture was published on the cover of the special GRL issue Vol. 25, Num 12, 1998. Also was published by [*Su et al., JGR, V* 108, A2, 1094, doi: 10.1029/2002JA009247, 2003].

1.5 Alfvén Waves Electron Energization and Density Profile Evolution

Alfvén waves can be launched in the magnetosheath by different mechanisms, for example, a flow of sheared plasma moving across the background magnetic field or through electron/plasma density perturbation [*Stasiewicz et al.,* 2000]. In this case, the magnitude of the perturbed density gradient will be a factor in determining the perpendicular amplitude of the Alfvén wave which in turn would control the aspects of the generated parallel electric field. *Chaston et al* [2004] reported that the bulk oxygen energies or their transverse temperatures may exceed 100 eV. This observation/analysis show an association between the propagation of Alfvén waves, the electron heating/burst and the increase in O^+ ion outflow. Also, FAST observations (at about 4000 km altitude) show an association between ion heating and small scale propagating Alfvén waves [e.g., *Knudsen and Wahlund.,* 1998]. They reported conics of ions especially oxygen began at ionospheric altitudes which suggest that these ions might receive continuous heating as they elevate along the field line [*Stasiewicz et al*., 2000]. Energy measurements suggest an acceleration of the O^+ ions where their upstream velocity increased besides their energy fluxes during the same time interval of Alfvén wave propagation [e.g., *Chaston et al.*, 2002; 2003].

1.6 Objectives of This Dissertation

In this research work, we present the results of two main parts; the first one is an investigation of O^+ densities troughs observed in the southern polar cap region by Polar/TIDE about 6000 km altitude. The simulation results show the production of O^+ densities the ionosphere-magnetosphere coupling region under specific geophysical conditions on the following four dates: December 02 1997, August 02 1998, August 20 1998 and June 26 1998. We compare these simulation results with the relevant Polar/TIDE observations. The

ionospheric plasma transport simulations were conducted with the UT Arlington Dynamic Fluid-Kinetic (DyFK) model [e.g., *Estep et* al., 1999; *Wu et al*., 1999, 2002; *Tu et al*, 2004].

The second part is an investigation of Alfvén waves formed by different density profiles that had been generated by DyFK model. The properties of the produced $E_{||}$ generated by the Gyro-Fluid model [*Jones*, 2004] had different physical effects on different electron temperatures along the ionosphere-magnetosphere field line. The behavior of these electrons, generated by test particle code [*Su et al*, 2004], produced an evolution of the O^+ ions densities and their out flows development in the auroral region. The Alfvén phase speed was also evolving in the ionosphere-magnetosphere region.

We designed the Alfvén waves study by employing three models working in iteration. The Gyro-Fluid code, test particle method and DyFK model.

CHAPTER 2

OBSERVATIONS

Many investigations have been made to understand the nature of the physical processes involved in the polar cap ionosphere-magnetosphere regions. Understanding the characteristics of the polar wind and aurora plasma flow is very important to reveal the complexity of the spatial and temporal variation in plasma and its density structures. Direct observations over the polar cap are a significant source of information to investigate the plasma dynamics and its transport along the magnetic field lines.

A significant amount of observational evidence indicates that, the top side ionosphere/*F* region serves as primary source of thermal plasma to the magnetosphere [e.g., *Horwitz et al.*, 1982, 1995; *Shelley et al*., 1982; *Moore et al*., 1986; *Chappell et a*l., 1987; *Ganguli,* 1996]. In addition, day-night asymmetries have been revealed in the ion bulk parameters such as ion velocities and densities [e.g., *Abe et al*., 1993; *Yau et al.*, 1995, *Su et al*., 1998a]. The study of ion flow (especially O^+) and density structures in the upper latitudes have been of great interest because of the mass loading of the magnetosphere change its characteristics. Observations report that these heavy ions exhibit upwelling motion resulting in various processes in regions like the cleft ion fountain/aurora but downgoing flow in the polar cap [e.g., *Horwitz*, 1984; *Chandler,* 1995; *Tsunoda et al*., 1998; *Horwitz and Lokwood*, 1985]. This produces a high variation in O^+ ion density structures across the polar cap. Polar/TIDE observations of O^+ ions ~ 5000 km reported a decline in their densities over the polar cap but the O^+ ion density tend to increase in the cusp/aurora regions [e.g., *Moore et al.,* 1995*. Su et al,* 1998a]. However, significant declines in O^+ densities over the polar cap have been reported, showing segments of O^+ density depletion and have been referred to as O^+ density troughs [*Zeng et al*, 2004].

Observations and simulations have shown that the increase in O^+ ion density in the auroral region is associated with various energization mechanisms that lead to an increase in O^+ velocities and outflow [e.g., *Su et al,* 1998b], which could be linked directly to soft electron precipitations [e.g., *Tu et al*, 2004], and Broad Band Extremely Low Frequency (BBELF) waves [*Andre and Yau*, 1997]. Observation missions have been launched to investigate the role of the BBELF waves in ion out flow over the polar cap. The studies have identified that these waves besides electromagnetic waves exist over both, the day side and night side aurora region. Over that range, electromagnetic Alfvén waves were included as small scale dispersive waves [e.g., *Hasegawa*, 1976; *Goertz and Boswell*, 1979].

In the next two sections we are going to discus observations of the O^+ density structures revealing four trough cases or very low O^+ ion densities lower than 0.01 cm^{-3} [*Zeng et al*., 2004]. The second section will consider the observations that present evidence of the existence Alfvén waves throughout the auroral oval and role of Alfvén waves in ionospheric plasma dynamics.

2.1 Observations of O^+ Density Troughs

Spacecraft-based in situ observations have shown considerable variability in O^+ densities in the polar cap ionosphere-magnetosphere region near 6000 km altitude, from greater than 10 cm^{-3} to lower than 0.01 cm^{-3}. Regions with densities in the low range (O^+ density troughs) [*Zeng et al*., 2004] are also called ion depletion zones [*Horita et al*., 1993] at the same altitudes. Our study covered four cases of O^+ density troughs for the Polar perigee through the southern polar cap measured by the Thermal Ion Dynamics Experiment (TIDE) on Polar spacecraft [e.g., *Moore et al*., 1995]. The four cases of O^+ density troughs formations are as follow:

2.1.1 August 20 1998

The first case of reduced O^+ densities over the southern polar cap on August 20 1998 was from 15:13 UT to 15:43 UT. The corresponding invariant latitude range for the Polar spacecraft was from about 72.5º to 82º at around 1 R_E altitude. Figure 2.1 shows an estimate of O^+ ion densities in the upper panel where the vertical bar shows the error estimate. The lower panel displays the corresponding spacecraft floating potential. It should be noted that in determining these ion density estimates, a "filling-in" procedure is incorporated to estimate the missing portion of the ion distribution shielded by the spacecraft potential [*Su et al.*, 1998b]. In the data processing, the moment corrections that result from the filling-in procedure are always less than 10%. From 15:30 to 15:40 UT, the distribution was almost absent. It is difficult to identify how much of the distribution was shielded, and to use the filling-in procedure to correct the moments, but the densities were very low during this period. It should also be noted here that after August 1996 direct ion mass separation was disabled due to the failure of the TIDE time-of-flight (TOF) mass analyzer. However, it is still often possible to effectively separate the principal ion species because of their differences in ram energy in the satellite frame (the energy measured at the spacecraft). The separation of the ion species in the Polar/TIDE data analysis is based on separating the phase space density distributions of the two principal ion species, O^+ and H^+. The phase space distribution usually has two peaks with different ram energies in the spacecraft reference frame. Under the assumption that both O^+ and H^+ ions have Maxwellian distributions in velocity space, it is usually possible to distinguish the two species distribution functions. From such distributions, it is then possible to integrate the moments of different ion species after separating their distribution functions [*Chandler and Moore*, 2003].

Figure 2.1 shows the O^+ densities determined with the indicated procedures. The estimated O^+ densities were above 10 cm^{-3} for the period 15:17-15:30 UT, then sharply declined to less than 0.01 cm^{-3} for the period ~15:30-15:40 UT, and returned to elevated values of around 10 cm^{-3} for

the remaining displayed period of 15:40-15:43 UT. As per the discussion in *Zeng et al*. [2004], the region of very low (<0.01 cm^{-3}) estimated O^+ densities is designated as an O^+ trough region.

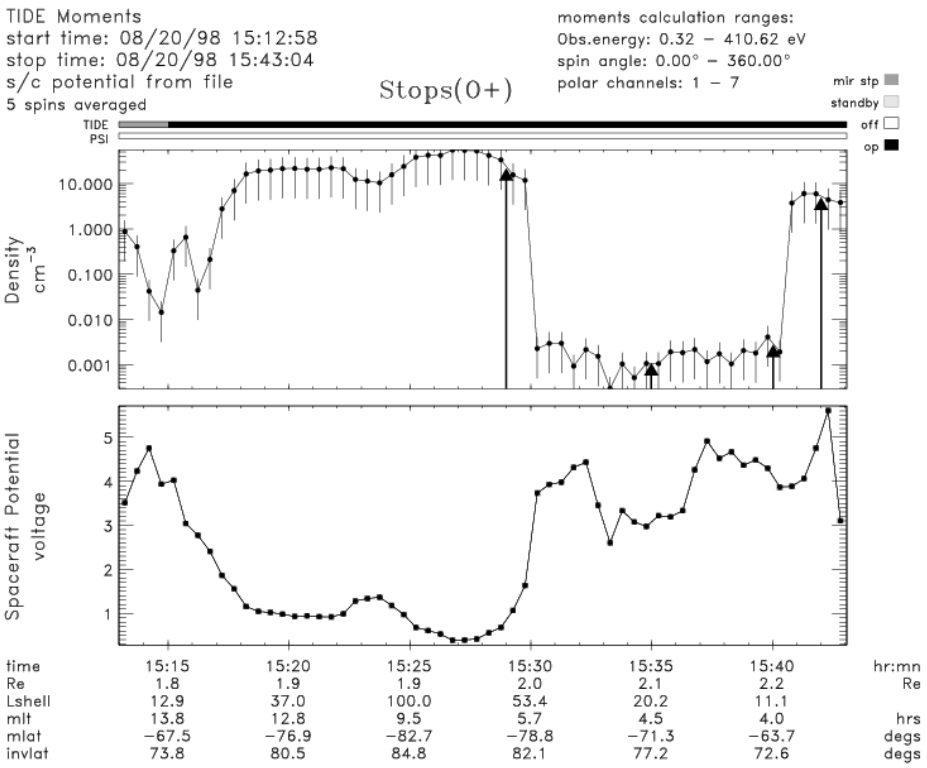

Figure 2.1 Estimated O^+ density observed from 513 UT to 1543 UT on August 20 1998. Observations were done by Polar/TIDE and also show the Polar spacecraft potential. The spacecraft potential was measured by the Electric Field Instrument (EFI) on board Polar spacecraft.

2.1.2 August 02 1998

The second case we present of low observed O^+ densities occurred on August 02 1998 during the period 1912-19:44 UT. The corresponding invariant latitude range was from about 73.1° to 89.4° at around 1 R_E altitude. The upper panel of Figure 2.2 shows an estimate of O^+ ion densities. The estimated O^+ densities were between 1 and 10 cm^{-3} for the period 19:15-19:21 UT, then declined to less than 0.01 cm^{-3} for the period ~ 19:22-19:27 UT designating the trough region, and returned to elevated values above 1 cm^{-3} after 15:28 UT to about 10 cm^{-3} for the remaining displayed period after 15:36 UT.

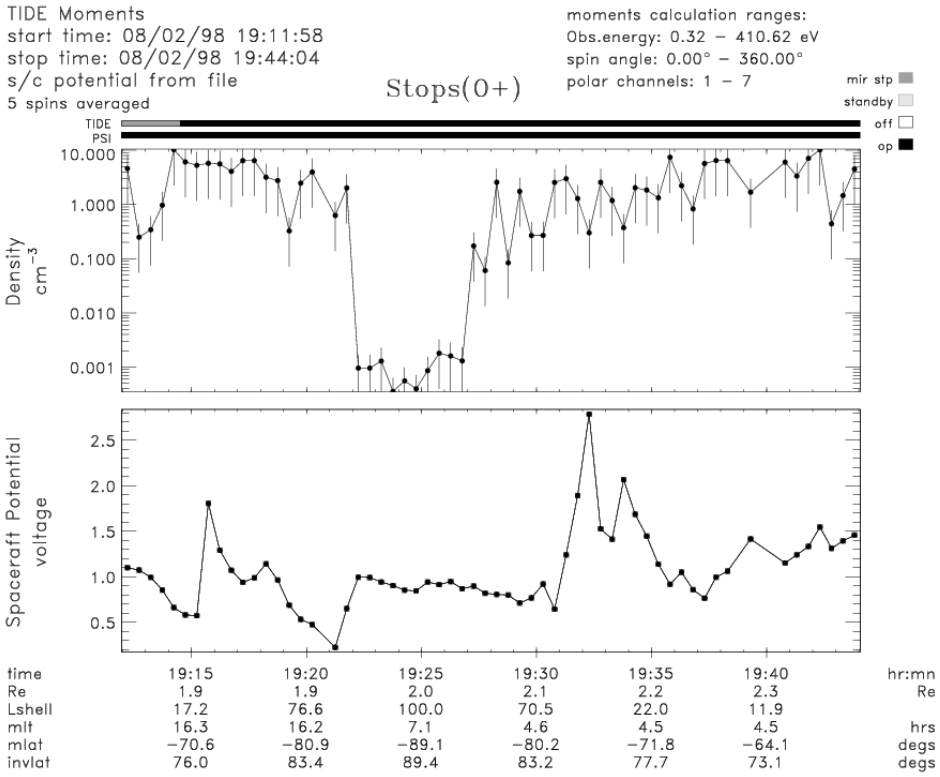

Figure 2.2 Estimated O^+ densities observed from 1912 UT to 1944 UT on August 02 1998. Observations were done by Polar/TIDE and also show the Polar spacecraft potential. The spacecraft potential was measured by the Electric Field Instrument (EFI) on board Polar spacecraft.

2.1.3 June 26 1998

The third case of low observed O^+ densities occurred on June 26 1998 during the period from 15:15 UT to 15:43 UT. The corresponding invariant latitude range for Polar was from about 73.0° to 83.7° at around 1 R_E altitude. The upper panel of Figure 2.3 shows an estimate of O^+ ion densities. The estimated O^+ densities started at about 0.1 cm^{-3}, and rose to above 1 cm^{-3} at 15:18 then dropped sharply below 0.01 cm^{-3} at 15:20. The densities rose to above 1 cm^{-3} for the period 15:21-15:25 UT. Another episode of a density drop to less than 0.01 O^+ ions cm^{-3} started from the ~ 15:27-15:34 UT designated as a trough region, and then returned to elevated values to above 1cm^{-3} for the remaining displayed period after 15:38 UT.

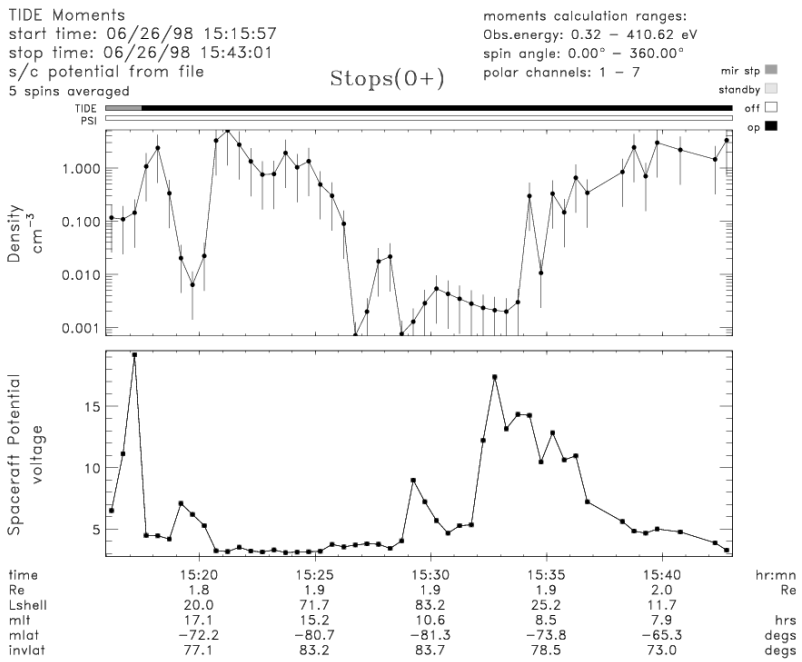

Figure 2.3 Estimated O^+ density observed from 1516 UT to 1543 UT on June 26 1998. Observations were done by Polar/TIDE and also show the Polar spacecraft potential. The spacecraft potential was measured by the Electric Field Instrument (EFI) on board Polar spacecraft.

2.1.4 December 02 1997

The fourth case of low observed O^+ densities occurred on December 02 1997 during the 1452-1520 UT. The corresponding invariant latitude range was from about 74.4° to 82.7° at ~ 1 R_E altitude. The upper panel of Figure 4 shows the estimated O^+ densities that were fluctuating for the period 1452-1509 UT, then sharply declined to less than 0.01 cm^{-3} for the period ~1514-1519 UT.

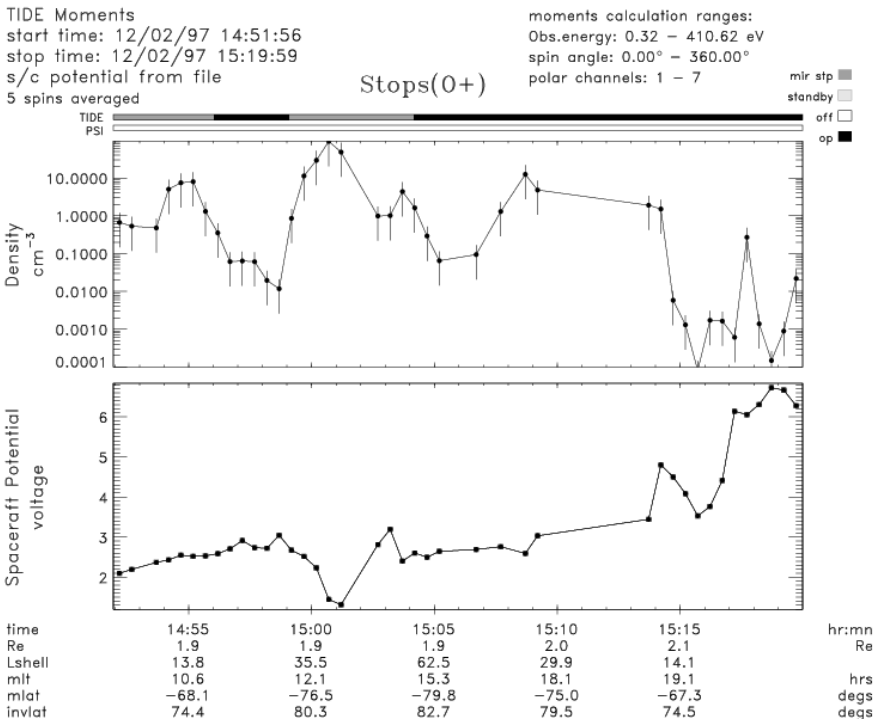

Figure 2.4 Estimated O^+ density observed from1452 UT to 1520 UT on December 02 1997. Observations were done by Polar/TIDE and also show the Polar spacecraft potential. The spacecraft potential was measured by the Electric Field Instrument (EFI) on board Polar spacecraft.

In the next chapter we use the solar wind parameters and IMF conditions as inputs driving the time-varying high-latitude electric potential model [*Weimer*, 2001] and incorporating auroral processes involving the effects of soft electron precipitation and wave-driven transverse ion heating, we simulate the ionosphere-magnetosphere plasma transport and the associated O^+ bulk parameter profiles of four flux tubes convecting in the high-latitude region.

2.2 Observations of Alfvén Waves and The Associated Accelerated Electrons and Heated Ions

Observations from Freja [*Louarn et al*, 1994; *Wahlund et al*, 1994] and FAST documented low frequency electric and magnetic field fluctuations. The electric fields in these waves are perpendicular to the background magnetic field line $B_{0.}$ The associated perpendicular magnetic field perturbation is also perpendicular to B_0. The relation between the two quantities is $E_\perp / B_\perp \approx V_A$ (10^4 – 10^7) km/s, which is on the same or higher order of as Alfvén wave speed [e.g., *Chaston et al*, 1999, 2003a]. The observations demonstrated that above the aurora oval, Alfvén waves are permanent feature in that region.

Numerous observations at low altitudes (below $1R_E$) from sounding rockets [*Boem et al*., 1990; *Knudsen et al.,* 1992; *Ivchenko et al*., 1999], as well as of different spacecraft such Freja [e.g., *Knudsen et al., 1998; Carlson et al*, 1998; *Anderson et al*, 2002], FAST [e.g., *Aikio et al*.1996; *Chaston et al,* 1999] over the aurora region have shown a strong association between the Alfvén waves propagation and particle acceleration. In addition, ground base observations of aurora have associated electron acceleration with Alfvén wave propagation in this region [*Lotko et al*., 1998; *Hallinan et al*., 2001].

FAST observations have identified high-flux field-aligned accelerated/heated electrons [e.g., *Chaston et al*., 1999a, 2001, 2003]. Also, in the dayside aurora/cusp region the data indicated that Alfvén waves accelerate and heat electrons but with field-aligned bursts [e.g., *Pfaff et al*., 1998; *Su et al*., 2001, 2004]. As mentioned before, the electron fluxes were predominantly field-

aligned with pitch angle spectra of 0, 360° being mostly downwards parallel to B_0 [e.g., *Chaston et al*, 2002, 2003, 2004].

Observations of wave forms and electron velocity distributions show that a parallel electric field generated by Alfvén wave is a mechanism for the electron acceleration [e.g.,*Chaston et a.*, 2002; *Kletzing and Hu*, 2001]. Moreover, the data measurements show the field-aligned wave Poynting flux is traveling mostly downward [e.g., *Chaston et al*, 2003]. The electron measurements report elevation in electrons energies, suggesting that the energy gain is coming from the wave and that this energization eventually results in electron burst events. The increase in electron energy flux was consistent with the observed deceases in wave Poynting flux [e.g., *Stasiewicz et al*, 2000, *Chaston et al*, 2003].

Also, observations showed an association between ion heating and small scale propagating Alfvén waves [e.g., *Wahlund et al.,* 1994; *Stasiewicz et al*., 1997; *Knudsen and Wahlund* 1998; *Andersson et al*., 2002]. The data report conics of ions especially oxygen begin at ionospheric altitudes. These O^+ ions might receive transverse heating as they elevate along the field line [e.g., *Knudsen and Wahlund*, 1998, *Stasiewicz et al*., 2000]. FAST spacecraft reported that the energies of bulk oxygen could exceed 100 eV [*Chaston et al.*, 2000], where their upstream increased besides their energy fluxes during the same time interval of Alfvén wave propagation [e.g., *Chaston et al* 2002; 2003].

Alfvén waves could be launched in the magnetosheath by different mechanisms. As an example, a flow of sheared plasma across the background magnetic field or electron/plasma density perturbation will produce Alfvén waves [*Stasiewicz,,* 2000]. FAST observations indicated that the perpendicular scale size of Alfvén waves is about 600 km at ~2000 km [*Chaston et al.*, 1999]. *Stasiewicz* [2000] suggested that based on observations from FAST, the Alfvén wave perpendicular number $k_\perp = 1\text{km}^{-1}$ in the ionosphere region. In this case, the magnitude of the perturbed density gradient will be a factor in determining the perpendicular amplitude of the Alfvén wave and its energy, which in turn would controls the aspects of the generated parallel

electric field. These observations, which show an association between the propagation of Alfvén waves, the electron heating/burst and the increase in O^+ ions out flow and its close connection to the surrounding plasma structures, determined the second topic of this dissertation.

CHAPTER 3

SIMULATION MODELS

The auroral oval is highly variable and dynamical region with physical processes that contribute to transport of energy and particles along the magnetic field lines. Electron precipitation and wave heating activities are always observed in this region. The presence of low frequency waves such as Alfvén waves carry significant energy into the ionosphere. These waves accelerate electrons to energies sufficient to cause bright auroras and ion outflow, which partially suggests that electron and ion acceleration between the ionosphere and the magnetosphere regions are complex [e.g., *Stasiewicz et al*., 2000]. However, over the polar cap region where the polar wind is dominant, the physical processes controlling the plasma flow are different and are sensitive to different solar/geophysical conditions. To facilitate the driver forces and mechanisms describing the observations and demonstrating the behavior of the plasma, we employed different models designed to describe and study two different problems. The first one, DyFK model, was used to understand and demonstrate the behavior of O^+ outflow in the high latitude region where O^+ density troughs were reported at about 6000 km altitudes. The DyFK model was employed to explain the O^+ ion density structures in the polar cap region. The second problem was to understand the associations between the propagation of Alfvén wave electron acceleration and the O^+ ions out flow in the aurora region by using the Gyro-Fluid model. This model was developed by *Jones* [2004] to launch and propagate Alfvén waves with its associated parallel electric field. This parallel electric field is one of the forces driving the electrons downward. The third code is the test particle, applied to show the accelerated electrons driven by the parallel electric field by following their kinetic motion along the flux tube. The Alfvén wave properties are determined by the structure of the surrounding plasma which is generated by DyFK model.

3.1 DyFK Model

The simulation of the ionospheric plasma outflow from the lower ionosphere region to high altitudes presented in this work is conducted by using the UT Arlington 1.5-dimensional time-dependent-Dynamic Fluid (DyFK) model. The DyFK model simulates ionospheric plasma transport dynamics along a magnetic flux tube at high-latitude [e.g., *Estep et al*., 1999; *Wu et al*., 1999, 2002; *Tu et al*., 2004a, b]. This model couples a truncated version of the moment based field line interhemispheric plasmasphere (FLIP) treatment [*Richards and Torr*, 1990]. It start typically for lower altitudes from 120 km to 1100 km altitude, to the generalized semi-kinetic (GSK) treatment [e.g., *Wilson*, 1992] of the higher-altitude regions, typically in the range from 800 km to 8 R_E altitude. The two sections overlapped between the 800 and 1100 km altitude respective boundary locations.

3.1.1 The FLIP Model

The lower segment, the truncated FLIP model, is a one-dimensional time-dependent fluid model that solves the coupled time-dependent ion continuity, momentum, and energy transport equations for the various species in the dense ionospheric region. Thereby we assumed that the velocity distributions of all species are Maxwellian in nature and that the bulk flow velocities are low and very subsonic, besides the temperature differences between species are assumed to be isotropic and relatively small at any given instant. In the fluid region DyFK calculates densities, field-aligned velocities and temperatures for H^+, O^+ and electrons by solving the continuity, momentum and the energy equations [*Young et al*., 1980; *Torr et al.,* 1990].

The ion continuity equation is given by

$$\frac{\partial n_i}{\partial t} + \nabla . \phi_i = P_i - L_i n_i \qquad (3.1)$$

Where n_i is the ion density, ϕ_i is the field-aligned ion flux. P_i, L_i are the production and loss rate coefficiens respectively.

$$\phi_i = n_i U_i \qquad (3.2)$$

U_i is the field-aligned flow velocity of ion and given by

$$U_i = \left(\frac{v_{ij}}{\sum(v)}\right) U_j + \left(\frac{v_{in}}{\sum(v)}\right) U_n - D_i \left[\frac{\nabla(n_i T_i)}{n_i T_i} - \frac{m_i g_{\parallel}}{k_B T_i} + \frac{\nabla(n_e T_e)}{n_e T_i} + \frac{n_j}{n_i + n_j}\left(\frac{\alpha_{ij}}{T_i}\nabla T_i - \frac{\alpha_{ij}^*}{T_i}\nabla T_j\right)\right] \qquad (3.3)$$

Where i and j represent one pair of ions in the fluid region, and continue to iterate covering all the species where they interact through both coulomb collisions and polarization electric fields. U_n is the field-aligned neutral wind velocity, v_{ij} is coulomb collision frequency. D_i is the ordinary ion diffusion coefficient, and α_{ij} and α_{ij}^* are thermal diffusion coefficients. m_i, n_e, T_i and T_e are the i th ion's mass, the electron density, the ion and electron temperature respectively.

The thermal electron/ion energy equation

$$\frac{3}{2} n_j k_B \frac{\partial T_j}{\partial t} + n_j k_B T_j \nabla . U_j + \frac{3}{2} U_j . \nabla T_j + \nabla . q_j = \sum Q_i - \sum C_i \qquad (3.4)$$

Where j stands for electrons and ions, U_j is the field-aligned flow velocity of ions/electrons. Q_j is the ions/electrons heating rate, C_j is the ions/electrons cooling rate. The electron temperatures provide the treatment for the lower boundary conditions to the upper region at 800 km altitude for every time step. Now the parallel motion of the ions is governed by the following equation:

$$m_i \frac{dv_{i\parallel}}{dt} = q_i E_{\parallel} - \frac{G m_i M_B}{r^2} - \mu_i \nabla_{\parallel} B + V_C \cdot \left(v_{i\parallel} \frac{\partial \hat{b}}{\partial S} + (V_C \cdot \nabla)\hat{b}\right) \qquad (3.5)$$

Where m_i and q_i are the ion's mass and charge, $E_{\|}$ is the electric field parallel to the ambient magnetic field B with its unit vector $\hat{b}$, and $\mu_i = m_i v_{\perp}^2 / 2B$ is the ion magnetic moment.

$V_C = \dfrac{E \times B}{B^2}$ is convection velocity.

3.1.2 The GSK model

The GSK model advances O^+ and H^+ gyrocenters along the flux tube for every time step [*Wilson et al,* 1990; 1992; *Ho et al.*, 1997], the particles are subjected to all macroscopic and microscopic forces, including the ambipolor electric force, gravity, mirror force

$$m_i \frac{dv_i}{dt} = q_i E_{\|} - \frac{G\ m_i M_E}{r^2} - \mu_i \nabla B \qquad (3.6)$$

$\mu_i = m_i v_{\perp}^2 / 2B$ is the ion magnetic moment.

The parallel electric field is based on the assumption of quasi-neutrality and is given by

$$E_{\|} = -\frac{K_B}{e}\frac{dT_e}{dr} - \frac{K_B T_e}{e\ n_e}\frac{dn_e}{dr} \qquad (3.7)$$

where T_e, n_e, k_B, r and e are electron temperature, density, Boltzmann constant, geocentric distance and electron charge respectively.

Also the convection-driven frictional ion heating caused by $E \times B$ ion drift in the F region/topside ionosphere [e.g., *Schunk et al*, 1997] is included besides the centrifugal force which accelerates particles due to the flux tube convection in the GSK region [*Horwitz et al.*, 1994]. In addition, the simulated ions experience Coulomb collisions and collisions with neutrals which cause charge exchange [*Wilson et al*, 1992; 1994] where eventually non-Maxwellian distributions are gradually developed. The GSK simulation incorporates the electron neutral fluid description where the generalized electric field is calculated in a self consistent way. The

thermal electron temperature is isotropic; however, the parallel and perpendicular electron temperatures are calculated in a self-consistent method by solving electron transport equations allowing the electron fluid exchange energy with the surrounding ions [*Su et al*., 1998b]. Ions are produced through ionization processes such as precipitation and solar illumination but lost through recombination or chemical reaction. However, new particles are constantly injected into the simulated flux tube through the upper boundary cell of the fluid part and then into the GSK part are through the bottom cell of this kinetic region.

3.1.3 The Overlapping Region

The two regions join by injecting FLIP with simulation particles ions into the GSK simulation region through the bottom simulation cell, where it iterates the solutions of both parts until a match of moment parameters is reached and a certain steady state for the flux tube is attained. The ions are drifting into the bottom cell of kinetic region holding Maxwellian distribution but in the following time step, their bulk parameters that have been calculated in the fluid region below 800 km altitude will be passed to the GSK region at 1100 km altitude to pass back the gradient values. In this overlapping region the values alternate between the two region ensures transit smooth solutions from the FLIP to GSK regions.

In all the DyFK simulations covered in this study, we first initialize a flux tube that runs for some time to reach a quasi-study polar wind state.

3.1.4 Auroral Processes in DyFK Model

The DyFK model has an option to incorporate the effects of auroral soft electron precipitation and wave heating [*Estep et al.,* 1999; *Wu et al*., 1999]. In the FLIP model, the effects of two-stream transport model precipitating auroral electrons on the ionosphere are included [*Richard and Torr*, 1990; *Richards*, 1995a]. The ionization and thermal electron heating rates due to electron precipitation are incorporated. These precipitating soft electrons drive the

ion outflows by elevating the electron temperature first and increase O^+ ions production in the top side ionosphere [e.g*., Whitteker*, 1977]. This leads to enhancement in the generated ambipolar electric field, and increases the upflowing ion fluxes. In addition, the wave-driven ion heating process through cyclotron resonance is included in high altitude auroral GSK region. The perpendicular heating [*Brown et al*., 1995; *Wu et al.,* 1999; 2002] increases the ion energies in the perpendicular direction causing the formation of shells, bowls and conic ion distributions [e.g., *Crew et al*., 1990; *Andre et al.,* 1990]. DyFK model uses the perpendicular ion heating technique given by *Crew et al*. [1990] and *Brown et al* [1995b]. The procedure starts by injecting every ion with a random perpendicular energy at each time step. This energy given by the Gaussian distribution

$$P\ (\delta w) = \frac{1}{\sqrt{2\pi\sigma}} \exp\left(-\frac{(\partial w)^2}{2\sigma^2} \right) \qquad (3.8)$$

$\sigma = \delta t\ (2 m_i D_{i\perp}(r))$, δt is the length of a time step and the $D_\perp(r)$ is the diffusion coefficient given by

$$D_\perp(r) = \left(\frac{\eta\ q^2}{4 m_i^2} \right) \left| E\ (\omega = \Omega(r)) \right|^2 \qquad (3.9)$$

and η is the fraction of left-hand polarized electric field spectral density. The wave spectral density was calculated by

$$\left|E_\perp(\omega, r)\right|^2 = \left|E_{\perp 0}\right|^2 \left(\frac{\omega}{\Omega_{O+}(r_0)} \right)^{-1.7} \begin{cases} \exp\left(\frac{r-3}{0.1} \right) & r \geq 3 R_E \\ 1 & 1.3 R_E < r < 3 R_E \\ \exp\left(-\frac{r-1.3}{0.05} \right) & r \leq 1.3 R_E \end{cases} \qquad (3.10)$$

Now the new perpendicular energy is given by

$$w'_\perp = w_\perp + \delta w + 2\sqrt{w_\perp \delta w}\ \cos\theta \qquad (3.11)$$

θ is random phase angle with even probability in the range (0~2π). The auroral electric field wave spectral density profile was adopted with "benchmark" spectral density at 6.5 Hz selected to be 0.3 x 10^{-6} V^2 m^{-2} Hz^{-1}, and Broad Band Extremely Low Frequency BBELF wave power spectral index was 1.7. The wave amplitude at H^+ gyro frequencies is about 100 times less than that at O^+ gyro frequencies due to the mass dependence. The difference results in lower H^+ heating rate 10 times lower than O^+ heating rate.

Figure 3.1 shows the regions and the mechanisms adopted by DyFK model. The transport processes along the field line include the ambipolar electric field, gravity, the mirror force, transverse ion heating and the potential drop which play a significant role for particle acceleration.

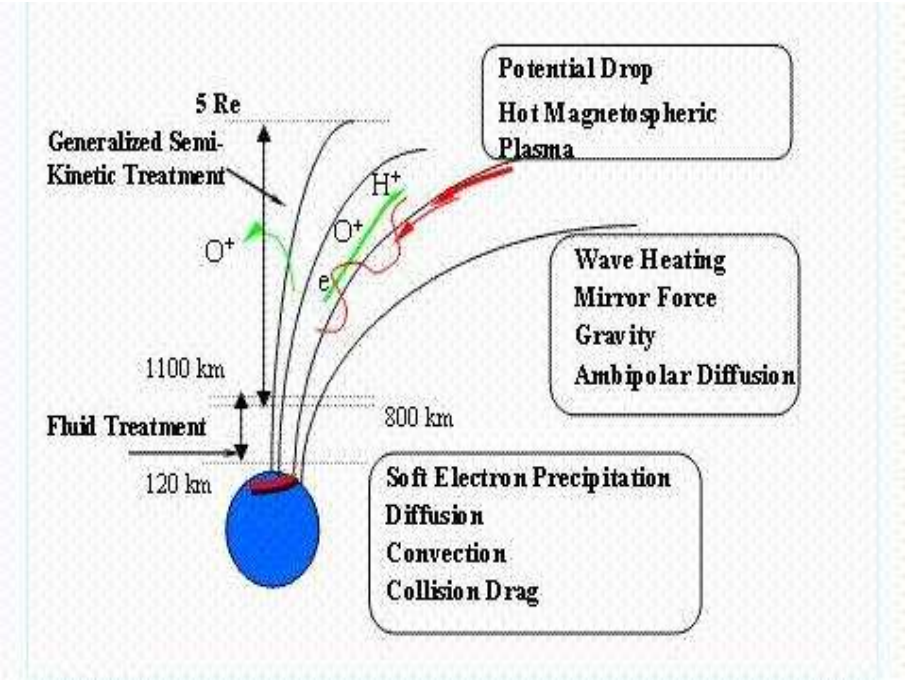

Figure 3.1 Schematic of the DyFK model regions and the ion transport processes.
It also shows the physical processes that is involved in the ionosphere- magnetosphere regions [*Tu et al* issertation, 2004].

3.2 Gyro-Fluid Model: The Alfvén Wave Model

The linear one dimensional gyrofluid model was used to simulate the propagation of Alfvén waves along a magnetic flux tube. The model incorporates finite ion's Larmour radius effects and electron inertia. Electrons and ions are considered fluids. This gyro fluid approach gives a wider description of kinetic Alfvén waves that propagate in magnetosphere-ionosphere magnetized plasma.

The derivation of the Gyro-Fluid equations was adapted from *Beer and Hammett* [1996]. However, the following Gyro-Fluid equations are described by [*Jones and Parker*, 2003; *Jones et al.*, 2004; *Su et al.*, 2004]. The generated parallel electric field $E_{\|}$ is responsible for energizing electrons and is based on the derivation of the scalar potential ϕ and vector potential A

$$E_{\|} = -\frac{\partial A}{\partial t} - \nabla \phi \qquad (3.12)$$

The vector potential is related to the scalar potential at the ionospheric boundary through the following equation

$$\phi = -\frac{A_{\|}}{\mu_0 \Sigma_P} \qquad (3.13)$$

Σ_P is the Pederson conductivity. The scalar potential is given by Poisson equation

$$\nabla_{\perp}^2 \phi = \frac{-e}{\varepsilon_0}\left(\sum n_i - n_e\right) \qquad (3.14)$$

Using certain assumptions as mentioned in details in *Jones* [2004], the scalar potential is given by

$$\phi = \frac{\sum n_{i1} - n_{e1}}{\sum n_{i0}\left(1-\Gamma_0\right)\frac{e}{T_i} + k_{\perp}^2 \frac{\varepsilon 0}{e}} \qquad (3.15)$$

n_{i0} , n_{i1} and n_{e1} are the initial ion density, and perturbed ion and electron densities respectively. The particles included in the plasma simulation are O^+, H^+, and e^-, and $n_e = n_O + n_H$.

The $K_\perp^2 \frac{\varepsilon_0}{e}$ term represents the displacement current in the parallel direction to B . This term was ignored in the simulation because the earth's Alfvén wave speed << C (the speed of light).

T_i is the ion temperature and $\Gamma_0(b) = e^{-b} I_0(b)$ (gamma function), where I_0 is the first modified Bessel function and $b = k_\perp^2 \rho_i^2$. This term appeared when we considered the ion density n_i is different than the guiding center density $\overline{n_i}$ but related by $n_{i1} = \overline{n_{i1}} - n_{i0}(1 - \Gamma_0(b_i))\frac{e\phi}{T_i}$.

This means, the total ion density perturbation n_i is a combination of the gyro-phase $\overline{n_i}$ and the polarization drift n_p (the second term).

The dispersion relation is given by

$$\frac{\omega^2}{k_\parallel^2} = V_A^2 \frac{1 + k_\perp^2 \rho_s^2}{1 + k_\perp^2 \lambda_e^2} \qquad (3.16)$$

Where $V_A = B \Big/ \sqrt{\Sigma n_i m_i \mu_0}$ is MHD Alfvén speed, $\rho_s = \sqrt{m_i T_e / e^2 B^2}$ is an ion acoustic gyroradius, and $\lambda_e = C / \omega_{pe}$ is electron skin depth and ω_{pe} is the electron gyro frequency.

The dispersive Alfvén wave adopted in the code was based on the advancing evolution of particle velocity, pressure and density perturbations along with the $E_\parallel, \phi \ A$. To simplify the

derivations, the ion fluid equations were neglected and the plasma was assumed to be a neutralized one ion species, the full ion fluid dispersion relation is,

$$\sum_i \frac{n_{i0}}{m_i\left(1+b_i/2\right)}\left(1-\frac{3T_i}{m_i V_P^2}\right)^{-1}+\frac{n_{e0}}{m_e}\left(1-\frac{T_e}{m_e V_P^2}\right)^{-1}+\frac{k_\perp^2}{\mu_0 e^2}=$$
$$\frac{k_\perp^2}{\mu_0 e^2 V_P^2}\left[\frac{\dfrac{n_{i0}}{m_i\left(1+b_i/2\right)^2}\left(1-\dfrac{3T_i}{m_i V_P^2}\right)^{-1}+\dfrac{n_{e0}}{m_e}\left(1-\dfrac{T_e}{m_e V_P^2}\right)^{-1}}{\sum_i n_{i0}\left(1-\Gamma_0\right)T_i^{-1}}\right] \qquad (3.17)$$

$V_P=\omega/k_\parallel$ is the phase speed of the Alfvén wave. This equation was obtained by solving the continuity equation of electrons and ions and momentum equations, for more details see *Jones* [2004]. The Gyro-Fluid code operated on a one dimensional flux tube located at 70° latitude, extended from the lower ionsphere region to about 7 R_E . The model included three species O^+, H^+, and e^- where it launches propagating single Alfvén wave from the top of the field line. From equation (1.1) the magnitude of the generated parallel electric increases with increasing the Alfvén wave speed but it decreases with the increase in medium density. This background density environment was simulated by the DyFK model. The electrons response to the $E_\parallel$ will be studied using the test particle code.

3.3 Test Particle Method

This code is designed to simulate the electron kinetics where we can test the electron heating/burst signature and was developed by *Su et al* [2004]. The field-aligned electric field $E_\parallel$ is generated by the Gyro-Fluid code. Test particles interact with $E_\parallel$ modifying the distribution function. The particles representing the magnetosheath electron of a flux tube are

introduced from the top of the field line with a specific temperature. These electrons are introduced with Maxwellian distribution function and allowed to fill the flux tube in a steady state. The flux tube was injected with 350,000 electrons. The electrons are subjected to three forces; the electric forces generated by Gyro-Fluid $E_{||}$, the mirror force, and the gravitational force. The kinetic equation driving the test electrons along the magnetic field line is:

$$m \frac{dv}{dt} = q E_{||} - mg - \mu \nabla B \qquad (3.18)$$

$\mu = m v_{\perp}^{2} / 2B$ is the electron magnetic moment,

The behavior of the simulated particles and their position, parallel and perpendicular velocities are recorded at each time step.

After allowing the propagation of $E_{||}$ due to launching an Alfvén wave, the electrons were constantly replenished from the top and bottom boundaries to replace the particles which leave the simulation. The electrons response to $E_{||}$ does not affect the Alfven wave amplitude therefore the models are not self consistent.

CHAPTER 4

SIMULATIONS OF THE FORMATION OF O^+ DENSITY TROUGHS AT 6000 Km ALTITUDE IN THE POLAR CAP IONOSPHERE-MAGNETOSPHERE REGION

The purpose of this study is to investigate the mechanisms that control the O^+ ion density structure in the polar cap ionosphere-magnetosphere region. This chapter presents an investigation of the formation of O^+ density structures involving normal and trough (<0.01 cm^{-3}) level densities at the Polar/TIDE satellite altitude (~ 1 R_E). The data were collected during the spacecraft passes in the southern polar cap perigee. It includes comparison between simulation results of normal and trough O^+ densities with the observations under specific solar and geophysical conditions. In addition, we show simulation results of the H^+ ion densities during the same period of time at the observation altitudes. We covered four different data sets or cases for different dates. The ionospheric plasma transport simulations were conducted using the UT Arlington Dynamic Fluid-Kinetic (DyFK) model. The simulation of the O^+ and H^+ bulk parameters evolution of every case started first by constructing the simulated flux tube which is presumed to convect along the paths determined from the Weimer electric potential model [*Weimer*, 2001], until it intersects the Polar track. The Weimer model determines the convection electric trajectories by including the solar indices and various geophysical parameters that existed at the time of the Polar/TIDE pass. During the convection of the flux tubes through the segments of the trajectories, they might pass through designated auroral oval region; auroral processes in DyFK model of soft electron precipitation and wave-driven transverse ion heating are turned on. The auroral region was determined initially by the Ovation Model [*Newell et al.*, 2002]. However, other measurements were also considered of the same period of the Polar pass. The goal is to have more precise boundary measurements of the auroral oval at the time of these observations. The next two paragraphs we display a general overview of Weimer convection trajectories and the modified Aurora boundaries and the steps of conducting both simulations.

4.1 Initial Simulation Steps

4.1.1 Convection Trajectories

As stated above, the high-latitude ionospheric electric potentials or the convection trajectories used here were based on the empirical ionospheric electric potential model [*Weimer*, 2001]. The structure of the convection electric fields in the ionosphere and inner magnetosphere is important for the reason of determining the geo-physical conditions and physical processes that would be incorporated in the flux tube passing through different regions of the polar cap [*Weimer*, 2001]. These polar cap electric potentials are a projection of the physical processes that existed in the coupled solar wind-magnetosphere-ionosphere system. In other words the trajectories are product of the interplanetary Magnetic Field (IMF) and solar wind coupling behavior with the earth magnetic field [*Weimer*, 2001]. The Weimer model includes the effects of corotation and accepts inputs of solar wind density, velocity, and IMF as its driving parameters. In this study, the solar wind conditions used were measured by the Solar Wind Experiment (SWE) on board the Wind satellite [*Ogilvie et al.*, 1995] and the IMF (Interplanetary Magnetic Field) parameters were measured by Magnetic Field Instrument (MFI) on board of Wind satellite [*Lepping et al.*, 1995]. For the simulations, the convection trajectories were “reverse” convected backward for approximately 6 hours prior to the observation time to designate the starting location of the simulation trajectory and the simulated flux tubes for the study cases were set up at their starting locations and times. As we mentioned before, they were assumed to move along their convection trajectories (with model time steps of 24 s) until they intersected the Polar track.

4.1.2 Aurora Boundaries

Several models may be used to estimate the location and width of the auroral oval. The approach used here for auroral oval boundaries estimation was partially based on the Ovation model [*Newell et al.*, 2002] which is constrained by measurements from the Defense Meteorological Satellite Program (DMSP) [*Rich and Hairston*, 1994]. The Ovation model includes SuperDARN HF radar data, DMSP particle data, and Polar Ultraviolet Imager (UVI) images [*Newell et al.*, 2002]. The model considers a special algorithm to calculate the boundaries of the auroral oval and the intensity of the auroral precipitation with in it. The model calculates the area of the auroral region mapped over a period of time which extends to ~30 minutes long. However, in our search for the actual aurora boundaries during Polar/TIDE observation, we considered other aurora location that had been reported by different instruments such as Polar/HYDRA (at the same time of the observations). Based on the collection of these other data sources, we have slightly adjusted the Ovation aurora boundaries to be consistent with the other measurements.

4.1.3 Common Simulation Conditions

The following section is a display of simulation results of O^+ density troughs and the associated H^+ densities for the following four dates or cases: case 1, was on August 20 1998 between 15:13-15:43 UT. Case 2 was on August 02 1998 between 19:13-19:44 UT. Case 3 covered June 26 1998 between 15:16-15:43 UT. Case 4 was on December 02 1997 from 14:52 to 15:20 UT. However, we go only over the first case in detail, exploring the procedures and steps to determine the O^+ and H^+ simulation density results and compare them with observation. We first go over the general conditions and DyFK simulation parameters that were applied through all cases. For all 4 cases, the observed O^+ densities were measured by the Thermal Ion Dynamics Experiment (TIDE) on Polar spacecraft during pass over the southern polar cap [e.g., *Moore et al.,* 1995]. For all the simulated trajectories, the starting point was located within

the polar cap, and each flux tube was initiated there with a quasi-steady state polar wind profile for that geographic location and level of solar illumination, etc. The upper boundary condition of the electron temperature at 3 R_E altitude was set at 3000 K in the polar cap and at 6000 K in the auroral regions. Although such upper boundary temperature settings contain considerable uncertainties, they should permit worthwhile qualitative investigations on the mechanisms that produce the O^+ density structures in the polar cap ionosphere/magnetosphere as observed by Polar/TIDE. For the auroral processes, and for every flux tube in all 4 cases, the soft electron precipitation stream was taken to be a streaming Maxwellian energy spectrum, with peak at 100 eV [*Newell et al.*, 1996]. The energy flux of the soft electron precipitation was taken to be 1 erg cm^{-2} s^{-1} at 800 km altitude [*Richards and Torr*, 1990]. Although these parameters are not tied to particular observations during the event in question, it is worth noting that the study of *Seo et al.* [1997] of soft electron precipitation and *F* region/topside upflows determined that upward ion flows at 800–850 km were often closely correlated with soft electron (defined there as <1 keV) precipitation with characteristic energies below 500 eV and soft electron associated energy fluxes below 3 erg cm^{-2} s^{-1}. The auroral electric field wave spectral density profile was that adopted by *Wu et al.* [1999], with the "benchmark" spectral density at 6.5 Hz selected to be 0.3 × 10^{-6} V^2 m^{-2} Hz^{-1}, and the BBELF wave power spectral index was 1.7 [*Crew et al.*, 1990]. The simulations were initiated with a typical flux tube in the polar cap absent auroral processes, which was in a quasi-steady state. The initial flux tube was chosen with some arbitrariness because its real evolution history would be difficult to determine anyway.

4.2 Trough Cases

4.2.1 Case 1: August 20 1998 (15:13-15:43 UT)

The observed O^+ densities for the Polar perigee pass through the southern polar cap on August 20 1998 was reported from 1513 UT to 1543 UT. The corresponding invariant latitude range was from about 72.5° to 82° at aroun d 1 R_E altitude. Figure 2.1 (top) shows an estimate of O^+ ion densities, where the vertical bar shows the error estimate. In this case, the estimated O^+ densities were above 10 cm^{-3} for the period 1517–1530 UT, then sharply declined to less than 0.01 O^+ ions cm^{-3} for the period ~1530–1540 UT. The O^+ ion densities returned to elevated values of around 10 cm^{-3} for the remaining displayed period of 1540–1543 UT. As per the discussion in the work of *Zeng et al*. [2004], the region of very low (<0.01 cm^{-3}) estimated O^+ densities is designated as an O^+ trough region.

For full observation/simulation comparisons, 14 different points located along the Polar/TIDE pass between 1525 and 1543 UT were selected for comprehensive study. We chose four points traversed by Polar at 1529, 1535, 1540, and 1542 UT to present the detailed DyFK simulation/observation comparisons. As noted earlier, the convection trajectories linking to these points were established from the empirical electric field model of *Weimer* [2001]. The IMF and the solar wind conditions required by Weimer's model determine the convection patterns are displayed in Figures 4.1 and 4.2 respectively. We also considered the transit time for the solar wind signals from Wind spacecraft to the earth's magnetopause, which was about 17 min. As seen from Figure 4.1, the IMF *By* varied between −2 and −11 nT, and IMF *Bz* varied between −6 and −13 nT. The solar wind velocity was about 336 ± 8 km/s. Figure 4.2 shows that the solar wind density fluctuated between 2 and 25 cm^{-3}.

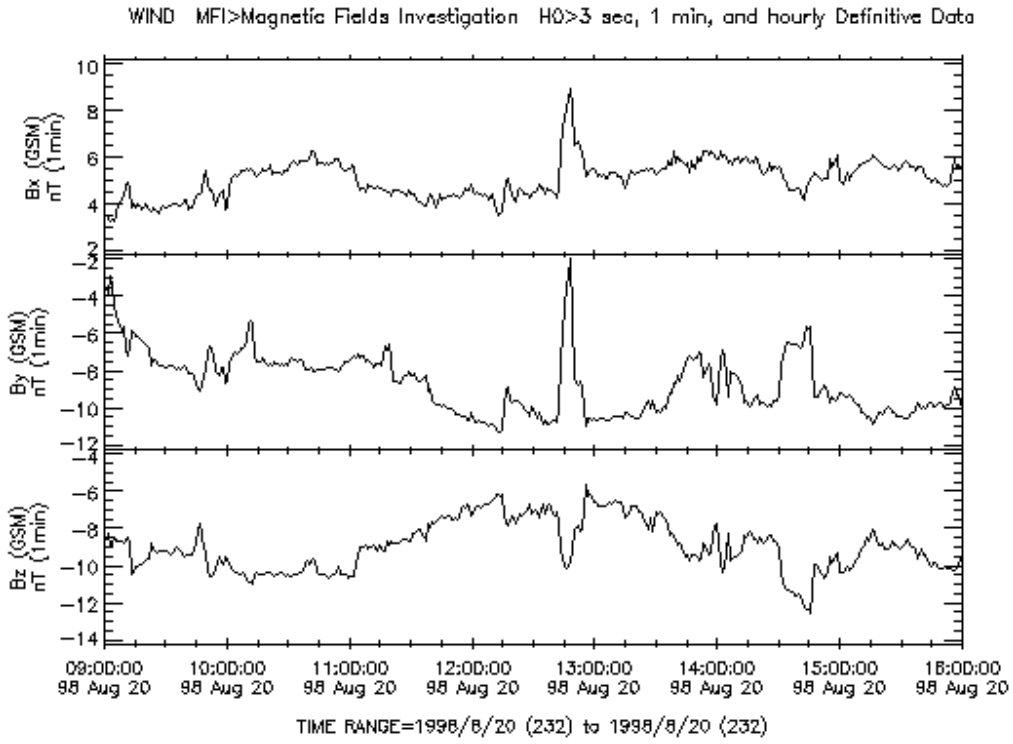

Figure 4.1 The interplanetary magnetic field (IMF) on August 20 1998. The interval from 0900 to 1600 UT corresponds to the 6 hours period plus the 17 min transit time prior to Polar/TIDE measurements. Data and plot courtesy of CDA web site: (www.cdaweb.gsfc.nasa.gov/) and provided by R. Lepping at NASA/GSFC.

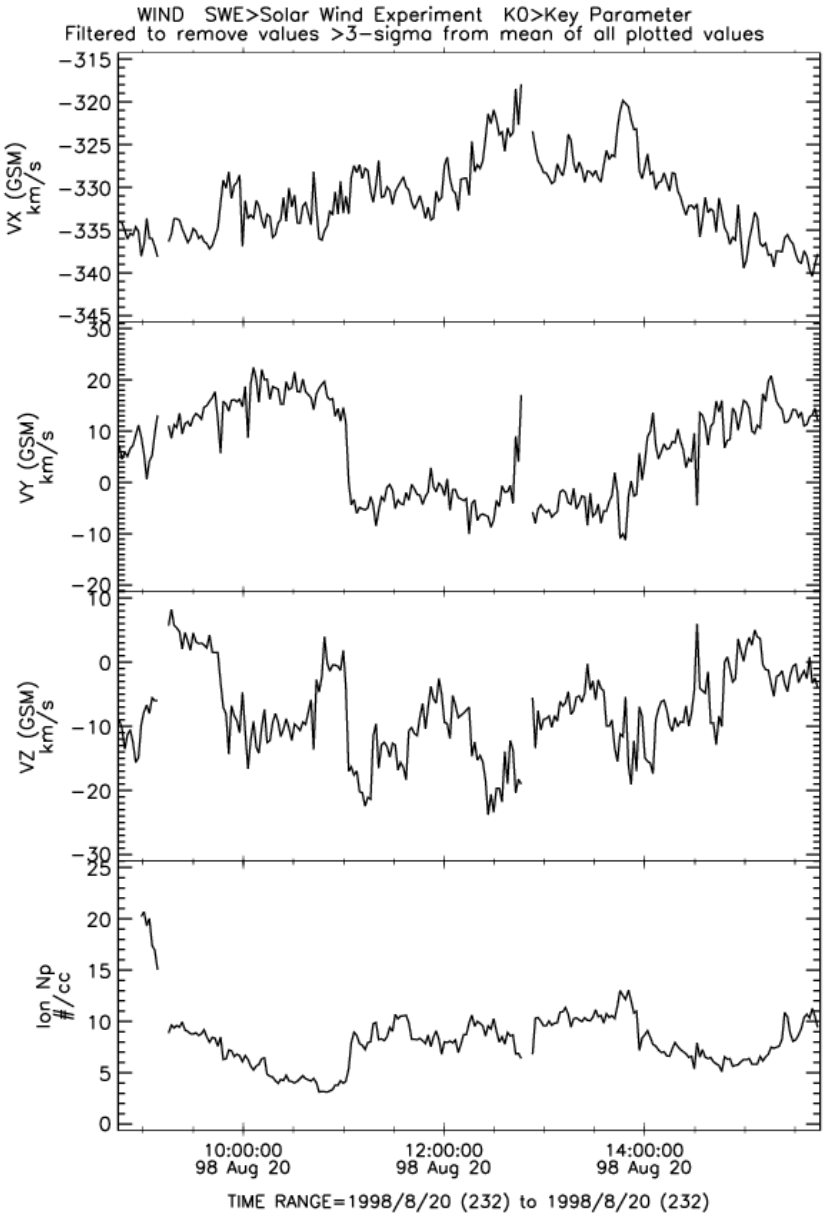

Figure 4.2 The solar wind conditions detected by Wind on August 20 1998. The interval from 0900 to 1600 UT corresponds to the 6 hours period plus the 17 min transit time prior to Polar/TIDE measurements. Data and plot courtesy of CDA web site: (www.cdaweb.gsfc.nasa.gov/).

The DyFK model simulated 13 flux tubes which were set up in their starting locations and times such that they would have intersected the Polar trajectory at the indicated observation times. During the convection of these flux tube along their trajectories, for the segments passing through the designated auroral oval regions, auroral processes of soft electron precipitation and transverse ion heating by waves were turned on. As mentioned before, for the aurora oval boundaries which existed at the time of the Polar/TIDE pass, we have used the Ovation model to calculate the aurora boundaries based on the DMSP observations. The data during its polar pass recorded the following boundaries coordinates of the aurora as follow, the two equatorward boundaries were located at about 62.5° INV LAT/18.3 MLT and 63° INV LAT/7.2 MLT, and the two poleward boundaries at 73.5° INV LAT/17.9 MLT and 74° INV LAT/7.5 MLT. Figure 4.3a shows the Ovation-based auroral oval along with both the DMSP track and the Polar track. However, the boundaries of the Ovation auroral oval appeared to be partially inconsistent with the Polar/HYDRA electron observations on these field lines during the same period [Scudder et al., 1995]. The Polar/HYDRA measurements indicated that the invariant latitude of the poleward boundary of the auroral oval was approximately 64° on the dawnside between 3 and 4 MLT. In addition, the Polar/TIDE energy flux observation for the same period of time indicated that the invariant latitude of the poleward boundary of the auroral oval was approximately 71° INV LAT on the dayside between 13 and 14 MLT. Therefore, the Ovation/DMSP-based model was modified slightly so that the auroral oval locations were consistent in the Polar-traversed local time sector. This modified auroral oval is displayed in Figure 4.3b with the four relevant convection trajectories. From Figure 4.3b, we can see that the convection trajectory ending at 1529 UT traversed both the designated auroral oval region and the indicated polar cap region. The convection trajectories ending at 1535, 1540, and 1542 UT were completely confined within the polar cap region under the indicated regional designations. The corresponding Polar/TIDE-measured O^+ densities at 1529 and 1542 UT were about 15.6 and 4.4 cm^{-3}, respectively, and

the nominal estimated O^+ densities at 1535 and 1540 UT were below 0.01 cm^{-3}. Each of these points is delineated in Figure 2.1 by an arrow connecting the time axis with the density line.

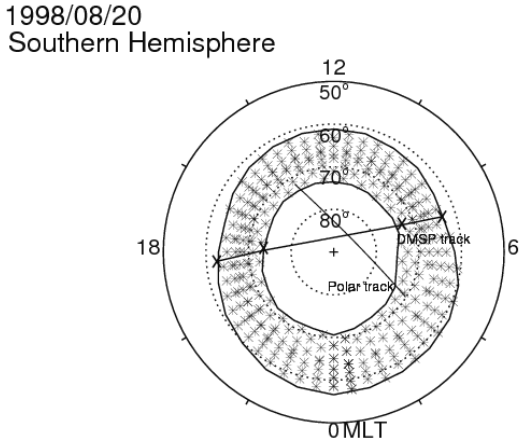

(a)

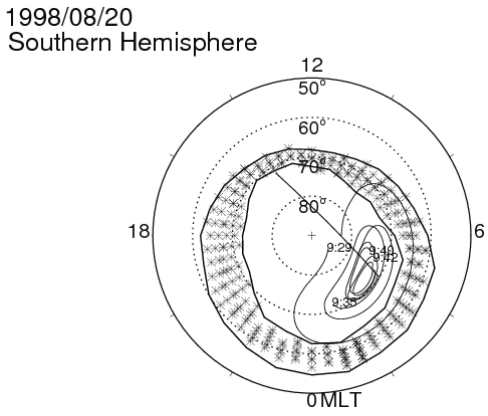

(b)

Figure 4.3 (a) The Ovation-based aurora oval based on DMSP model along with the Polar track trajectory. (b) The four selected Weimer trajectories in the southern high-latitude region with their intersections with the modified auroral oval region.

The simulations were initiated with a typical flux tube in the polar cap absent auroral processes, which was in a quasi-steady state. As we mentioned before, the initial flux tube was chosen with some arbitrariness because its real evolution history would be difficult to determine anyway. For the points located at 1529, 1535, 1540, and 1542 UT and all other selected points, DyFK simulations were run first to attain quasi-steady state profiles at the respective starting locations. The following geophysical parameters were adopted in DyFK simulation to reflect the realistic conditions on August 20 1998: *AP* index = 17, the solar radio activity index $F_{10.7}$ = 142, and the 90 day averaged $F_{10.7}$ = 133. Again, when the flux tubes passed through the aurora boundaries, the aurora process was turned on with soft electron precipitation and transverse wave heating.

4.2.1.1 O^+ Densities for 1529 UT

The first simulation presented pertains to the Polar/TIDE observations at 1529 UT. The modeled flux tube convection trajectory, displayed in Figure 4.4a, was reverse-traced to 0929 UT. This nominal initial model location of the flux tube is indicated by the letter A at 84.5° invariant latitude, 3.5 h magnetic local time . The flux tube was then convected to point B (61.4° INV LAT, 01 MLT) where the indicated auroral processes were initiated. The flux tube exited the auroral region at point C (74.6° INV LAT , 8.8 MLT). The flux tube convected to the intersection point with the Polar track at point D (82.6° INV LAT, 5.9 MLT) (Figure 4.4.a). The simulated O^+ density profile for this time and flux tube location is displayed in Figure 4.4.b. The O^+ density estimate from Polar/TIDE was 15.6 cm^{-3} at ~6000 km altitude, and the simulation-produced O^+ density was ~14.5 cm^{-3}.

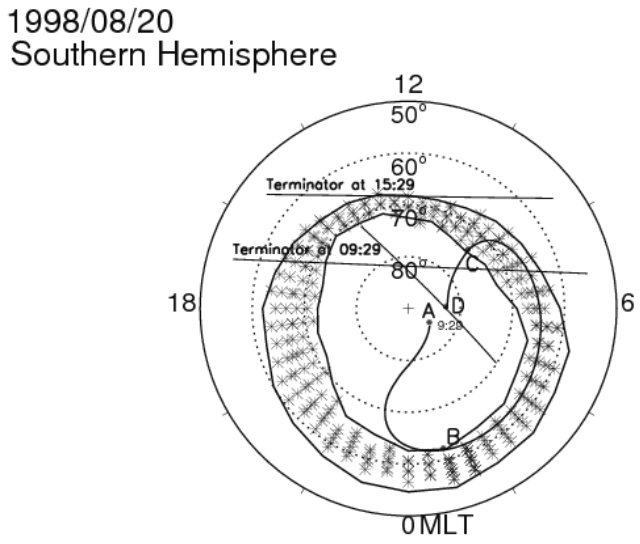

(a)

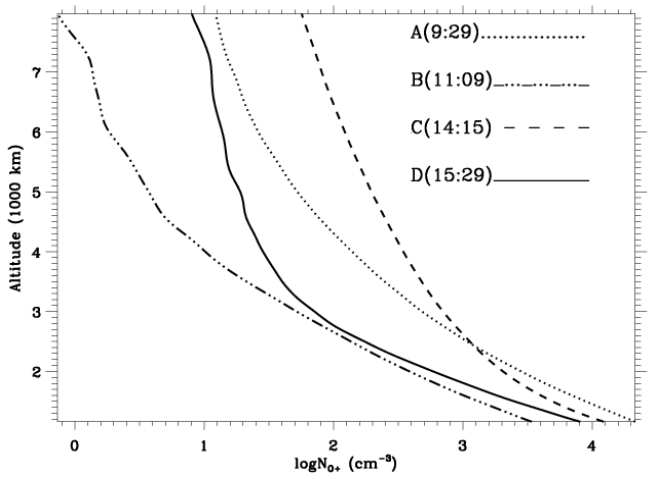

(b)

Figure 4.4 (a) The convection trajectory which projected to intersect the Polar track at 15:29 UT in the southern ionosphere on August 20 1998. The initial point for the flux tube is denoted with A. The flux tube entered the aurora region denoted at B and exited at point C, finally reached the observation point at 15:29 UT. Based on the indicated loci of the 300 km altitude, the terminators for the start and end times show the *F* region portions of the flux tube along the convection trajectory path was largely in darkness. (b) The simulated O^+ density profiles when the flux tube located at points A, B, C, and D, respectively.

4.2.1.2 O^+ Densities for 1535 UT and 1540 UT

The second and third convection trajectories in the present simulations intersected with the Polar track at 1535 and 1540 UT respectively. In both cases, the model trajectories were confined to the polar cap region and their *F* region portions were confined in darkness. These model convection trajectories are displayed in Figure 4.5 and 4.6 respectively. The simulation flux tube associated with the Polar/TIDE observation at 1535 UT was initiated at point A (71.8° INV LAT, 1.15 MLT) in Figure 4.5 and intersected the Polar track at D (77.48° INV LAT, 4.4 MLT). The simulated O^+ density at ~7000 km altitude, which was the altitude of Polar satellite in this case, was 7×10^{-3} cm^{-3}. The simulation flux tube associated with the Polar/TIDE observation at 1540 UT was initiated at point A (74.7° INV LAT, 4.9 MLT) and intersected the Polar track at point D (72.1° INV L AT, 4.0 MLT). The resulting simulation O^+ density at the Polar satellite altitude of ~7644 km was about 1.9×10^{-3} cm^{-3}. The corresponding observed O^+ densities were both about 10^{-3} cm^{-3} and within O^+ trough regions as discussed in the work of *Zeng et al.* [2004]. The simulated O^+ density profiles for the Polar track intersection times are displayed in Figures 4.5b and 4.6b.

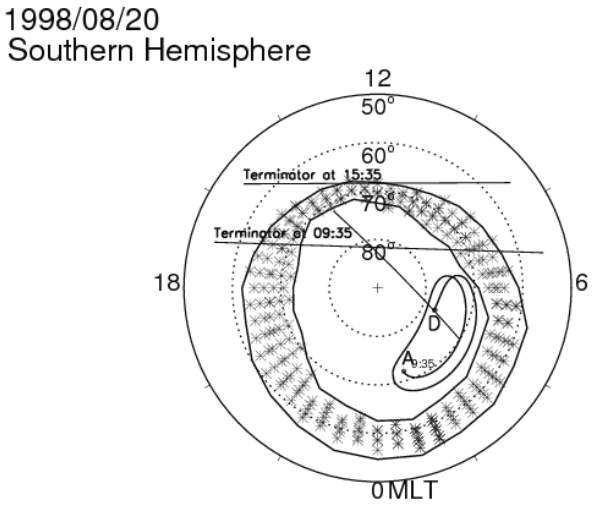

(a)

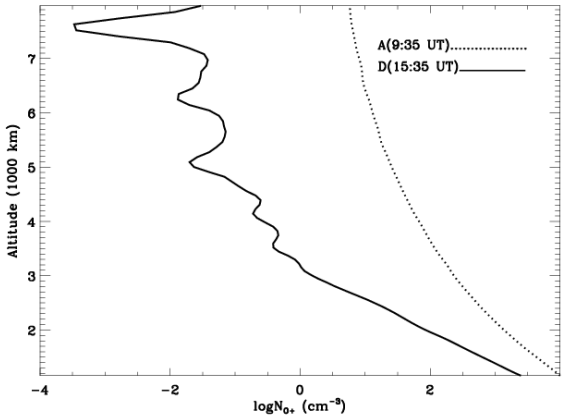

(b)

Figure 4.5 (a) The convection history that started at point at 0935 UT in the southern polar cap on August 20 1998. The flux tube was initially at point A and then continued to convect until reaching the observation point at 1535 UT. The terminators for the start and end times indicates that the *F* region portion of the flux tube along the convection trajectory path was largely in darkness. (b) The simulated O^+ density profiles for point 1535 UT when the flux tube passed at points A, D shown in a.

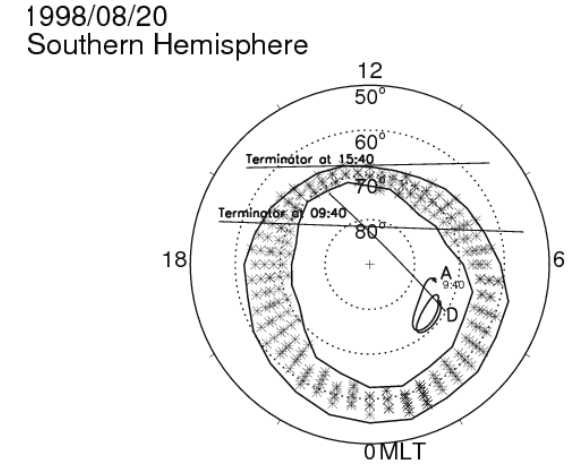

(a)

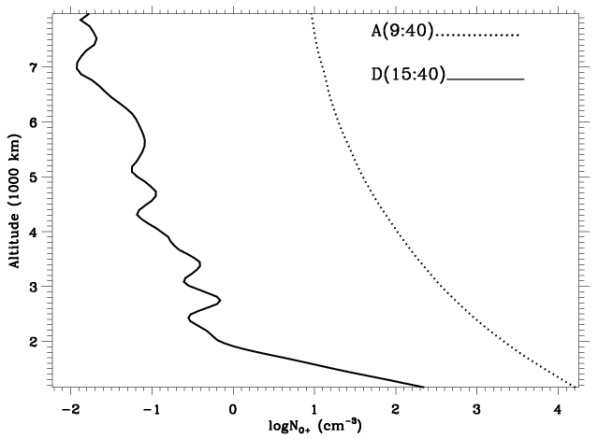

(b)

Figure 4.6 (a) The convection history that started at point at 0940 UT in the southern polar cap on August 20 1998. The flux tube was initially at point A and then continued to convect until reaching the observation point at 1540 UT. The terminators for the start and end times indicates that the *F* region portion of the flux tube along the convection trajectory path was largely in darkness. (b) The simulated O^+ density profiles for point 1540 UT when the flux tube passed at points A, D.

4.2.1.3 O^+ Densities at 1542 UT

The last case for simulation/observation comparison is for the Polar/TIDE observation at 1542 UT. As with the previous cases, the convection trajectory was traced back from 1542 UT at point D in Figure 4.7a (70.5° INV LAT, 3.9 MLT) to 0942 UT at point A (73.2° INV LAT, 4.6 MLT). The convection trajectory at *F* region altitudes was confined completely in darkness and was confined to the polar cap region. The altitude of the Polar spacecraft at 1542 UT was near 8000 km, and the O^+ density measured by Polar/TIDE was ~4.4 cm^{-3}. However, as indicated in simulated O^+ ion density profiles in Figure 4.7b, at similar altitudes the simulated O^+ density was below 0.005 cm^{-3}, i.e., in the trough region.

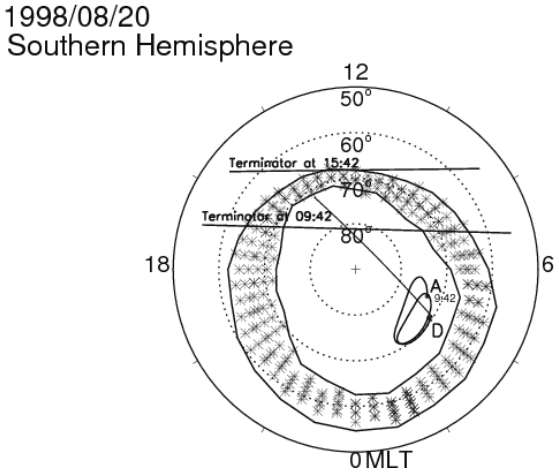

(a)

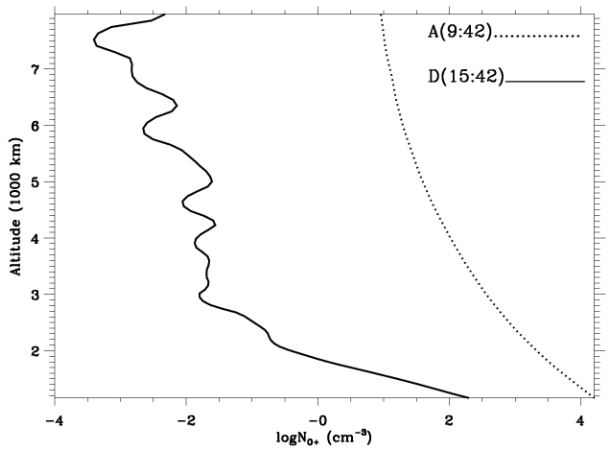

(b)

Figure 4.7 (a) The convection path history that started at point at 0942 UT in the southern polar cap on August 20 1998. The flux tube was initially at point A. The terminators for the start and end times indicates that the *F* region portion of the flux tube along the convection trajectory path was largely in darkness. (b) The simulated O^+ density profiles when the flux tube passed points A, D, respectively.

4.2.1.4 O^+ Simulated Densities along the Polar Path

To compare the general results of O^+ density from the DyFK simulation with the observed O^+ density TIDE profile of the 14 selected points that were confined between 1525 and 1543 UT, we constructed the Weimer model-based trajectory for each of the points that were traced back for ~6 h. Figure 4.8a displays all the constructed Weimer-model based trajectories for the 14 points. At each of the trajectories starting points a simulated flux tube was convected along its own path. The results of the DyFK simulation of O^+ densities at the intersection of the Polar track of each of the flux tube convection trajectories is displayed in Figure 4.8b. This comparison of profiles shows the results of all the simulated points (the solid line) which are in agreement with most of the observed O^+ densities (the dotted line). The first simulated O^+ density trough case started at 1533 UT, approximately 3 min delayed from the first observed O^+ density trough. The simulated O^+ densities troughs were again in agreement with the observed troughs up to 1540 UT, when the observed densities start to recover to higher levels at 1542 UT. However, the simulated densities remained at the trough level beyond the time/location of this point. Possible reasons for this discrepancy will be discussed in the next section.

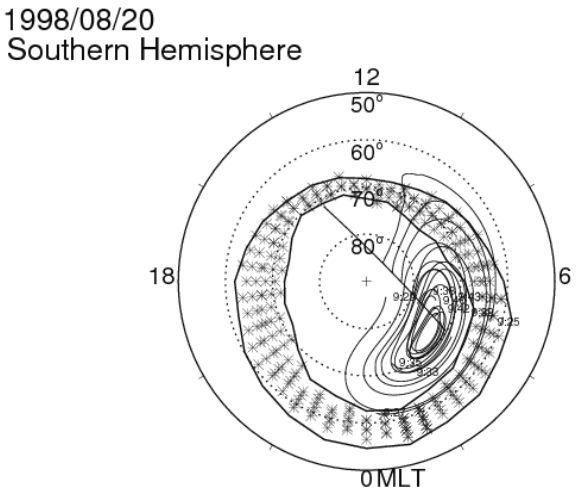

(a)

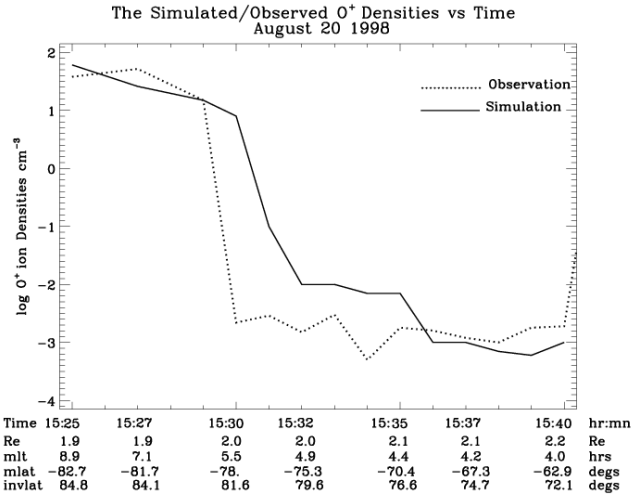

(b)

Figure 4.8 (a) The 14 selected Weimer convection trajectories that are confined between 1525 and 1543 UT, in the southern high-latitude region with their intersections with the estimated auroral oval region. For each trajectory, a simulated flux tube drifts along its path producing the DyFK simulated O^+ density. (b) The simulated O^+ densities at ~1 R_E altitude along the Polar track points verses universal time along with observed O^+ densities.

4.2.1.5 Discussion and Conclusions

We have presented simulation results of O^+ density structure at the ionosphere-magnetosphere interface region and compared it with the O^+ densities observed by Polar/TIDE during its southern polar cap perigee pass from 1525 to 1543 UT on August 20 1998. The observations showed structures including both elevated and trough O^+ density levels. The presented simulations also demonstrate similar O^+ density structures in the polar cap magnetosphere region. For the simulations reported in this paper, we traced the convection trajectories of four points along the Polar track using the empirical ionospheric electric potential model of *Weimer* [2001], incorporating the geophysical and solar wind conditions at the time of the Polar pass. The auroral oval locations were determined by the Ovation model [*Newell et al.*, 2002] and the DMSP observations. After considering Polar/TIDE and Polar/HYDRA electron measurements, we modified the boundary locations of the auroral oval slightly so that the modified auroral oval was approximately consistent with the available DMSP, Polar/HYDRA, and Polar/TIDE observations. Employing the DyFK model for ionospheric plasma transport along those convecting flux tubes, it was found that the simulation results for O^+ densities near Polar spacecraft altitudes were in the range of the O^+ density observations for three of the four locations selected for consideration. However, a substantial difference was observed between the O^+ densities and the simulated densities at 1542 UT, where the observed O^+ density was about 2 orders of magnitude higher than the trough level densities in the associated simulation at this time. In the nominal polar cap region, the primary competing processes in controlling the O^+ ion density are anticipated to be solar photonization and ion-electron recombination in the *F* region and auroral/CIF effects. The auroral processes which were included in this paper included soft electron precipitation and transverse wave heating. As shown in previous DyFK and other simulations [e.g., *Wu et al.*, 1999; *Su et al.*, 1999] soft electron precipitation enhances *F* region plasma production, as well as increasing the electron temperature by Coulomb collisions between the soft electron precipitation and the thermal electron background.

Transverse ion heating [e.g., *Norqvist et al.*, 1998] is suggested to be most likely the resonant heating in the perpendicular direction by Broad-Band Extreme Low-Frequency (BBELF) turbulence. Combining with the mirror force associated with the diverging geomagnetic field, the transversely heated ions are subsequently energized in the parallel direction and driven to higher altitudes.

For the observation made at 1529 UT, the associated convection trajectory would have entered the auroral zone at 1109 UT at point B and exited the auroral region at 1415 UT at point C (cf. Figure 4.4a). The flux tube experienced simulated auroral effects for about 186 min. As seen from.., the simulated O^+ density at Polar altitude (about 6000 km) increased from 1.5 cm^{-3} at point B to ~121 cm^{-3} at point C. This increase could be attributed to enhancements due to the synergistic effects of soft electron precipitation and transverse ion heating. From point C to D in Figure 4.4a, the auroral effects were not operative; the *F* region was in darkness and the electron-ion recombination effects, and gravitational collapse of the enhanced O^+ density plume, appeared to have dominated during this portion of the flux tube's convection history. The O^+ density decreased from 121 cm^{-3} at point C to 14.5 cm^{-3} at point D, which was consistent with the observation results.

Referring to the 10 min trough episode from 1530 UT to 1540 UT in Figures 4.8a, it may be noted that none of the convection trajectories which intersect the Polar track for this interval traversed the estimated auroral region; on the basis of the model oval and empirical electric field model, the flux tubes were trapped inside convection vortices within the polar cap. For the present simulations, the O^+ loss rates due to the recombination of ions and electrons at 300 km altitude were about 2 cm^{-3} s^{-1}. The ionospheric source of O^+ ions tends to be weaker in darkness and if a flux tube is confined in the dark for an extended period of time, there will be reduced O^+ flow to high altitudes. Correspondingly, the pressure gradient force which would support high altitude O^+ density plumes [e.g., *Ganguli*, 1996] was decreased, and thus

the densities at high altitudes declined. Hence, very low O^+ densities in such regions should occur in both in situ observations [*Horita et al.*, 1993; *Zeng et al.*, 2004] and simulations. As noted earlier, a substantial discrepancy occurred between the O^+ density observations and corresponding simulation densities at 1542 UT on August 20 1998: the O^+ density observed by Polar/TIDE was about 4.4 cm^{-3}, while the simulation O^+ density was below 0.01 cm^{-3}. It is quite possible that this is because the real flux tube convection history intersecting with the Polar track actually did include traversal of a region containing elevating auroral processes, somewhat like those flux tubes which intersected the Polar track prior to 1533 UT. However, we did not attempt to further adjust the auroral oval model and/or modify the electric field pattern to facilitate such assumed auroral oval traversal of the 1542 UT associated convection trajectory because the present study is to qualitatively explore the mechanisms that control the O^+ density through structures in the polar cap magnetosphere. Auroral processes such as soft electron precipitation and the wave heating combined will dominate other effects. Meanwhile, in the absence of the auroral processes, the photonization/recombination processes will control the O^+ density.

In summary, using our DyFK model we were able to explore the effects of such dominant processes which lead to either normal or trough O^+ densities and replicate the Polar/TIDE observations for much of the Polar pass displayed. This tentatively suggests that the mechanisms causing the O^+ troughs observed by *Zeng et al.* [2004] may indeed be now understood, as in the presented simulations, in terms of the incorporated competing processes of *F* region recombination in darkness and associated draining of plasma from higher altitudes, versus solar illumination and auroral processes, as governed by convection paths through regions of different processes.

4.2.2 Case 2: August 02 1998 (19:12-19:44 UT)

The observation data of the Polar/TIDE pass on August 02 1998 is displayed in Figure 2.2 which includes O^+ trough and normal densities. In this case we also do full observation/simulation comparisons. We simulate 22 Weimer trajectories and 22 convecting flux tubes which projected to have intersected with the Polar pass. The IMF and the solar wind conditions required by Weimer model to determine the convection patterns are displayed in Figures 4.9 and 4.10 respectively. The data used to derive the Weimer model were the 1-min OMNI data. The data incorporate the transit time of the solar wind to the earth which is 21 minutes for the spacecraft location and measurements.

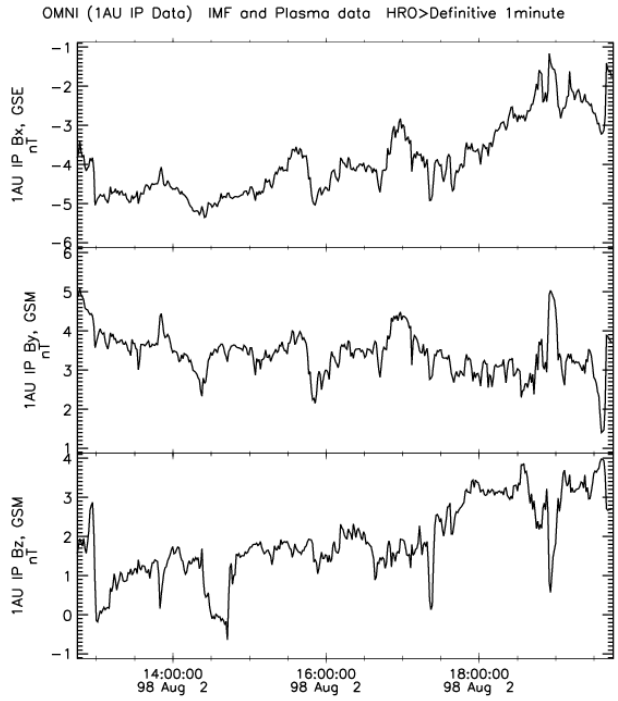

Figure 4.9 The interplanetary magnetic field (IMF) on August 02 1998. The interval from 1245 to 1945 UT corresponds to the 6 hours period plus 21 minutes the transit time prior to Polar/TIDE measurements. Data and plot courtesy of CDA web site: (www.cdaweb.gsfc.nasa.gov/) and provided by R. Lepping at NASA/GSFC.

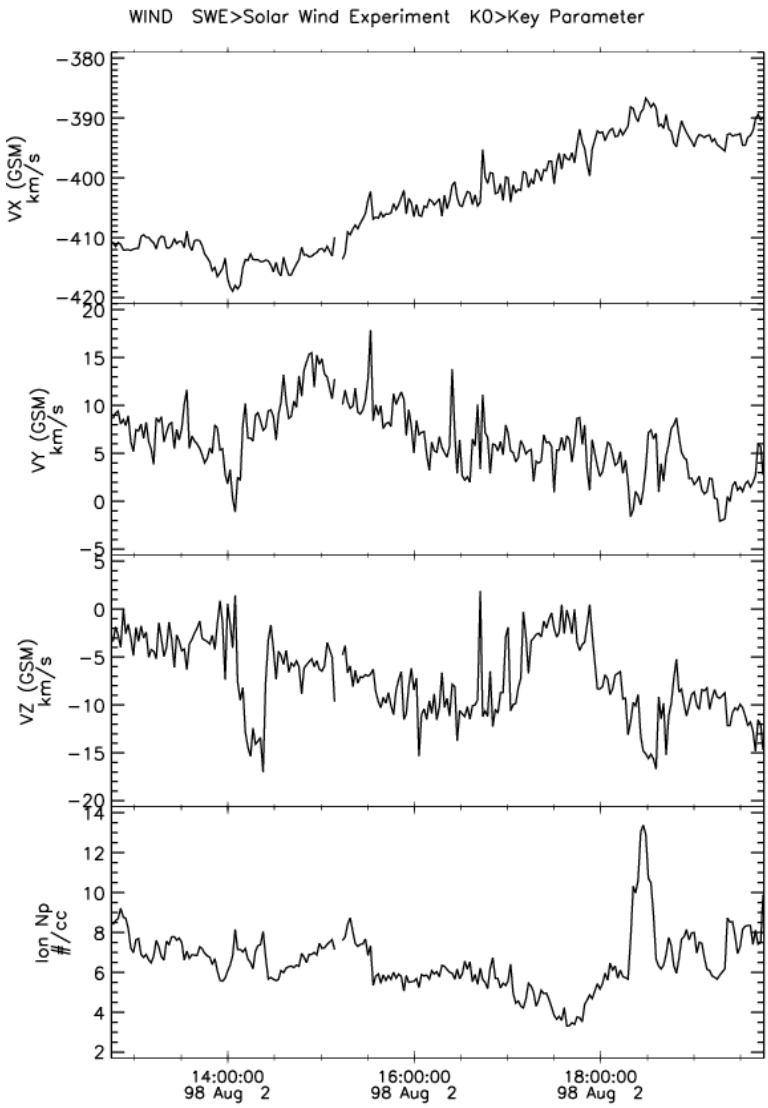

Figure 4.10 The solar wind conditions detected by Wind on August 02 1998. The interval from 1245 to 1945 UT corresponds to the 6 hours period plus 21 minutes the transit time prior to Polar/TIDE measurements. Data and plot courtesy of CDA web site: (www.cdaweb.gsfc.nasa.gov/).

As seen from Figure 4.9 the IMF *By* varied between 2.3 and 5 nT, and *Bz* varied between -1.3 and 5 nT. Figure 4.10 shows the solar wind velocity was about 403 ± 17 km/s, and the solar wind density fluctuated between 3 and 13.8 cm^{-3}.

At the time of this Polar/TIDE pass; the Ovation model [*Newell et al;* 2002] Indicates the auroral equatorward boundary was located at about 70.2 INV LAT/ 18.4 MLT, and the poleward boundary was at 78.59 INV LAT/ 18 MLT. Figure 4.11a shows the Ovation-based auroral oval along with both the DMSP track and the Polar track. We did not modify the boundaries of the Ovation auroral oval; there was no other available observation of the same time of the Polar pass. The Ovation auroral oval is displayed in Figure 4.11b with the 22 relevant convection trajectories.

4.2.2.1 Simulation Results

To simulate the ionospheric plasma transport in the simulated convecting flux tubes and compare the simulated O^+ densities near 6000 km altitude with observations. The following geophysical parameters were adopted to reflect the realistic conditions on August 02 1998: *AP* index = 6, the solar radio activity index $F_{10.7}$ = 113, and the 90 day averaged $F_{10.7}$ = 133. The upper boundary condition of the electron temperature at 3 R_E altitude was set at 3000 K in the polar cap and at 6000 K in the auroral regions. Again, when the flux tubes passes through the aurora boundaries, the aurora process will be turned on with soft electron precipitation and transverse wave heating.

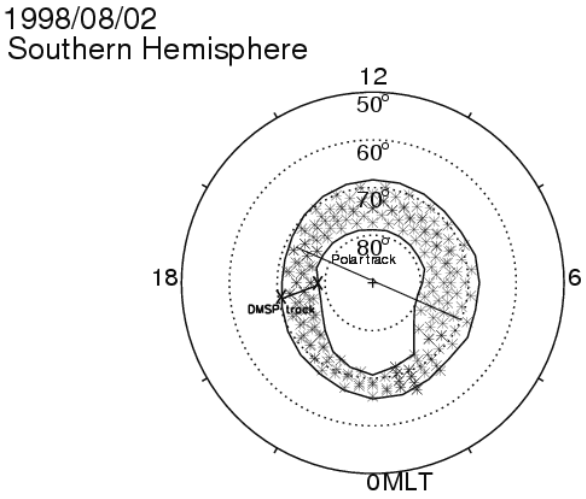

(a)

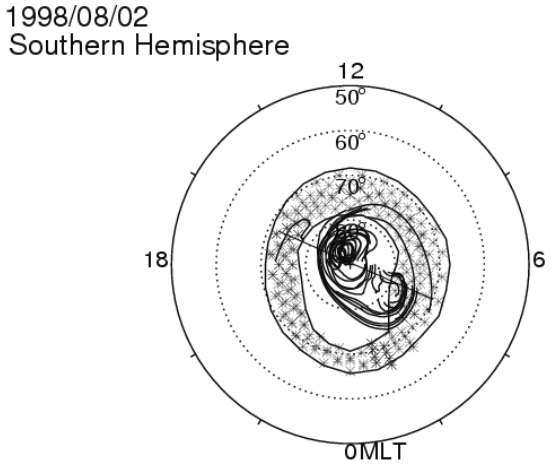

(b)

Figure 4.11 (a) The Ovation-based aurora oval based on DMSP model along with the Polar track trajectory. (b) The 22 selected Weimer convection trajectories that are confined between 1915 and 1940 UT, in the southern high-latitude region with their intersections with the estimated auroral oval region. For each trajectory, a simulated flux tube drifts along its path producing the DyFK simulated O^+ density.

To compare the general results of O^+ density from the DyFK simulation with the observed O^+ density TIDE profile of the 22 selected points that were confined between 1915 and 1940 UT, we follow the same steps as the study of the first case. We first constructed the Weimer model-based trajectory for each of the points that were traced back for ~6 hours. At each of the trajectories starting points a simulated flux tube was convected along its own path. The results of the DyFK simulation of O^+ densities at the intersection of the Polar track of each of the flux tube convection trajectories is displayed in Figure 4.12. This comparison of profiles shows the results of all the simulated points (the solid line) which are in agreement with most of the observed O^+ densities (the dotted line). As seen from the Figure 4.12, the first simulated O^+ density trough case started at 1916 UT, approximately 3 min ahead from the first observed O^+ density drop at 1919 UT. The simulated O^+ densities rise again to normal for 3 minutes to drop to trough level for about 9 minutes from 1919 to 1927UT. At about 1928 the simulated O^+ densities are normal to 1940UT. The simulated troughs were in agreement with the observed troughs for the time between 1923 up to 1927 UT, but the simulated densities started the trough 3 minutes earlier than the observations. Possible reasons for this discrepancy is that the real flux tube convection history intersecting with the Polar track actually did pass through the auroral oval earlier and for longer period of time than the simulated one. Although the Ovation auroral oval was not adjusted nor the electric field pattern was modified, the Ovation auroral oval may not have been presenting the actual boundaries for the real auroral region at the time of Polar pass, or and the Weimer trajectories for the 3 points 1920, 1921, and 1922 UT were not confined totally in the nominal polar cap. However, looking at Figure 4.12 the DyFK simulation line (solid) is reasonably close to the observations.

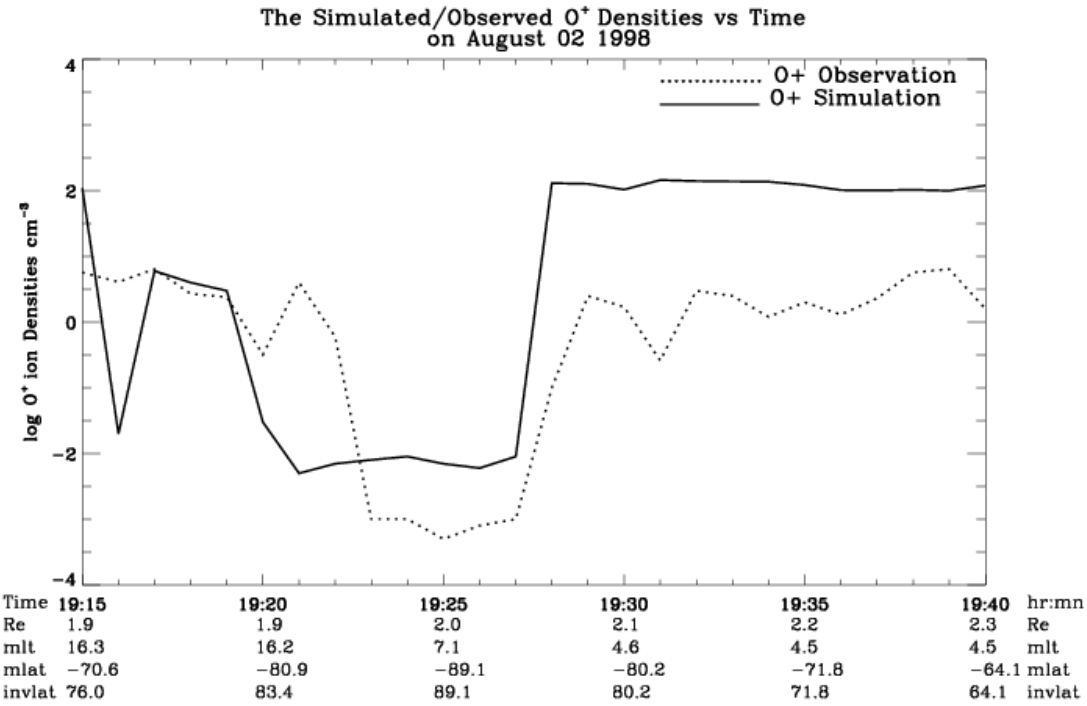

Figure 4.12 The simulated O^+ densities at ~1 R_E altitude along the Polar track points verses universal time along with observed O^+ densities for the case of August 02 1998.

4.2.3 Case 3: June 26 1998 (15:16-15:43 UT)

The observation data of the Polar/TIDE pass on June 26 1998 is displayed in Figure 2.3 which includes O^+ trough and normal densities. For full observation/simulation comparisons, we simulated 21 convection trajectories that were projected to have intersected with the Polar pass. The IMF and the solar wind conditions required by Weimer's model to determine the convection patterns are displayed in Figures 4.13 and 4.14 respectively. As seen from Figure 4.13, IMF *By* varied between 5.5 and 12.5 nT, and *Bz* varied between -5.2 and – 9.4 nT.

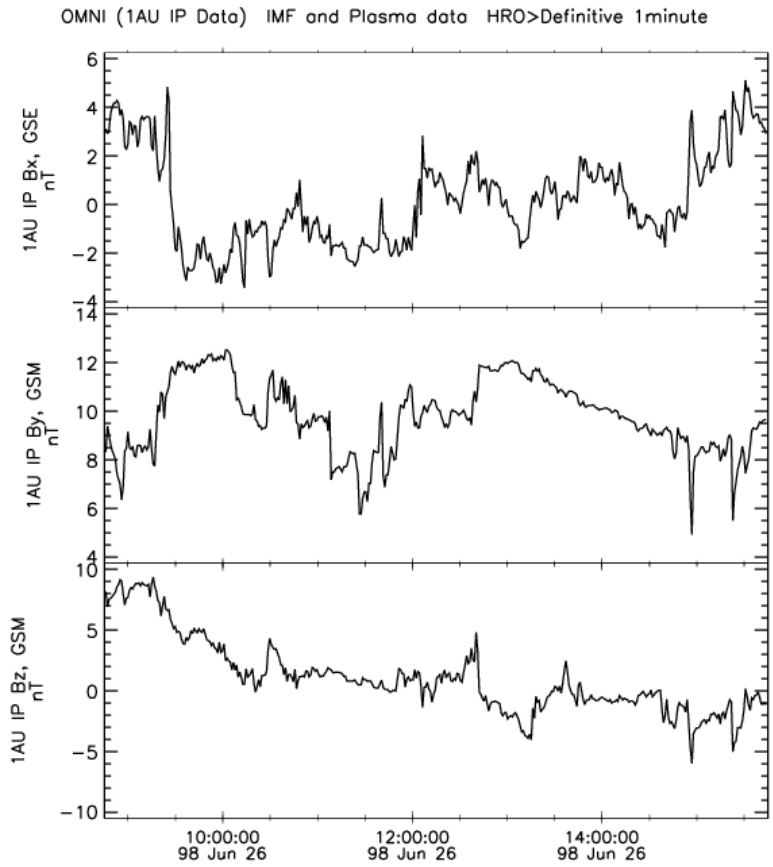

Figure 4.13 The interplanetary magnetic field (IMF) conditions detected by Wind on June 26 1998. The interval from 0900 to 1600 UT corresponds to the 6 h period plus the 11.5 min transit time prior to Polar/TIDE measurements. Data and plot courtesy of CDA web site: (www.cdaweb.gsfc.nasa.gov/) and provided by R. Lepping at NASA/GSFC.

Figure 4.14 shows the solar wind velocity was about 481±27 km/s, and the solar wind density fluctuated between 11.7 and 47.3 cm^{-3}. The data were simulated incorporating the transit time of the Wind data which is 11.5 minutes for the spacecraft location.

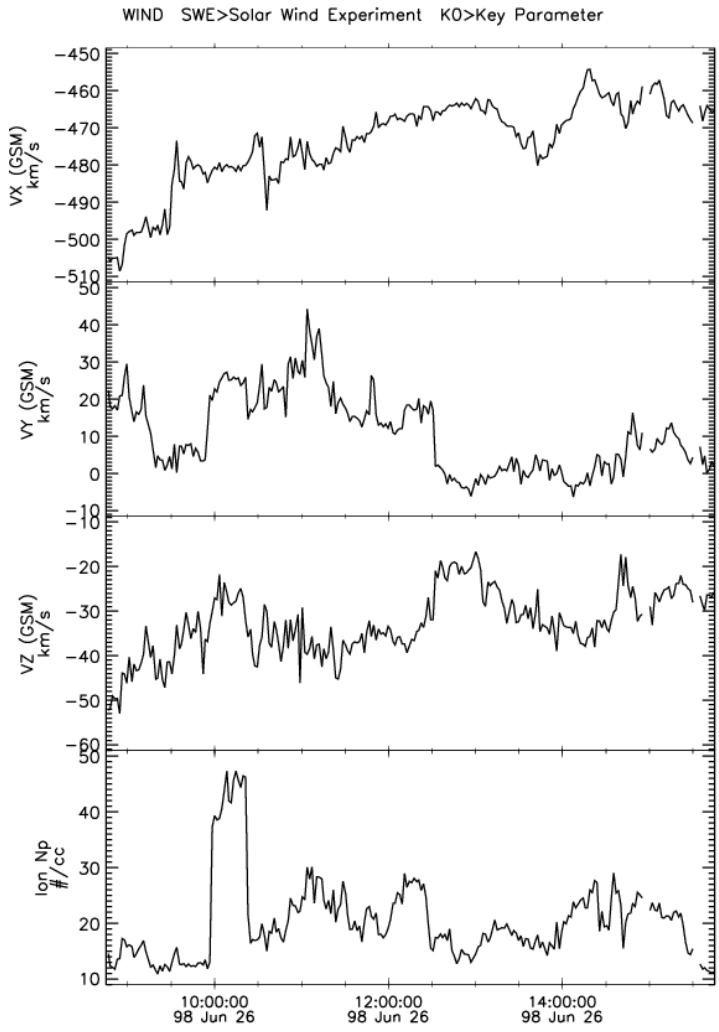

Figure 4.14 The solar wind conditions detected by Wind on June 26 1998. The interval from 0900 to 1600 UT corresponds to the 6 h period plus the 11.5 min transit time prior to Polar/TIDE measurements. Data and plot courtesy of CDA web site: (www.cdaweb.gsfc.nasa.gov/).

The Ovation Model auroral boundary during the Polar pass had the equatorward boundary was located at about 61 INV LAT/ 7 MLT and the poleward boundary at 77.8 INV LAT/ 6.8 MLT. Figure 4.15a shows the Ovation-based auroral oval along with both the DMSP track and the Polar track. In this case other measurements were available to modify the Oval auroral boundaries. The modified boundaries of the Ovation auroral oval were based on the Polar/TIDE

electron observations [*Scudder et al.*, 1995] measurements indicated that the invariant latitude of the poleward boundary of the auroral oval was approximately 71 and 73 INV LAT between 17.5-17.6 ML. Based on the Polar/TIDE measurements the auroral oval is modified and displayed in Figure 4.15b with 21 relevant convection trajectories.

4.2.3.1 Simulation Results

We simulate the ionospheric plasma transport in these convecting flux tubes and compare the simulated O^+ densities near 6000 km altitude with observations. The following geophysical parameters were adopted to reflect the realistic conditions on June 26 1998: *AP* index = 42, the solar radio activity index $F_{10.7}$ = 113, and the 90 day averaged $F_{10.7}$ = 141. Again, the upper boundary condition of the electron temperature at 3 R_E altitude was set at 3000 K in the polar cap and at 6000 K in the auroral regions. Also, like the previous two cases, the auroral processes include the soft electron precipitation and the transverse wave heating. To compare the general results of O^+ density from the DyFK simulation with the observed O^+ density TIDE profile of the 21 selected points that were confined between 1515 and 1543 UT.

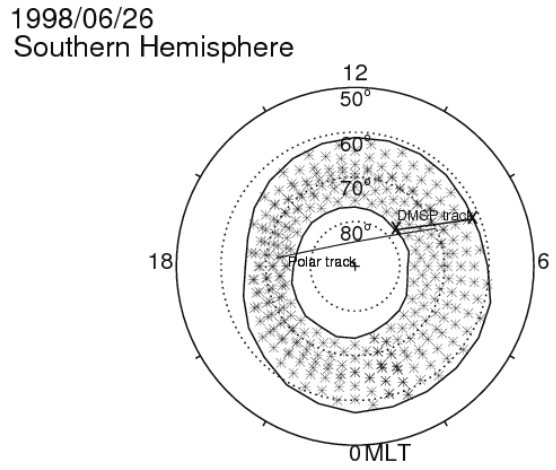

(a)

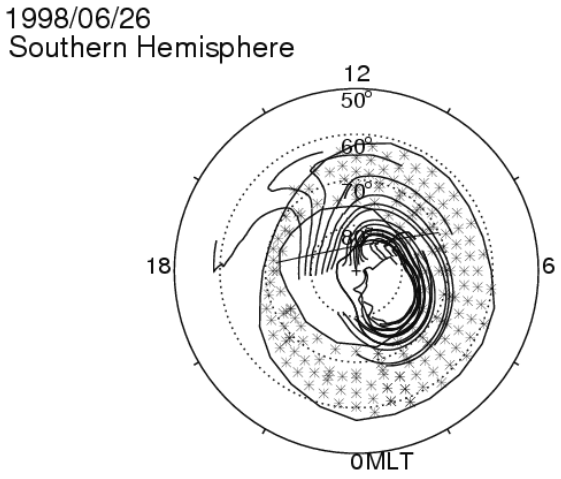

(b)

Figure 4.15 (a) The Ovation-based aurora oval based on DMSP model along with the Polar track trajectory. (b) The 21 selected Weimer convection trajectories that are confined between 1915 and 1940 UT, in the southern high-latitude region with their intersections with the estimated auroral oval region. For each trajectory, a simulated flux tube drifts along its path producing the DyFK simulated O^+ density.

Following the same steps as the study of the previous two cases, we first constructed the Weimer model-based trajectory for each of the points that were traced back for ~6 hours. At each of the trajectories starting points a simulated flux tube was convected along its own path. The results of the DyFK simulation of O^+ densities at the intersection of the Polar track of each of the flux tube convection trajectories is displayed in Figure 4.16.

This comparison of profiles shows the results of all the simulated points (the solid line). The first trough case in the observation is at 1520 UT; however the O^+ ion simulation is normal and does not suffer any trough until it reaches 1527 UT while the observation starts the second trough O^+ densities at 1525 UT. However, both the simulation and observation remain in trough region up to 1536 UT. We consider the O^+ ion density simulation is in agreement with most of the observed O^+ densities. As seen from the Figure 4.16, the first simulated O^+ density deep drop started at 1528 UT, but approximately 2 min delayed from the first observed O^+ density trough at 1525 UT. Possible reasons for the discrepancy and the delay is that the real flux tube convection history intersecting with the Polar track actually did pass through the auroral oval earlier and for longer period of time than the simulated one. Although the Ovation auroral oval was adjusted, the electric field pattern was not modified. The conclusion is that the Ovation auroral oval may not have presented the actual boundaries for the real auroral oval at the time of Polar pass. Another possibility is that the actual Weimer trajectories for the points 1520, 1525, 1526, and 1527 UT were not confined totally in the nominal polar cap. However, looking at Figure 4.16 the DyFK simulation line (solid) is reasonably close to the observation dotted line.

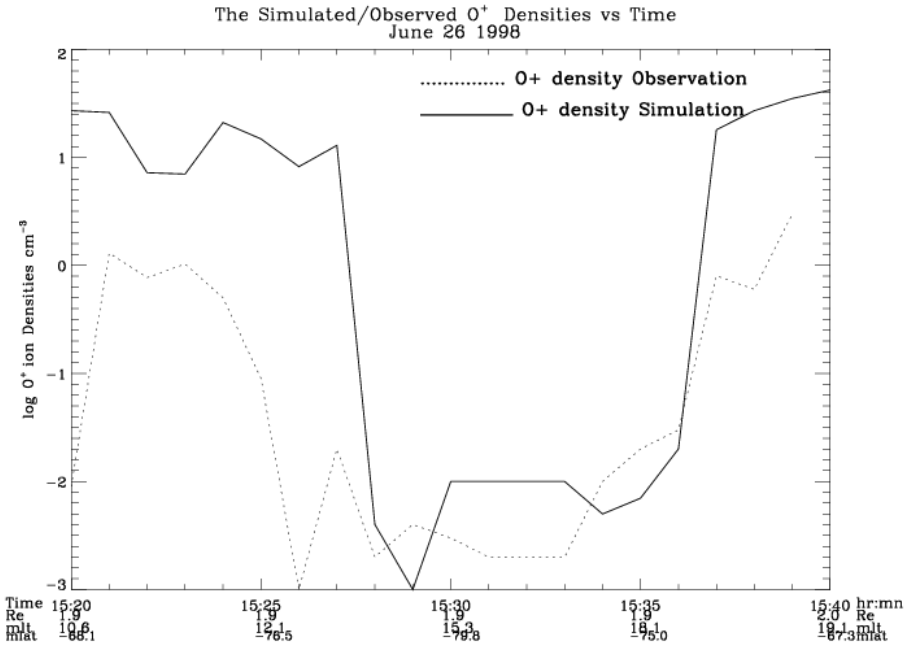

Figure 4.16 The simulated O^+ densities at ~1 R_E altitude along the Polar track points verses universal time along with observed O^+ densities.

4.2.4 Case 4: December 02 1997 (14:52-15:20 UT)

The observation data of the Polar/TIDE pass on December 02 1997 is displayed in Figure 2.4 which includes O^+ trough and normal densities. For full observation/simulation comparisons, we simulated 25 Weimer convection trajectories projected to have intersected with the Polar pass. The solar wind and IMF conditions required by Weimer's model to determine the convection patterns are displayed in Figures 4.17 and 4.18 respectively. The transit time is approximated about 58 minutes for the average given solar wind velocity Vs= 334±17 km/s.

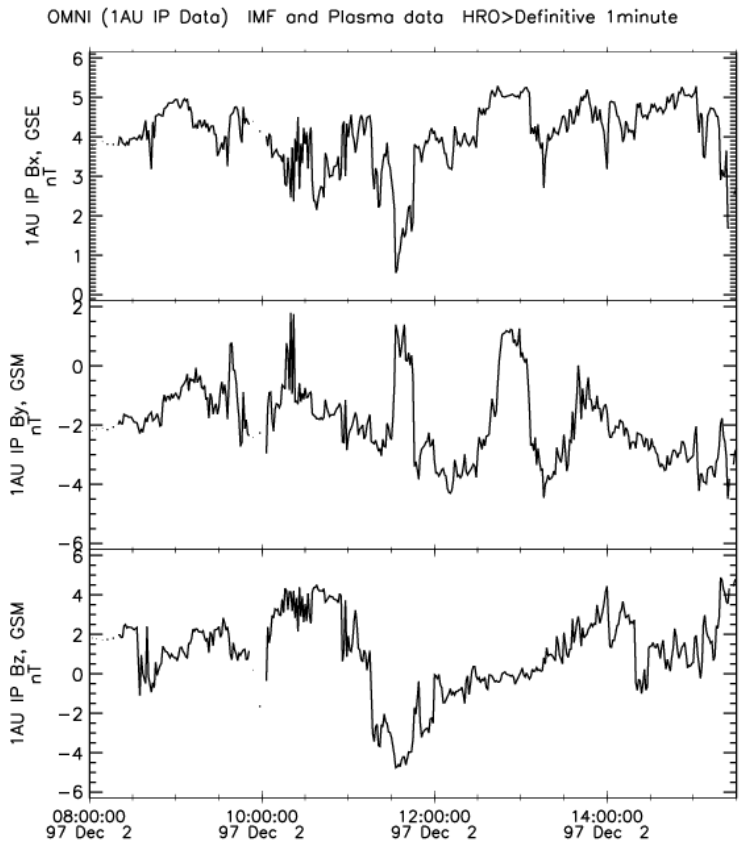

Figure 4.17 The interplanetary magnetic field (IMF) detected by Wind on December 02 1997. The interval from 0900 to 1600 UT corresponds to the 6 h period plus the 58 min transit time prior to Polar/TIDE measurements. Data and plot courtesy of CDA web site: (www.cdaweb.gsfc.nasa.gov/) and provided by R. Lepping at NASA/GSFC.

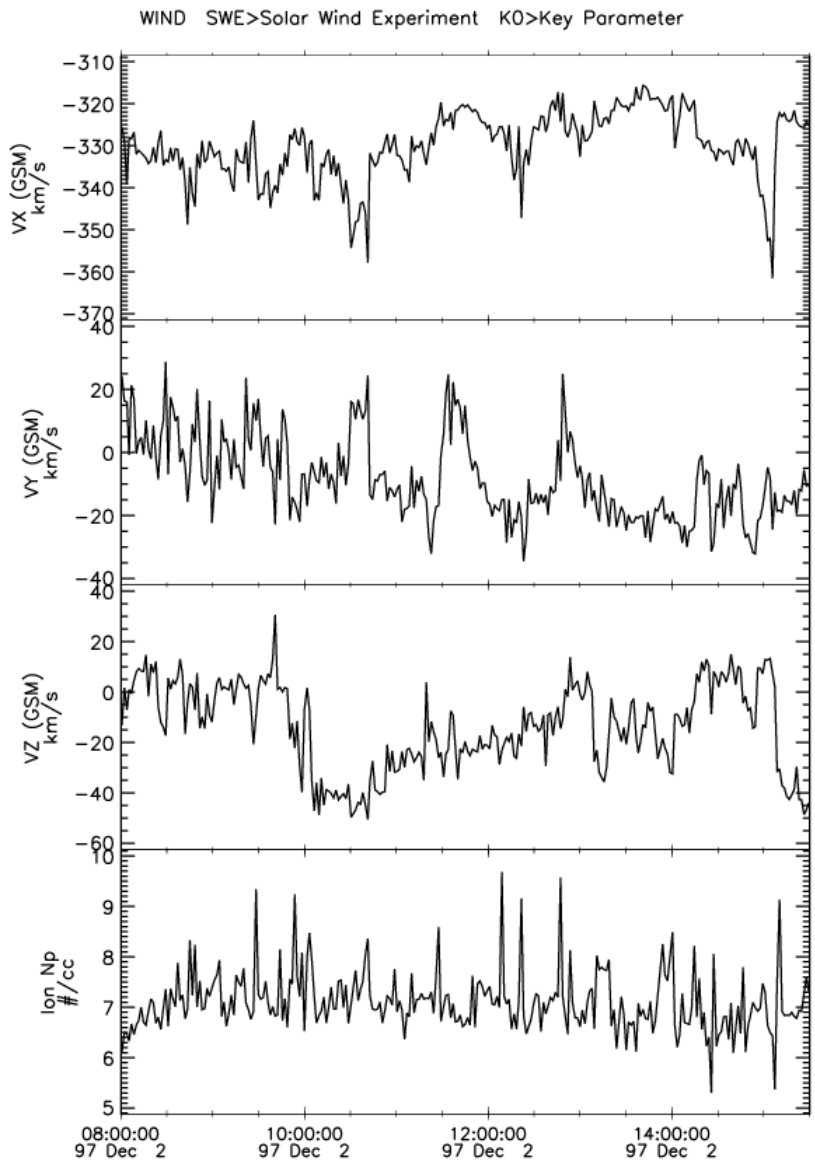

Figure 4.18 The solar wind conditions detected by Wind on December 02 1997. The interval from 0900 to 1600 UT corresponds to the 6 h period plus the 58 min transit time prior to Polar/TIDE measurements. Data and plot courtesy of CDA web site: (www.cdaweb.gsfc.nasa.gov/).

As seen from Figure 4.17, IMF *By* fluctuated between -4.5 and 1.4 nT, and IMF *Bz* varied between -4.3 and 4.7 nT. The solar wind density fluctuated between 5.3 and 9.7 cm^{-3}. The data were conducted from 8:00 to 15:20 UT incorporating the transit.

The Ovation Model auroral boundary during the Polar pass had the equatorward boundary was located at about 68.4 INV LAT/ 18.8 MLT and the poleward boundaries at 78.3 INV LAT/ 18.2 MLT, Figure 4.19a shows the Ovation-based auroral oval along with both the DMSP track and the Polar track. The modified boundaries of the Ovation auroral oval were based on the Polar/HYDRA electron observations [*Scudder et al.*, 1995]. The Polar/HYDRA measurements indicated that the invariant latitude of the poleward boundary of the auroral oval was approximately 66 and 67 INV LAT between 13 and 14 MLT, the modified auroral oval is displayed in Figure 4.19b with the 25 relevant convection trajectories.

4.2.4.1 Simulation Results

First we note that the observation day is in the summer time over the southern polar cap, where the plasma in the flux tube is exposed to the sunlight for long time during the convection. The solar EUV radiation ionizes the atmosphere and produces photoelectrons with super thermal energy which enhances the ambipolar electric field then drive polar wind outflow [e.g., A*xford,* 1968; *Lemaire,* 1972]. We simulate the ionospheric plasma transport in the convecting flux tubes and compare the simulated O^+ densities near 6000 km altitude with observations. The following geophysical parameters were adopted to reflect the realistic conditions on December 02 1997: *AP* index = 4, the daily solar radio activity index $F_{10.7}$ = 114, and the 90 day averaged $F_{10.7}$ = 93. The upper boundary condition of the electron temperature at 3 R_E altitude was set at 3000 K in the polar cap and at 6000 K in the auroral regions.

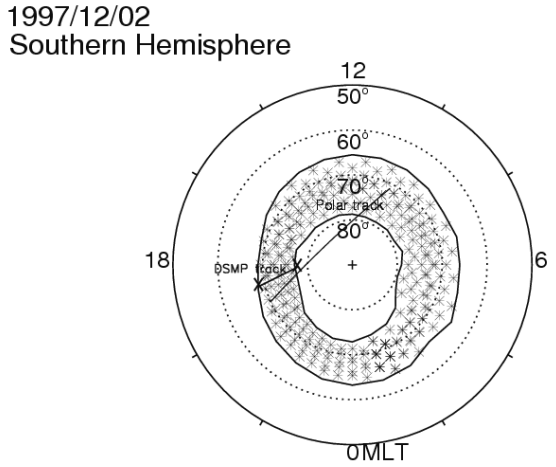

(a)

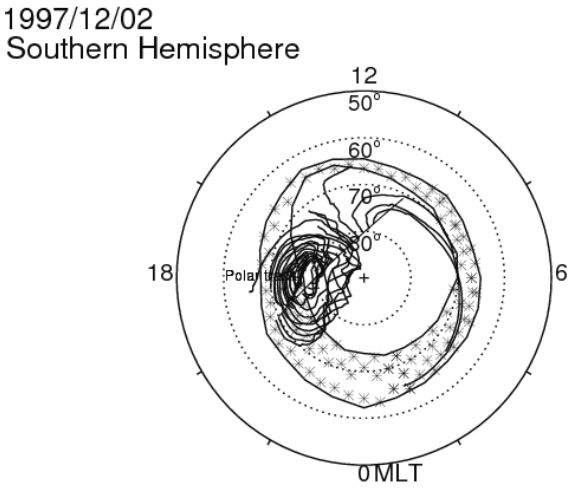

(b)

Figure 4.19 (a) The Ovation-based aurora oval based on DMSP model along with the Polar track trajectory. (b) The 25 selected Weimer convection trajectories that are confined between 1915 and 1940 UT, in the southern high-latitude region with their intersections with the estimated auroral oval region. For each trajectory, a simulated flux tube drifts along its path producing the DyFK simulated O^+ density.

For the auroral processes, the soft electron precipitation with energies and energy fluxes are 100 eV and 1 erg cm^{-2} s^{-2}. The auroral electric field wave spectral density profile was 0.3 x 10^{-6} V^2 m^{-2} Hz^{-1}.

To compare the general results of O^+ density from the DyFK simulation with the observed O^+ density profile of the 25 selected points that were confined between 1455 and 1520 UT. Following the same previous steps of simulation/observation comparison, we constructed the Weimer model-based trajectory for each of the points that were traced back for ~ 6 h. At each of the trajectories starting points a simulated flux tube was convected along its own path. As mentioned before, the flux tube is exposed to the aurora processes when it enters the auroral region. The results of the DyFK simulation of O^+ densities for all the 25 trajectories at the intersection of the Polar track of each of the flux tubes is displayed in Figure 4.20. The comparison of two profiles shows that the simulation results (the solid line) are in discrepancy with the observation. The observation show high fluctuation between the trough and normal O^+ ion densities. The first data points give normal O^+ ion density, as time pass, the densities declines and the first trough case was about 1459 UT, then the O^+ ion densities rose to normal at ~ 15:00 UT, it dropped again at ~ 1514 UT to trough level. The O^+ ion density is back suddenly to normal density at 15:17 UT but suddenly it drop again at 15:18 UT, right after this point it started to rise. Meanwhile the O^+ ion simulation results show one O^+ ion trough at ~ 1528 UT, it rises to normal densities. The simulated O^+ ion kept at that level and higher to ~ 15:20 UT. Based on the above results, we consider the O^+ ion density simulation is in disagreement with most of the observed O^+ densities. Possible reasons for this discrepancy and the time delay in the simulation trough comparison are many. One of the reasons could be indicated from the high fluctuation in the data, the nature of the observed trough maybe temporal not spatial. Another possibility is the observed flux tube convection history that intersected with the Polar track may stay in the polar cap nominal area much earlier and for longer period of time than the simulated one. Although the Ovation auroral oval

was adjusted as described in section 4.1, the conclusion is that the Ovation auroral oval may not represented the actual boundary for the time of the observation. Most of the simulated trajectories intersected with the auroral region where the soft electron precipitation and the wave heating are the dominant processes that elevate the O^+ densities to high altitudes.

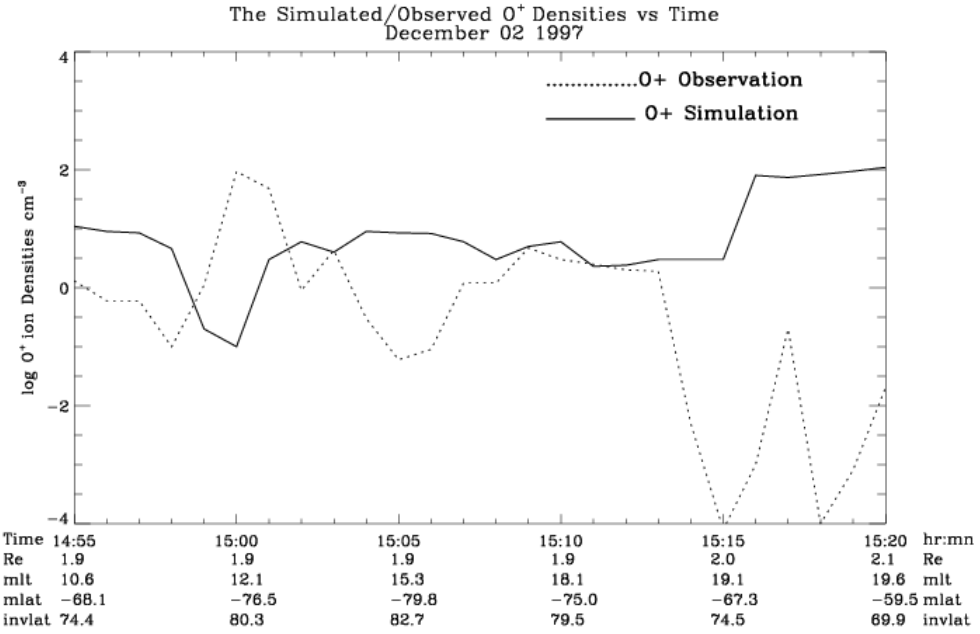

Figure 4.20 The simulated O^+ densities at ~1 R_E altitude along the Polar track points verses universal time along with observed O^+ densities for the case of December 02 1997.

4.3. The H^+ Simulated Densities along the Polar Path

To account for the H^+ densities from the DyFK model of each studied case of the O^+ trough simulations, we simulated H^+ ion densities along with O^+ ion densities at the intersection of the Polar track of each of the flux tube convection trajectories of all 4 cases as shown in Figure 4.21. The profile shows the simulated H^+ density of each studied case did not vary significantly and remained steady, no H^+ troughs correlated with the O^+ troughs during the time of observation. The statistical study done by *Zeng et al* [2004] shows that the calculations of O^+ densities at the trough region includes both H^+ and O^+ ions. The exclusive extraction of H^+ ion densities is a cumbersome process when it is calculated in the O^+ trough region [*Zeng*, privet communication, 2004]. However, the DyFK model simulations produced high H^+ densities in that region despite the expectations of producing very low H^+ ions. Possible reasons for this significant discrepancy is as follow; the densities of H^+ ions are in general correlated with the O^+ ions present and production at lower altitudes H^+ ions is controlled mainly by O^+ charge exchange [e.g., *Wilson et al.*, 1992]. At high altitudes another process is affecting the H^+ present and densities and even velocity, which is the enhanced ambipolar electric field [e.g., *Ho et al,* 1992; *Su et al,* 1998]. However, in the auroral region, O^+ ions respond strongly to the ion-wave heating resonance. This leads H^+ densities reach about 1 order of magnitudeless than the O^+ densities [*Wu et al,* 1999; *Tu et al*., 2004]. However, the ExB convection might drag the high electrons densities at high altitudes that were elevated already in the auroral region to the nominal polar cap and/or the solar illumination during the flux tubes convection. The presence of high electron densities generates a potential difference in the ionosphere-magnetosphere region that in turn forms an ambipolar (parallel) electric field. This local electric field could be strong enough to elevate H^+ ions upward in the nominal polar cap. The H^+ densities at Polar/TIDE altitude are not directly associated with the O^+ densities in DyFK model because of the different competing processes governing the plasma in the flux tube. Figure 4.21 maps all Polar/TIDE study cases during a

time span of 20 minutes observations where it includes the O^+ trough regions in each data set.

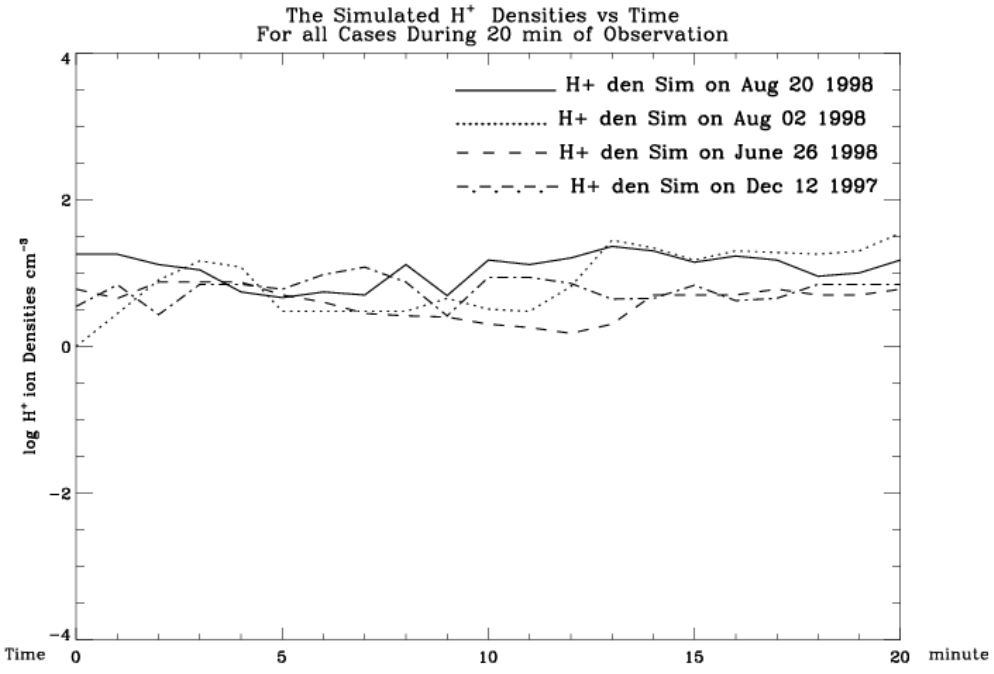

Figure 4.21 The simulated H^+ densities at ~1 R_E altitude along the Polar tracks points verses 20 minutes of observations for all 4 cases: August 20 1998, August 02 1998, June 26 1998, and December 02 1997 covering the O^+ trough regions.

4.4 Conclusions

Spacecraft-based in situ observations have indicated considerable variability in O^+ densities in the polar cap ionosphere-magnetosphere region near 6000 km altitude, from above 10 cm^{-3} to lower than 0.01 cm^{-3}. Regions with densities in the low range have been referred to as O^+ density troughs or ion depletion zones at these altitudes. We used the Dynamic Fluid-Kinetic (DyFK) ionospheric plasma transport model to simulate O^+ density profiles under various

conditions, in order to reproduce O^+ densities which were observed by the Thermal Ion Dynamics Experiment (TIDE) on the Polar spacecraft. We studied 4 different cases near Polar perigee; August 20 1998, August 02 1998, June 26 1998, and December 02 1997. We used solar wind parameters and IMF conditions as inputs driving the time-varying high-latitude electric potential model. In DyFK simulations we incorporated auroral processes which involved the effects of soft electron precipitation and wave-driven transverse ion heating. We simulated the ionosphere-magnetosphere plasma transport and the associated O^+ bulk parameter profiles within many flux tubes convecting in the high-latitude region in each case. Using our DyFK model we were able to explore the effects of the dominant processes which lead to either normal or trough O^+ densities and compared it with the Polar/TIDE observations for each case. 3 out of 4 cases did agree reasonably with much of the Polar observations, while the fourth one had a significant discrepancy. A possible reason for a discrepancy is that the real flux tube convection history intersecting with the Polar track may not pass through the auroral oval earlier and for the same period of time than the simulated one. Although the Ovation auroral oval was not adjusted nor the electric field pattern was modified, the Ovation auroral oval may be not representative of the actual boundaries for the real auroral region at the time of Polar pass, or and the Weimer trajectories were not accurate for the time of observations.

For the fourth case, the simulation results had a strong disagreement with the observations. It could be that the trough in this case was temporal not spatial.

As we concluded, the principal competing processes controlling the O^+ density levels at the ionosphere-magnetosphere coupling region are: first the auroral processes, which elevate the O^+ densities in the ~6000 km altitude region, second are the effects of *F* region O^+-electron recombination in darkness, which decrease the O^+ densities at higher altitudes through draining to the reduced *F* region ionosphere. However, depending chiefly upon the flux tube convection trajectories and their relationship to estimated auroral oval locations, that was the main effective factor that determined most of our O^+ density results or in other words where and when both

elevated and trough-like densities could occur at ~6000 km altitudes in the simulations. The observed trough could be spatial or temporal or both depending on the location and the history of the convection of flux tube. In summary, we have presented a qualitatively exploration of the mechanisms that effect the O^+ densities trough structures in the polar cap ionosphere-magnetosphere region and understood the controlling processes of O^+ ion density.

CHAPTER 5

ELECTRON ENERGIZATION BY ALFVEN WAVES AND ITS AFFECTS ON AURORAL IONOSPHERIC PLASMA TRANSPORT

5.1 Alfvén Waves in the Ionosphere-Magnetosphere Region

Research on Alfvén waves has been conducted in detail in many studies [e.g., *Thompson and Lysak.*, 1996**;** *Andersson et al.,* 2002; *Kletzing and Hu.,* 2001**;** *Chaston et al.,* 1999], where the precipitating electrons in the auroral region are occasionally associated with Alfvénic parallel electric fields. Studies of dispersive Alfvén waves show that these waves accelerate electrons down toward the ionosphere region [*Hasegawa,* 1976]. Alfvén waves under certain conditions generate a field-aligned parallel electric field $E_{||}$ which drives the electron acceleration n downward [e.g., *Kletzing and Hu.,* 2001**;** *Chaston et al.,* 2001; 2002; *Anderson et al*., 2002]. These electrons might have burst events when electrons velocity exceeds Alfvén phase speed [*Andersson et al*., 2002]. As mentioned before, the electron acceleration is strongly dependent on the composition of the plasma and its density variation with altitude [e.g., *Kletzing and Hu.,* 2001; *Chaston et al*., 2000] and the phase speed profile [e.g., *Su et al.,* 2004]. It is been reported that Alfvén waves propagation may influence the bulk oxygen energies which may effect their out flow [e.g., *Chaston et al*, 2003].

Many studies have reported an association between the propagation of Alfvén waves, the electron heating/burst and the increase in O^+ ions out flow [e.g., *Chaston et al,* 2004]. The search for the mechanisms that contribute to O^+ ion outflow through the interaction of Alfvén waves with the ionosphere-magnetosphere plasma is what motivated the topic of this chapter. In addition, we explore the behavior and the effects of continuous Alfvén wave propagation with its associated parallel electric field through simulation. The simulation starts by the DyFK model generating polar cap ionosphere-magnetosphere region density profiles [e.g., *Estep et al,* 1999], which form the background plasma for Alfvén wave propagation simulated by the Gyro-Fluid

model [*Jones and Parker*, 2003; *Jones*, 2004]. This study shows the effect of simulated parallel electrics fields on the evolution of the magnetosheath electrons by applying a test particle method [*Su et al*., 2004]. Then we study the consequent evolution of O^+ ion densities and their outflows development in the ionosphere-magnetosphere region. This work is designed by employing the three models working in iteration. A review of the simulation models used in this investigation is displayed next.

5.2 The Simulation Models with the Initial Production

We begin by producing a plasma density profile which reproduces electron time dispersive signatures by propagating an Alfvén wave with its associate parallel electric field under certain initial conditions used to launch the wave.

The Dynamic Fluid-Kinetic DyFK model simulated high-latitude plasma structure that could reflect a possible realistic auroral background plasma environment that would shape the propagating Alfvén waves and its phase speed profile (see eq 3.16). The DyFK model simulated an H^+, O^+ and e^- density structure representing the most probable physical conditions manifested in the formation of an auroral flux tube. More details are in the next section 5.2.1.

To form an Alfvén wave traveling from the upper part of the magnetosphere region downward along the field line to the ionosphere and to generate a parallel electric field, the one-dimensional Gyro-Fluid code was employed. The wave was initialized at a specific altitude with an electron density perturbation. The perturbation generated an Alfvén wave with a wave length and wave number chosen to be comparable with observation.

The expected interaction between the generated Alfvénic parallel electric field with magnetosheath electrons is simulated with the test particle wave/particle interaction. The test particle code demonstrates the electron acceleration and the kinetic effects of the generated parallel electric field ($E_{||}$) on these electrons. The three models DyFK, Gyro-Fluid and test

particle code are linked together sequentially but not self consistently. More details about every model production are in the following section.

5.2.1 The DyFK Density Profile

We first aim to produce a simulated plasma density profile that would be present in the auroral oval environment and allow for the Alfvénic parallel electric field to produce field-aligned electron acceleration/burst. To account for normal conditions that existed in the auroral oval, the DyFK model simulated the ionospheric plasma transport in a flux tube located in the polar cap boundary at ~ 70˚ latitude along the geomagnetic field line. The flux tube extended from the lower (ionosphere) ~400 km to the upper (magnetosphere) about 40,000 km altitude. Even though this flux tube was chosen with some arbitrariness, the plasma density structure reflected possible realistic conditions at high latitude/polar cap ionosphere/magnetosphere region where DyFK model adopted the geophysical parameters of 20 August 1998 case [*Jaafari et al*; 2008]. This choice was based on the fact that the solar/geophysical parameters at that day were considered to be a typical and normal for an average day. The following conditions were the geophysical parameters that existed on that day and was adopted by the DyFK simulation; *AP* index = 17, the solar radio activity index $F_{10.7}$ = 142, and the 90 day averaged $F_{10.7}$ = 133. The DyFK model initiated a typical flux tube for a developed polar wind profile located at the specified location in the aurora boundary, which is based on the fact that Alfvén waves were observed mostly in the aurora region boundaries with the polar cap. The flux tube ran first for some time to reach quasi-steady state density profile. The plasma in the flux tube is composed, as mentioned, of three species e^- , H^+ and O^+ where $n_e = n_H + n_O$. It should be noted that after attaining the plasma profile, we slightly modified the original H^+ density profile, the H^+ densities sustained the $1cm^{-3}$ value at high altitudes (above 13,000 km) instead of dropping to lower values for reasons will be explained in the following section.

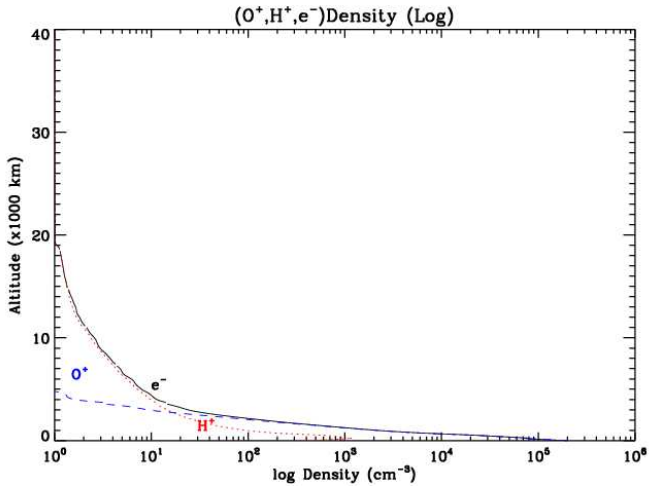

(a)

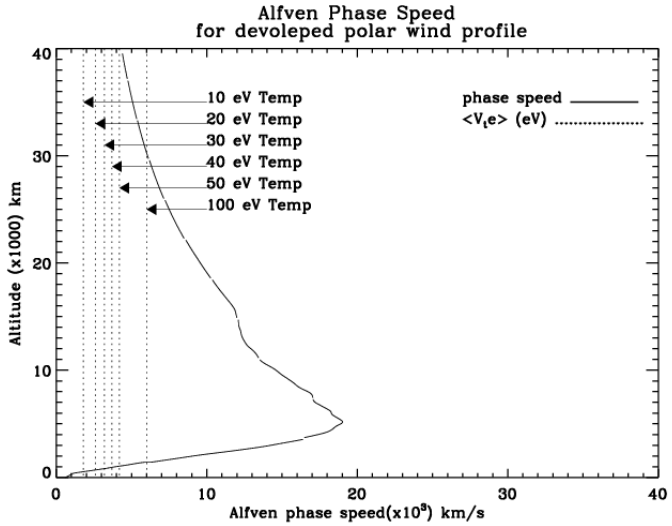

(b)

Figure 5.1 (a) The generated DyFK density profile of O^+, H^+ and e^- for the developed polar wind profile high-latitude flux tube**.** (b) The phase speed of the dispersive Alfvén wave that is associated with the initial plasma density profile.

Figure 5.1a shows the density of e^- , H^+ and O^+ of the developed polar wind profile, where the solid, dashed, and long dashed lines present e^-, H^+, and O^+ densities respectively.

We assumed that all three species will have the same temperature, 2 eV in the lower boundary rising to 100 eV at the upper boundary. The temperature model used was based on [*Lysak et al*., 1996] and given by the following equation $T = 2 + 98 \tanh\left(r - 1.0157\right)$ eV.

The local plasma density structure is essential for determining the Alfvén wave phase speed profile [*Su et al*., 2004]; because the Alfvén phase speed is tied to the surrounding plasma density and its composition (see the dispersive Alfvén wave equation 3.16) more details are displayed in the next section.

5.2.2 Alfvén Wave Properties

As mentioned, the DyFK model simulated the flux tube along a magnetic field line extended to about 40,000 km altitude. The simulated plasma density structure is presented in Figure 5.1a. The particles in the flux tube (with O^+, H^+, e^-) reached a quasi-steady state.

To initiate an Alfvén wave propagating down ward toward the ionosphere region, an electron density perturbation of a single Gaussian pulse was initialized in Gyro-Fluid model at the top of the DyFK simulated flux tube. The pulse was located at 32,000 km altitude (which respond to 80% of the flux tube) with an amplitude of A= 0.5 cm^{-3}. The perturbation launched the electromagnetic Alfvén wave with a wave length of $\lambda_\perp =$ 6.3 km where the wave number was set to $k_\perp$=1 km^{-1} at ~ 6700 km altitude which is comparable to the observations [e.g., *Stasiewicz et al*., 2000]. It has been demonstrated by many that, along with these initial conditions, the Alfvén phase speed plays a critical role in generating suitable conditions for the formation of the electron heating/burst [e.g., *Chaston et al.*, 2003; *Su et al*., 2004; 2006]. To address this issue in more details we display the Alfvén phase speed associated with the generated density profile in Figure 5.1b. The profile of the Alfvén phase speed determines

whether the electrons could be trapped by the wave and experience the burst event or not. Also it predicts the location and range of electron acceleration. Figure 5.1b shows the Alfvén wave phase speed (solid line) rise slowly (from the lower altitudes) to reach a maximum value of $V_A \approx$ 20 x 10^3 km/s at about 6000 km altitude, but then it drops gradually along the top of the flux tube. Also in this Figure, we show 6 dotted vertical lines. These lines present 6 groups of electrons that possess 10, 20, 30, 40, 50, 100 eV temperatures. In the acceleration regions we expect to witness a wide range of electrons acceleration. The acceleration range is located anywhere below the peak of the Alfvén phase speed and the intersection location. The electrons in that region may accelerate to exceed the wave speed and experience the burst signature.

The plasma environment that had been set up by the DyFK model has an electron skin depth of λ_e = 5.4 km from the top of the flux tube to about 20,000 km before it drops gradually to reach zero about the foot print of the flux tube. This λ_e value is very comparable to the perpendicular wave length $\lambda_\perp$, which is the condition for Alfvén waves to propagate in the inertial regime. The parallel electric field is in the inertial regime also. This situation leads to a constant increase in the magnitude of the parallel electric field. The Alfvénic $E_{||}$ is in opposite phase with the gradient of the scalar potential (see equation 1.1). Our flux tube does not extend to the transition region (from kinetic to inertia).

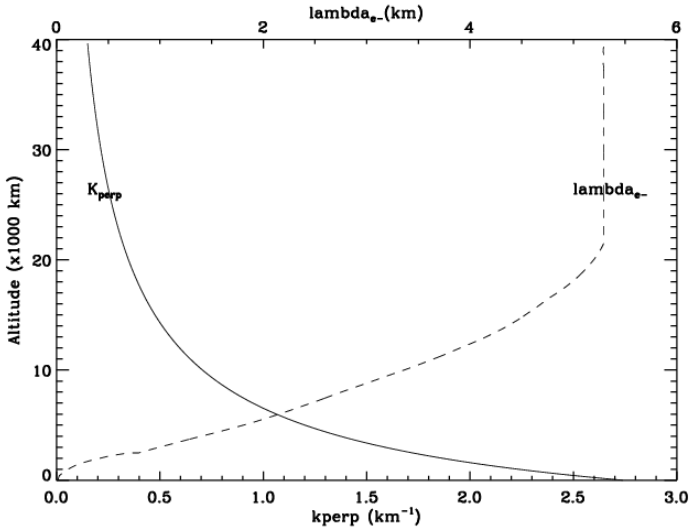

(a)

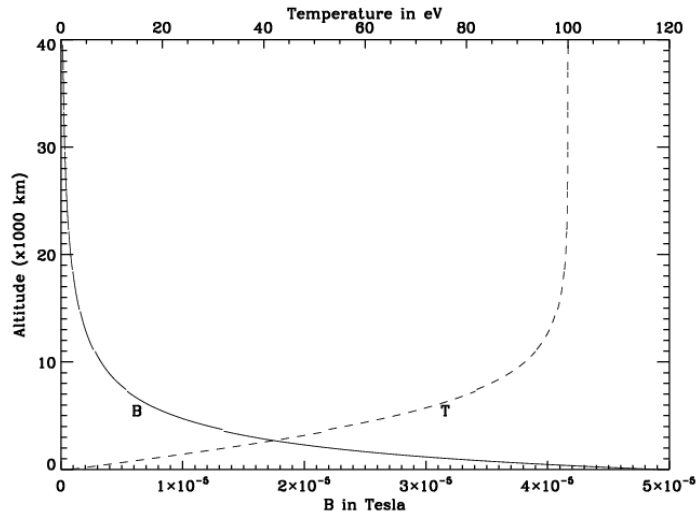

(b)

Figure 5.2 (a) The $k_{\perp}$ profile with the electron skin depth (λ_e) profile. (b) The B◦ (background magnetic field) and plasma temperature (T) profiles.

Figure 5.2a shows the decrease in $k_\perp$ (perpendicular wave number) values going downward the flux tube along with λ_e (the electron skin depth) decrease profile. Figure 5.2b shows the change in temperature and ambient B field along the flux tube, where the temperature, as mentioned before, started at 2 eV and gradually reach 100 eV at the top of the flux tube.

Different factors such as the local plasma density, temperature and perturbation properties of initialization of the Alfvénic wave would determine the magnitude of the produced parallel electric field (equation 1.1). We allow the simulated Alfvén wave to evolve in time so that the Alfvénic parallel electric field has its maximum amplitude $E_{||}$ ~ 0.27 mVm^{-1} at about 25,000 km altitude. The parallel electric field gradually dissipated downward along the field line encountering higher plasma densities and smaller skin depth in the ionosphere region. The behavior of the internal $E_{||}$ is that its magnitude starts to increase right after initialization. The increase of $E_{||}$ is associated with the increasing Alfvén wave speed. Later in the lower dense ionosphere region; the $E_{||}$ starts to decrease with the sharp drop of V_A (results shown in the next section). The magnitude of $E_{||}$ is a significant factor for accelerating any electrons trapped by the wave potential. However, for the simulation results to be physical, these accelerated electrons energy fluxes must be less than the Alfvén wave energy (Poynting flux $\vec{S}$) where $\vec{S} = \vec{B}_\perp \times \vec{E}_\perp$.

To calculate Poynting flux we need to have $E_\perp$ and $B_\perp$ magnitudes. The perpendicular electric and magnetic fields are calculated by using the following equations where Fourier transformation was involved.

$$E_\perp = -(\nabla \phi) = k_\perp \phi \qquad (5.1)$$

$$B_\perp = \nabla \times A = k_\perp A \qquad (5.2)$$

Based on the last two equations, the Poynting flux magnitude is highly dependent on the wave scalar potential and vector potential. The scalar potential behavior is explained by the formula (3.15). Calculating ϕ will provide the means for the behavior of Poynting flux magnitude. Based on equation 3.15 many factors play a role of determining ϕ such as the zero order of ion densities and the intensity of the electron perturbation. Another factor that plays a significant role in determining the wave potential initial value and consequently the wave energy Poynting flux is the phase sign of the initial perturbation. The phase sign (given the initial DyFK density profile) has to be positive. Based on separate study, it is been found that a negative perturbation creates different wave, in addition to a different wave potential and eventually different Poynting flux. The negative initial density perturbation generates an Alfvén waves with much smaller Poynting flux S. Table 5.1 shows the effects on the potential ϕ_0 in simulation results for the same initial DyFK density profile, but with various magnitudes and signs of the initial electron perturbation density. Table 5.1 we also show the effect of the location of the pulse for the same sample on ϕ_0 when we launch an Alfvén wave at different altitudes.

Table 5.1 The maximum wave potential with the change of the initial pulse location and magnitude.

Pulse Magnitude (cm^{-3})	+ 0.5	- 0.5	+1	-1
ϕ_0 (V)	273	42.3	547	84.6
Pulse Location of (80% of the flux tube)	4 R_E	5 R_E	7 R_E	–
ϕ_0 (V)	143	254	273	–

We conclude that the higher electron density perturbation that carries a positive sign at the top of the flux tube higher ϕ_0 magnitude in the lower ionosphere. Also, as expected if the perturbation starts from higher altitudes ϕ_0 will have longer time and distance over which to grow. In addition to the previous simulation study, we performed a different study to understand the effect of the density gradient in the ionosphere region on the ϕ_0 magnitude. We handled 4 different density profiles each had 1 H^+ ion density above 20,000 km altitude. In all DyF density profiles samples an Alfvén wave was launched with the same initial perturbation pulse = 0.5 cm^{-3}. The density gradient was presented by the density difference between two arbitrary altitudes n_2 at 8000 km and n_1 at 3000 km, $\nabla n = \frac{n_1 - n_2}{\Delta L}$ ΔL is the distance between the two measured points. $\bar{n}$ is the average density of the two points at 5500 km altitude. Then we calculated the maximum wave potential reached ϕ_0 which was at ~ 600 km altitude. Figure 5.3 presents the relationship between $\frac{\nabla n}{\bar{n}}$ and ϕ_0. As seen in this Figure, the increase in ϕ_0 values with the decrease in ∇n values or smaller density gradients or shallower density profile slopes. We conclude that density profiles with stronger slopes tend to allow Alfvén waves to build higher potentials. Also we found that the increase in the background H^+ ion density at high altitudes (above 20,000 km altitude) for the same samples that extend to $7R_E$, the Alfvén waves tend to have higher ϕ_0 values at the lower ionosphere region as shown in table 5.2.

Table 5.2 The maximum wave potential with the change of the background H^+ ion density.

# of H^+ ions Above 20,000 km altitude	1	2	10
ϕ_0 (v)	273	342	433

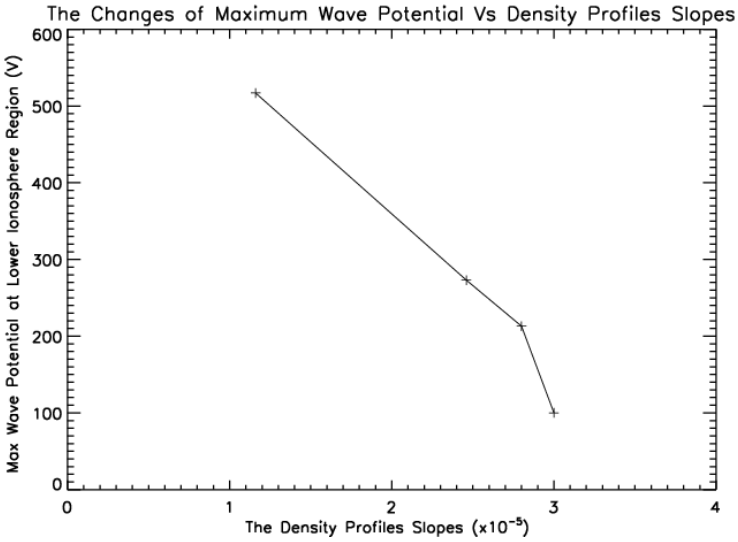

Figure 5.3 The Changes of ϕ_0 values at the lower ionosphere region as the slopes of a 4 different density profiles changes.

Now continuing with the original DyFK model initial density profile where O^+ densities decrease substantially reaching 5000 km altitude, while H^+ ions and electrons maintain density up to the top of the flux tube. In this case the H^+ and e^- densities at higher altitudes would be a major player in determining the magnitude of ϕ and its gradient. Slightly modifying H^+ densities above 20,000 km was performed to meet and maintain 1 cm^{-3} above 25,000 km in order to generate reasonable Poynting flux values at the ionosphere region. The above DyFK density profile had electron inertia dominant effect region for the Gyro-Fluid Alfvén wave where the wave carried Poynting energy flux with maximum magnitude at about 600 km altitude $\vec{S}$ = 2.7732288 erg cm^{-1} s^{-1} . However the $\vec{S}$ =1.8 erg cm^{-1} s^{-1} at about 800 km altitude where perpendicular electric field perturbation $E_\perp$ = 46 mV m^{-1} and perpendicular magnetic field perturbation $B_\perp$ = 47 nT as seen in Figures 5.4 (a), (b) and Figure 5.5. This energy will be partially transferred to the field line electrons for heating and acceleration.

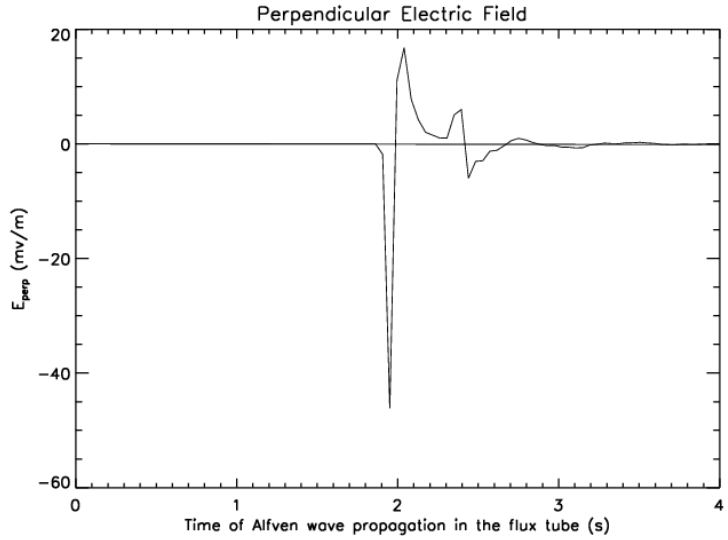

(a)

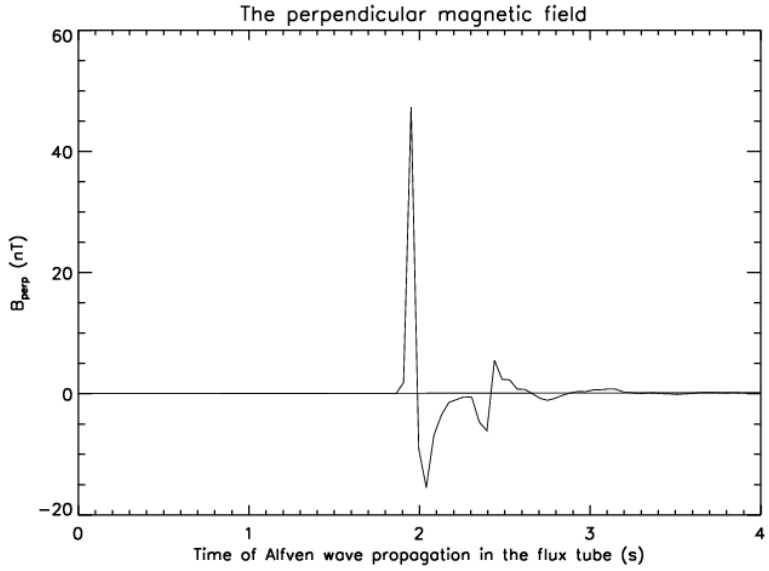

(b)

Figure 5.4 (a) The magnitude of $E_{\perp}$ as it reached 800 km altitude during Alfvén wave propagation down ward along the field line. (b) The magnitude of $B_{\perp}$ at 800 km altitude as Alfvén wave propagated down ward along the field line.

The purpose of calculating the Poynting flux magnitude at this altitude is to understand the role of the Alfvénic electrons precipitating downward on the ionospheric plasma transport. The test particle method used to study the kinetic evolution of these electrons. Calculations of the accelerated electrons base moments of characteristic energy and energy fluxes at the top side ionospheric *F* region (~ 800 km altitude) is performed to determine the evolution of upward ion flows in the ionosphere-magnetosphere coupling region. In order for the simulation results to be physically acceptable, the wave Poynting flux magnitude has to be much higher than the accelerated electrons energy flux. The calculated base moments of accelerated electrons, are used as inputs for the DyFK model to generate the developed density profile influenced by of precipitating energetic electrons.

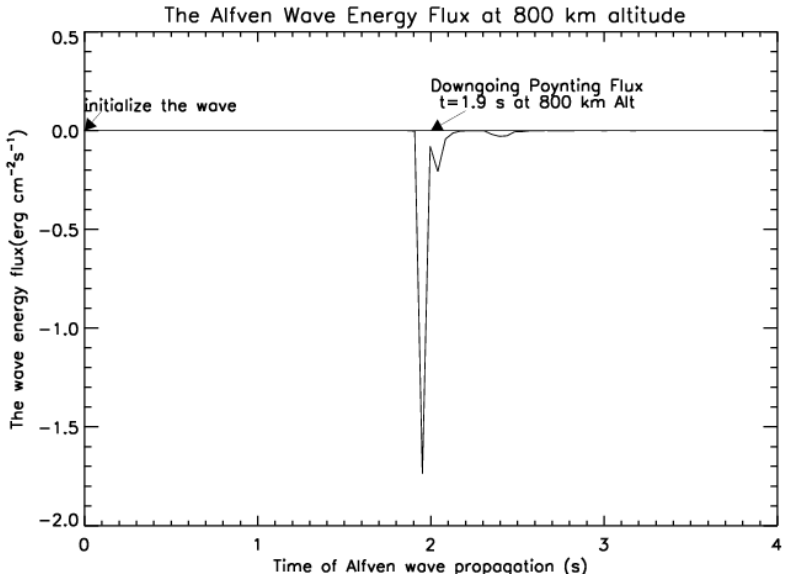

Figure 5.5 The magnitude of down ward $\vec{S}$ at 800 km altitude as Alfvén wave propagated downward.

5.2.3 Magnetosheath Electrons Kinetic Response to Alfvénic $E_{||}$

To track the magnetosheath electrons response to $E_{||}$ that was generated by the Gyro-Fluid Alfvén wave, we employ the test particle code. We generated different flux tubes with different test particles temperatures. The goal is to track the responses of different accelerated electron populations that each has certain temperature.

Based on the given initial conditions presented earlier, a simulated Alfvén wave was launched and allowed to propagate downward along the flux tube. A parallel electric field was formed with a magnitude of $E_{||}$ ~ 0.27 mVm^{-1} at about 10,000 km altitude in the acceleration region. This simulated $E_{||}$ is comparable to FAST data [*Stasiewicz et al.,* 2000]. Given the properties of the simulated Alfvén wave and the produced parallel electric field, the test particle code simulated 5 different flux tubes with the following electrons temperatures: 10, 20, 30, 40 and 50 eV to represent wide range of magnetosheath precipitating electrons. We track the kinetic electron distributions response of all the simulated electrons and their phase speed distributions to the generated parallel electric field.

As mentioned before, the initial electron phase speed distribution function is Maxwellian in all simulated flux tubes. Each flux tube is filled with 350,000 test particles (electrons). After the particles reach the steady sate in each of the flux tubes, the Gyro-Fluid simulated Alfvénic $E_{||}$ was introduced into the particle simulation.

In each of the flux tubes, the initial magnitude of parallel electric field $E_{||}$ increased (a response to DyFK density structure) with increasing the Alfvén wave speed through time until it reached dense plasma region (below the wave phase speed peak), where $E_{||}$ started to diminish very quickly. The propagation of the simulated parallel electric field modified the electron parallel and perpendicular phase speed distributions. The strongest changes were to be located in the acceleration region.

Next we explore the response of test particles (precipitating electrons) at different temperatures to the same Gyro-Fluid initialized Alfvén wave and it's produced parallel electric field $E_{||}$. Then we calculate the accelerated electrons energies and their energy fluxes at 800 km in altitude, which are used later as input parameters in DyFK model to generate the second (developed) density profile.

5.2.3.1 The Kinetic Response of 10 eV Electron Temperature.

Based on the initial conditions we have applied in the Gyro-Fluid model, the simulated Alfvén wave that propagated through the DyFK density profile and had maximum $E_{||}$=0.27 mV/m was not able to trap the 10 eV electrons populations while propagating down toward the ionosphere. That was because the Alfvén wave with its criteria was too fast to pass through the 10 eV electrons without significant effect. The 10 eV electron temperature allowed to reach a velocity V_{te}=1.8 X 10^3 km/s << V_A as the wave passes. The wave was able to create a bump as it traveled down ward along this field line where the electron Maxwellian distribution was not significantly modified, and the electrons were not substantially accelerated.

5.2.3.2 The Kinetic Response of 20 eV Electron Temperature.

The electrons of 20 eV might responded differently, they can reach a velocity V_{te}=2.6 X 10^3 km/s. The Alfvén wave was able to trap and accelerate this population. The parallel electric field at the top of the flux tube started to drive and accelerate the electrons as the wave passed through. A few particles trapped by the wave gained energy and accelerated ahead of the wave. These electrons resonated with the wave and gained sufficient energies to resemble a burst event. These burst electrons showed an increase in the parallel velocity to about 17x10^3 km s^{-1} (at 4.5 R_E) which is more than twice than the local Alfvén speed V_A ~ 8 km x10^3 s^{-1}. During the wave propagation, at about 27,000 km altitude, the group of burst electrons that

were moving downward suddenly started to decrease its speed. More downward accelerated electrons in the burst bulk followed where the total group (bulk) of these accelerated electrons began to rotate in the phase space and gradually the burst electrons separated from the main stream at about 20,000 km altitude. This separated bulk of electrons continued rotating at higher speeds while going down toward the ionosphere. Their speed reached about 33 $x10^3$ km s^{-1} at about 3000 km altitude. Figure 5.6 shows panels of six snap shots of this phenomenon where it presents the evolution of test particles of the 20 eV electrons with the propagating parallel electric field. The Figure shows a series of advanced position and parallel velocities of the accelerated electrons at time 0.495, 0.814, 1.359, 1.450, 1.586 and 1.677 s. The Alfvén phase speed represented with thin line and the parallel electric field represented with the bold line, both obtained from the Gyro-Fluid code.

Calculating the accelerated electrons characteristic energy (ECE) and there energy flux (EEF) at about 800 km, the results showed that ECE= 40.6 eV, and EEF = 0.07 erg cm^{-1} s^{-1}(see Figure 5.7). These two parameters will be used as inputs for DyFK model to generate the next density profile.

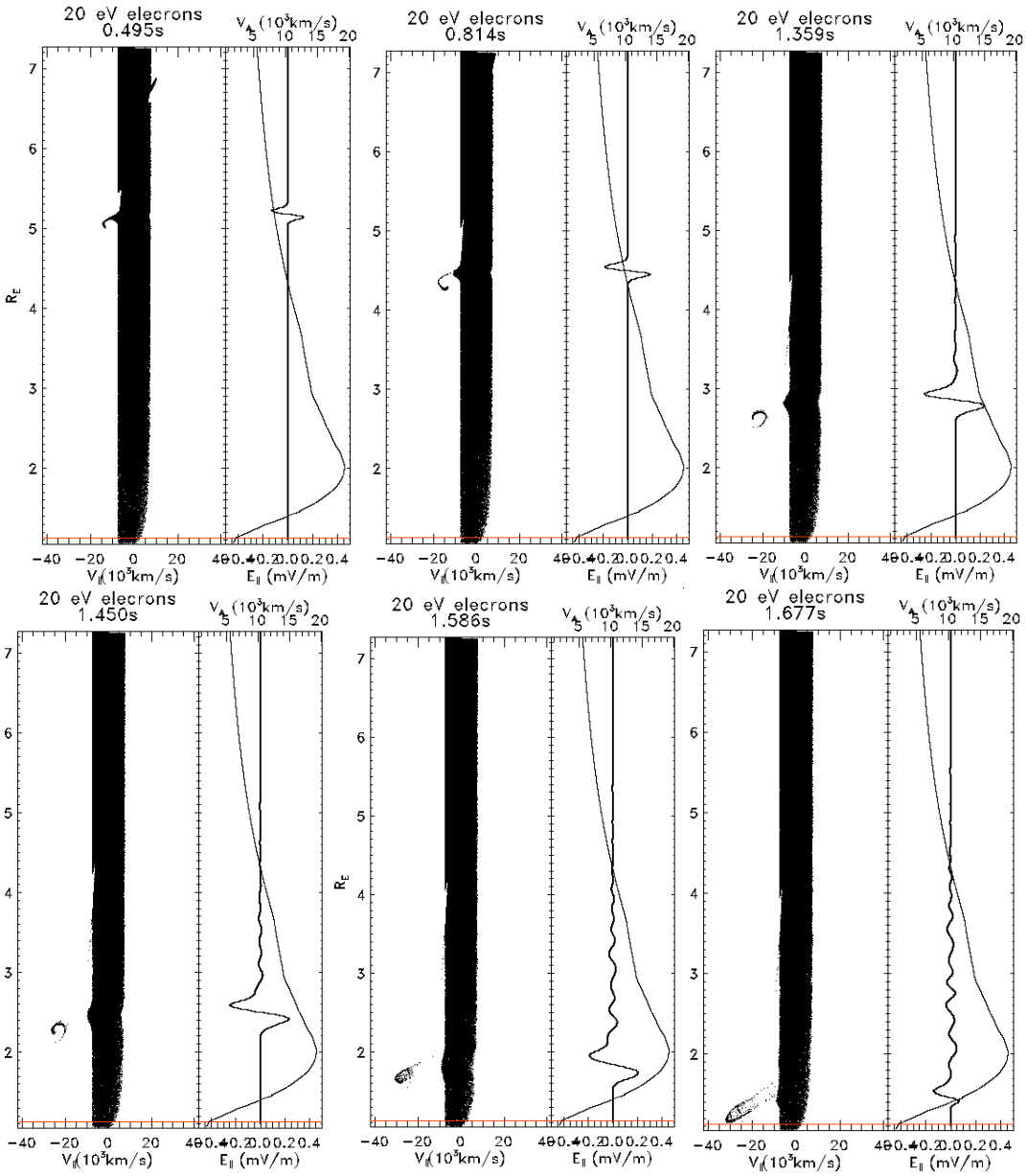

Figure 5.6 Six snap shots of the development of Alfvénic parallel electric field and parallel velocity of 20 eV electrons as time pass. The second panel shows the clear formation of swirling electrons in the phase space which continue rotating while going downward.

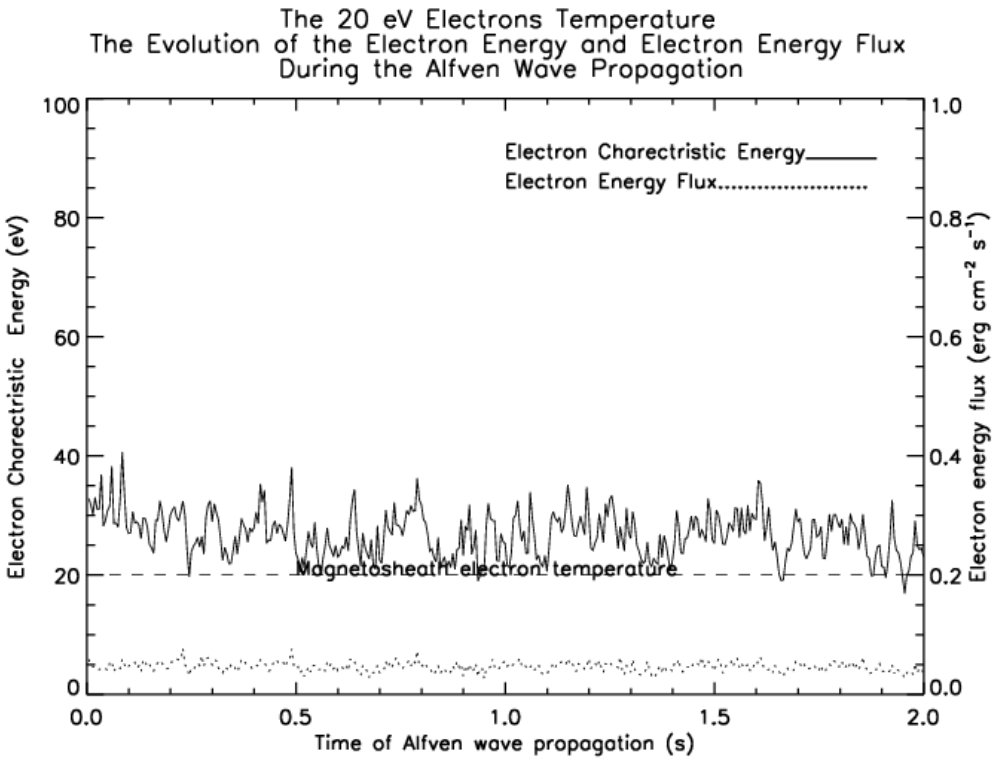

Figure 5.7 The change of electrons energy and the electron energy flux/energy flux for 20 eV electrons during the Alfvén wave propagation along the field line.

5.2.3.3 The Kinetic Response of 30 eV Electron Temperature

Following the propagation of the same initialized Gyro-Fluid Alfvén wave through test particles of 30eV reach a V_{te}=3.2 km x10^3 s^{-1}; this group experienced acceleration and also heating/burst signature. Similar to 20 eV electrons behavior, the accelerated electrons from the 30 eV temperatures, rotated in the phase speed space. However, in this group the wave was able to trap and carry more electrons than the 20 eV electrons. The rotation of highest speed electrons started about 25,000 km with more electrons swirling and then separating from the main stream and that was below 12,000 km altitude. The difference between the 30 eV

electrons and the 20 eV electrons behavior manifested by a bigger bulk of electrons in the 30 eV group than the 20 eV electrons, besides the location of the burst electrons and the total separation was much lower in the 30 eV group. However, in this 30 eV group, and as the wave continue propagation, another group of electrons at about 6000 km altitude experienced a burst event joining the original separated bulk. The highest speed the burst electrons reached was also about 34 $x10^3$ km s^{-1}. Figure 5.8 shows 6 snapshots of the burst/swirling electrons in the phase speed space describing the event as the wave and its parallel electric field propagating downward along the field line.

The electron characteristic energy (ECE) was calculated at about 800 km ECE= 63.3 eV, and electron energy flux EEF = 0.13 erg cm^{-1} s^{-1} (see figure 5.9). Also, these parameters are used later on as inputs in DyFK model to generate a new density profile.

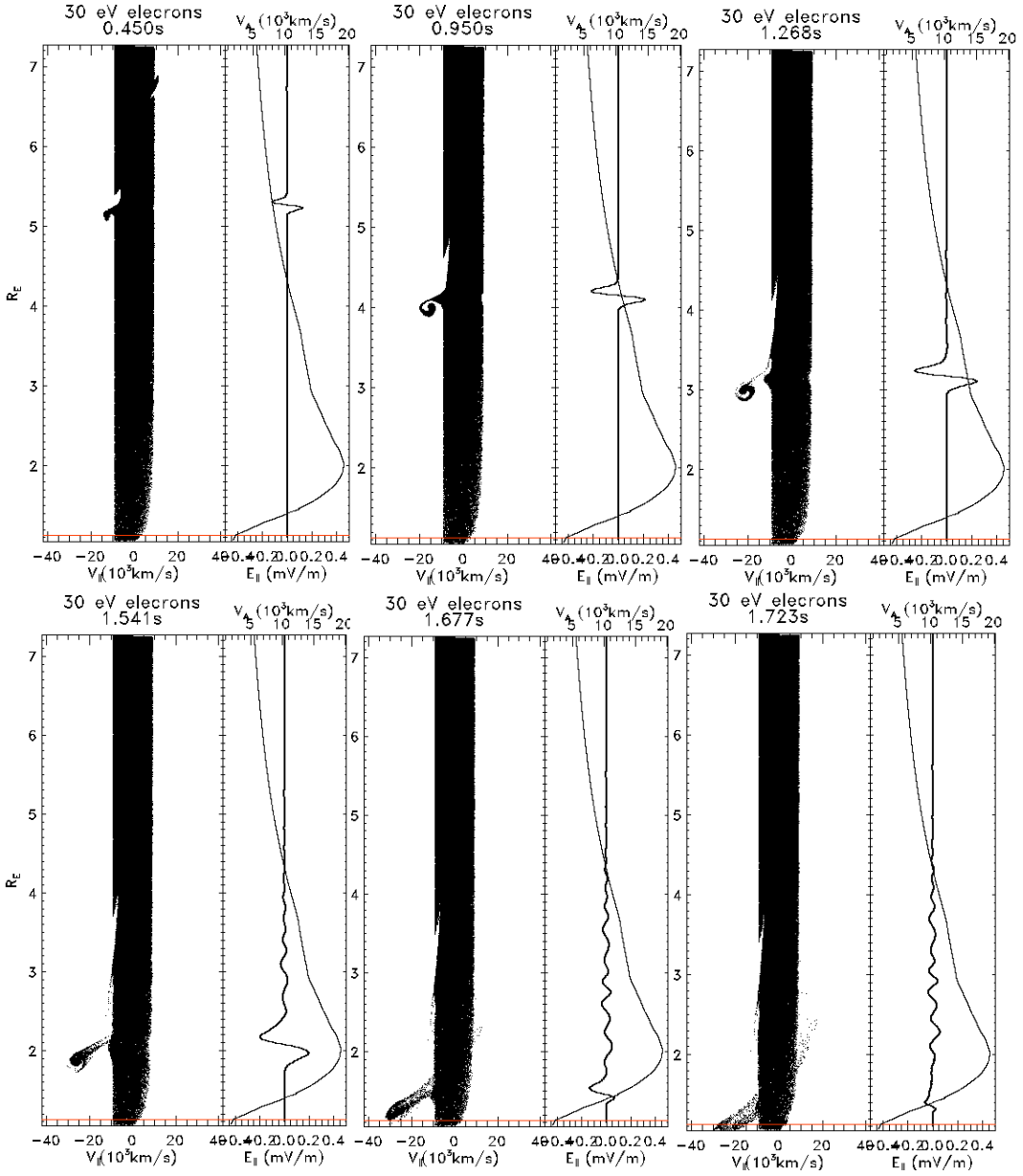

Figure 5.8 Six snap shots of development of advanced parallel electric field and parallel 30 eV electrons as time pass. The swirling electrons in the phase space continue rotating while going downward.

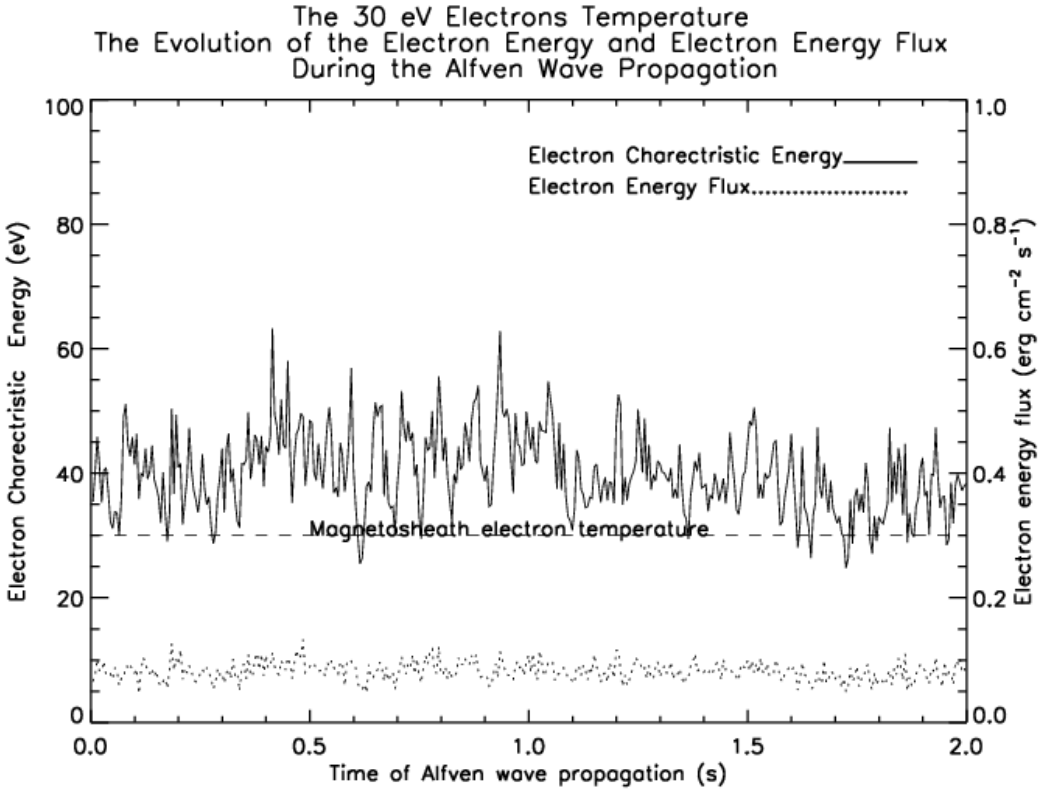

Figure 5.9 change of electrons energy and the electron energy flux/energy flux for 30 eV electrons during the Alfvén wave propagation along the field line at 800 km altitude.

5.2.3.4 The Kinetic Response of 40 eV Electron Temperature.

To track the response of electrons of 40 eV (V_{te}= 3.8 km x10^3 s^{-1}), the $E_{\|}$ that generated by the Gyro-Fluid Alfvén wave, the test particle code showed that as the wave propagates downward, the electrons were trapped inside the wave with many more electrons (compared to the 30 eV group), and these electrons gained energy from the wave. The electrons with the highest energies traveled in front of the wave. Some of the accelerated electrons generated the burst signature. The outer edge electrons of the burst group started to rotate in phase speed space. However, as the wave was moving downward, electrons

continued to accelerate from the original flux tube and join the bulk of burst electrons. The highest parallel speed reached was about 35 x10^3 km s^{-1}. Figure 5.10 shows 3 snapshots of the burst electrons in the phase speed space describing the event as the wave and its parallel electric field propagating downward along the field line.

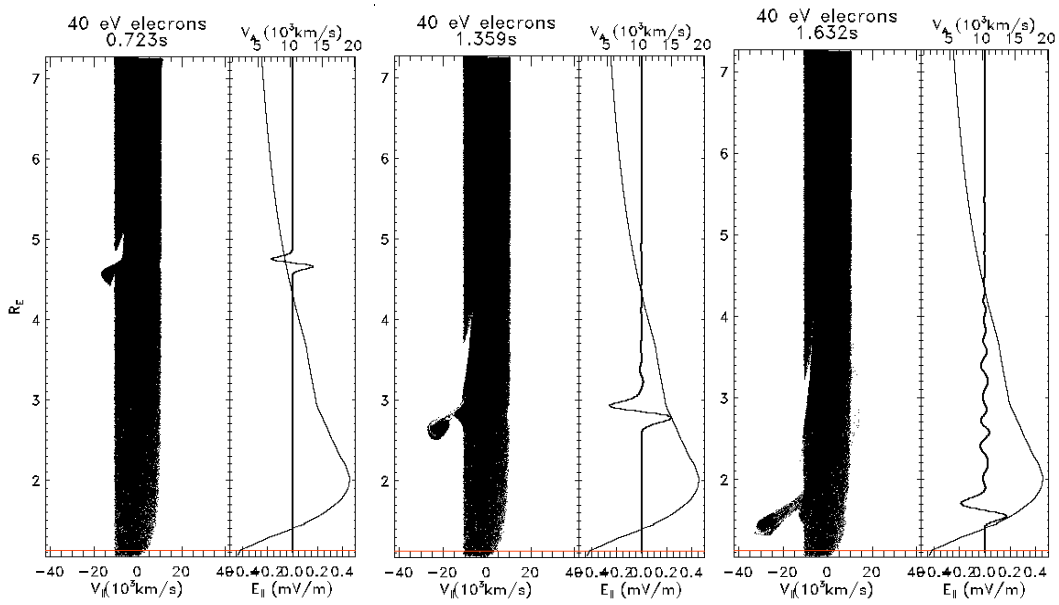

Figure 5.10 Three snap shots of development of advanced parallel electric field and parallel 40 eV electrons as time pass. The swirling electrons in the phase space continue rotating while going downward.

The downward accelerated electrons may enhance the top side ionosphere *F* region production. To investigate the role of those precipitating electrons on the existing plasma density structure, we chose the 40 eV electron group for further simulation study.

As the 40 eV electrons accelerated, they formed a burst signature. In Figure 5.10 the development of this event is shown in the phase space. We show eight snap shots of the electrons distribution function history at the top side of the ionosphere ~800 km altitude. The electrons phase velocities and their evolution was recorded during the 1.95 seconds of Alfvén

wave propagation. The formation of conics and multiple shells in velocity phase space indicates the evolution of the electrons acceleration. As seen in this Figure 5.11 the distribution started as a Maxwellian, then as the wave passed through and accelerated the electrons, the accelerated burst electrons formed a shell (red color). The internal electrons (cold) gained more speed/energies and move together in larger negative $V_{\|}$ in phase space.

The base moments of characteristic energy and energy fluxes at the top side ionospheric F region (~ 800 km altitude) were obtained from the test particle code as inputs for the DyFK ionospheric plasma transport simulation. The electron characteristic energy (ECE) was 104.38 eV, and electron energy flux was 0.38 erg cm^{-1} s^{-1}. The electron's characteristic energy and energy flux are displayed in Figure 5.12 during the time of Alfvén wave propagation.

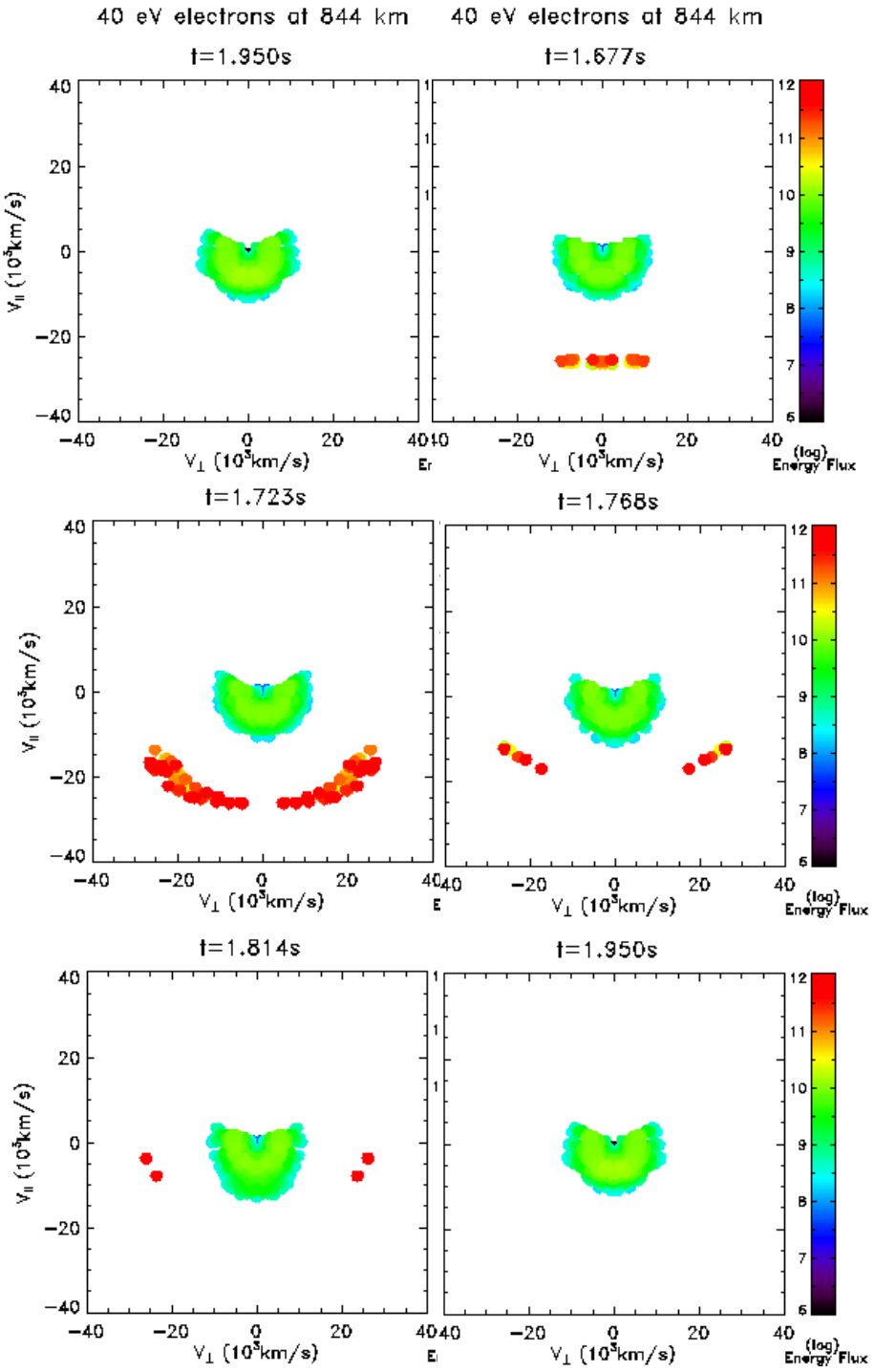

Figure 5.11 Eight snap shots of the phase space distribution 40 eV magnetosheath electrons during the time of Alfvén wave propagation at 800 km altitude.

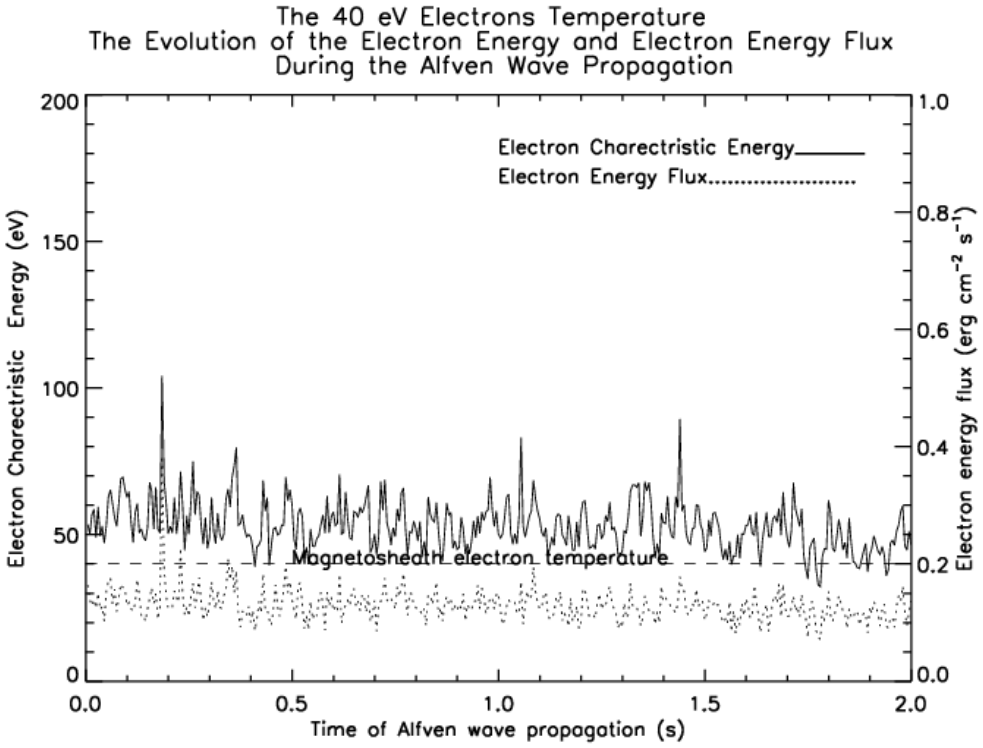

Figure 5.12 The change of electrons energy and the electron energy flux/energy flux for 40 eV electrons during the Alfvén wave propagation along the field line at 800 km altitude.

5.2.3.5 The Kinetic Response of ≥50 eV Electron Temperature.

When the electrons the 50 eV temperatures reach V_{te} = 4.2 km x10^3 s^{-1} , the parallel electric field had larger impact on these electrons; they became strongly accelerated and energized. The wave was able to trap and carry a larger number of electrons than the previous groups. However, the 50 eV group did not experience rotation. As the wave propagated, electrons were continuously accelerated. The highest speed electrons reached was about 35 x10^3 km s^{-1}. Calculating the electron characteristic energy (ECE) calculated at about 800 km ECE= 278 eV, and electron energy flux EEF = 1 erg cm^{-1} s^{-1}. The electron energy flux reached

a comparable value with the wave energy flux S= 1.8 erg cm^{-1} s^{-1}. Because the value of electron energy flux that was reached exceeded 50% of Poynting flux, the simulation is not self contestant.

5.3 Ionosphere Response to Energized Alfvénic Electrons

To describe the interaction of accelerated Alfvénic electrons with the ionosphere plasma and consequently the ionospheric plasma transport along the magnetic flux tube; we perform sequental simulations involving the DyFK model, the Gyro-Fluid simulation and the test particle method in iteration. The DyFK model forms the initial density profile through which the Gyro-Fluid model simulates a propagating Alfvén wave. The propagating Alfvén wave could sustain a parallel electric field that drives magnetosheath electrons downward toward where they impact the ionosphere. To investigate the interaction of the Alfvénic precipitating electrons on the existing DyFK plasma density structure, we use the test particle method to calculate their base moments of characteristic energy and energy fluxes at the top side ionospheric *F* region (~ 800 km altitude). In the aurora region, the precipitating electron energies and energy fluxes including the auroral electric field wave spectral density are the main physical processes that influence the plasma transport. The heavy ion outflow is controlled by these processes. Alfvén waves provide one of the sources for such process.

Soft electron precipitation enhances F region plasma production and electrons temperature. Transverse wave heating enhances the ion out flow and continuously modifies the aurora ionosphere-magnetosphere density structures. In our simulation, we include the auroral processes caused by the propagation of Alfvén wave (soft electrons precipitation), which modifies DyFK densities. The initial DyFK density profile will evolve to a new plasma structure for every propagated Alfvén wave. The iteration between the models shows the consequent effects on the properties of the next propagating Alfvén wave due to the injection of new particles into the background density profile. It should be noted that, the coupling between the

three models is not strictly self consistent. Below is a diagram shows the sequent iteration between the simulation models.

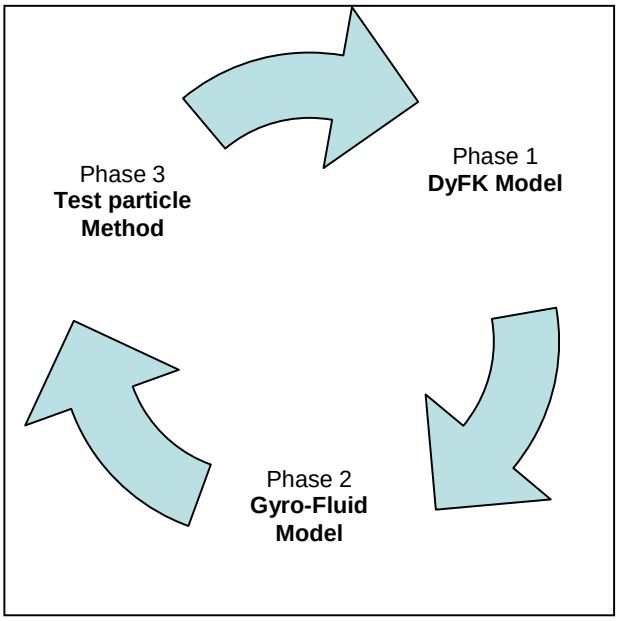

Figure 5.13 Diagram show the relation between the three models as they sequential iteration.In phase 1, DyFK model generates Generates M-I density profile. Phase 2, The Gyro-Fluid model lunches propagating Alfvén wave and generates $E_{||}$. Phase 3, the Test Particle code tracks the evolving distribution of electrons phase speed.

Next, we display simulation results of our models. The electrons that are accelerated by Alfvén waves are going downward toward the ionosphere. These energetic electrons are precipitating in fluxes that enhance the top side ionosphere *F* region production. For the DyFK simulation, the maximum electron energy and electron energy flux during the Alfvén wave total time propagation are used as inputs. The purpose of this step is to generate a density structure in response to the propagation of a group of simulated Alfvénic parallel electric fields. In section 4.4 the Alfvén wave was initiated with an electron density perturbation of 0.5 cm^{-3}. The initial conditions that generated the initial Alfvén wave lead to a parallel electric field with a maximum

value of 0.3 mVm^{-1} at ~ 10,000 km altitude. The initial Alfvén wave carried energy of 1.8 erg cm^{-2} s^{-1} at 800 km altitude. The simulated parallel electric field accelerated electrons of 20 eV, 30 eV , 40 eV and higher temperatures. The test particle method was able to show the field-aligned electron bursts of these groups of electrons. To make our results meaningful, we used the cases were the electron energy flux does not exceed the 50% of the Alfvén wave energy. The cases applied to this condition are only the 20 eV and 30 eV and 40 eV electron temperature groups. The interaction with the Alfvén wave caused the field-aligned electrons to gain energy reaching a maximum energy of ECE=40.6 eV, EEF=0.07 erg cm^{-2} s^{-1}, for 20 eV group, ECE=63.3 eV and EFE= 0.13 erg cm^{-2} s^{-1} for 30 eV group and ECE= 104 eV and EFE=0.38 erg cm^{-2} s^{-1} for 40 eV group at ~ 800 km altitude.

The calculated values of Alfvénic precipitating electrons energies and energy fluxes at the ionosphere along with wave-driven transverse ion heating at 0.3×10^{-6} V^2 m^{-2} Hz^{-1} are inputs to the DyFK model. The DyFK simulation runs for 240 second (10 steps) or for 4:00 minutes, the choice of this time span was based on the assumption that the DyFK simulated density structure would show a considerable change in the ions densities along the flux tube for such time period. The DyFK model simulates the ionospheric-magnetosphere plasma that would consequently affect the transport of the O^+ bulk parameter evolution. Increasing the mass density will affect the phase speed of the next propagating Alfvén wave [*Su et al.,* 2004].

5.4 Simulation Results of Continuous Alfvén Wave Propagation Through Evolving Plasma Density

To follow the effects of continuous changes in the plasma profile on Alfvén wave properties; we perform a series of simulation steps. After simulating the density perturbation used in the Alfvén wave in Gyro-Fluid code, a simulated Alfvén wave was allowed to propagate and generate parallel electric field. The electric field then accelerated electrons downward toward the ionosphere with wide range of energies. We gathered the simulation results obtained from the test particle method that had different electrons temperatures. Next we display the simulation results of the 3 models iteration for the 20 eV, 30eV and the 40 eV electron temperatures. However, we are exploring the 20 eV electrons responses first then the 30 eV and finally the 40 eV electrons.

5.4.1 The 20 eV Electron Temperature Simulation Results

Following the same steps and analysis with this group of test particles, also with 4 iterations of Alfvén propagation were applied. The sequential effects of continuous changes in the plasma profile and on Alfvén wave profiles are displayed in table 5.3. The data presented in this table show the increase in the O^+ ion densities through the transition time. The Alfvén phase speed became slower and its plateau flatter; the reduction rate is close to the two previous groups. The $E_{||}$ fluctuated through time but not significantly. The electron energies and their fluxes increased from the initial values (due to the increase in $E_{||}$) then kept steady along the transition time (due to steady $E_{||}$ amplitudes). The EEF values were much less than 50% than the wave Poynting flux as time passed.

Table 5.3 The simulation results of 20 eV electrons.

Iteration #	1	2	3	4
Transition time (sec)	1.9	2	2.6	3.5
Max V_A (x 10^3 km/s)	20.2	18.5	14.26	10.52
O^+ Density (4000 km) cm^{-3}	3.4	13.25	49.23	99.27
Max $E_{\|\|}$ (mV/m)	0.27	0.3	0.29	0.29
ECE (eV)	40	40.62	40.62	40.62
EFE (erg cm^{-2} s^{-1})	0.07	0.074	0.0.73	0.072
S at 800 km (erg cm^{-2} s^{-1})	1.8	0.55	1.15	1.55

5.4.2 The 30 eV Electron Temperature Simulation Results

Following the same steps and analysis with this group of test particles, 4 iterations of Alfvén propagation was applied. As for the sequential effects of continuous changes in the plasma profile and on Alfvén wave profiles, table 5.4 shows the simulation results of DyFK model and Gyro-Fluid along with the test particle method. The changes in the plasma mass densities consequently modified the Alfvénic parallel electric field which is also displayed in the table below. After performing the same series of simulation steps, the changes in the electrons energies and energy fluxes are also both displayed in the table.

Table 5.4 The simulation results of 30 eV electrons.

Iteration #	1	2	3	4
Transition time (sec)	1.9	1.97	3.14	3.5
Max V_A (x 10^3 km/s)	20.2	18.8	11.76	10.32
O^+ Density (4000 km) cm^{-3}	3.4	12.72	52.49	97.8
Max $E_{\|\|}$ (mV/m)	0.27	0.29	0.29	0.27
ECE (eV)	63.27	62.35	66.56	62.27
EFE (erg cm^{-2} s^{-1})	0.13	0.13	0.14	0.12
S at 800 km (erg cm^{-2} s^{-1})	1.8	0.53	1.35	1.35

From table 5.4 we conclude that the O^+ ion densities increased through the transition time, and the maximum Alfvén phase speed declined (as expected). The magnitude of the parallel electric field increased in the second event and kept constant along the transition time. The electron energies at 800 km altitudes were raised higher than the original value (30 eV), but then kept around this values for the rest of the events along with the electron energy fluxes. The values of EEF values were less than 50% than the Poynting flux along the total transition time. The difference between the results of 30 eV temperature and the 40 eV electrons are in the data of precipitating electron energies and their energy fluxes at 800 km altitude. However, this difference did not significantly affect the increase in O^+ ion densities and the associated phase speed results. The reason for this is DyFK model presents the values of soft electron precipitation stream as Maxwellian energy spectrum, with peak of the given value [*Newell et al.,* 1996]. However, electrons with energies less than 100 eV mostly affect the topside ionosphere rate of ionization where the electrons with higher energies penetrate deeper with a weak effect on the surrounding atoms.

5.4.3 The 40 eV Electron Temperature Analyses

The transition time for one iteration of the DyFK simulating density profile, the initialization and propagation of Alfvén wave generated by Gyro-Fluid model and finally the influence of the produced parallel electric field on the magnetosheath electrons applied by the test particle, extended to $T_{transition}$= 242 seconds = 4:02 minutes. The transition time was the product of adding DyFK simulation time (T_{DyFK}=240 (24 x10 steps)) plus the time of Alfvén wave propagating through the test particles (T_{Alfven}=2sec). The Alfvén wave propagation time is determined by its local phase speed velocity and its location. We used the maximum value to calculate the Alfvén propagation time. The calculations of the initial base moments of the accelerated electrons at the ionospheric top region (~800 km altitude) obtained from the test particle method of the 40 eV electrons were as follows; ECE (1) = 104.38 eV, and electron

energy flux EEF (1) = 0.38 erg cm^{-1} s^{-1} where wave Poynting flux S=1.8 erg cm^{-2} s^{-1} and the initial maximum $E_{||}$ =0.27 mV/m. The ECE and EEF values are used as inputs in the DyFK model to produce a second density profile. Then the Gyro-Fluid model initiated a second propagating Alfvén wave through the second generated DyFK density profile with a density perturbation of a single Gaussian pulse of an amplitude A=0.5 cm^{-3} (same as the initial). The wave propagated through the developed DyFK density structure of O^+, H^+ and e^-. The test particle method showed that the 40 eV magnetosheath electrons also experienced heating/acceleration. Again, calculating the electrons energies and their energy fluxes at the top side ionospheric *F* region (~800 km altitude) for this step and then for the next 2 steps as we iterate between the 3 models to produce the sub-sequent density profiles and their associated wave phase speed profiles. The iteration continued 4 times altogether and the results are displayed in table 5.5 as follows.

The maximum value of the parallel electric field experienced some reduction starting from the second round. Figure 5.14 shows the gradual change in ECE and EEF along with Poynting flux during the total transition time at 800 km altitude. From this Figure, the electron energies drop slightly, the electron energy fluxes sustain its initial value. Through the 4 events the difference between the wave Poynting flux and the electron energy fluxes were below 50%.

Table 5.5 The simulation results for 40 eV electron temperature.

Iteration #	1	2	3	4
Transition time (sec)	1.9	2.05	4.	4.7
Max V_A (x 10^3 km/s)	20.2	18.8	11.76	10.32
O^+ Density (4000 km) cm^{-3}	3.4	12.72	52.49	97.8
Max $E_{\|\|}$ (mV/m)	0.27	0.48	0.3	0.29
ECE (eV)	104.38	99	87	78
EFE (erg cm^{-2} s^{-1})	0.38	0.3	0.23	0.2
S at 800 km (erg cm^{-2} s^{-1})	1.8	0.8	1.05	0.52

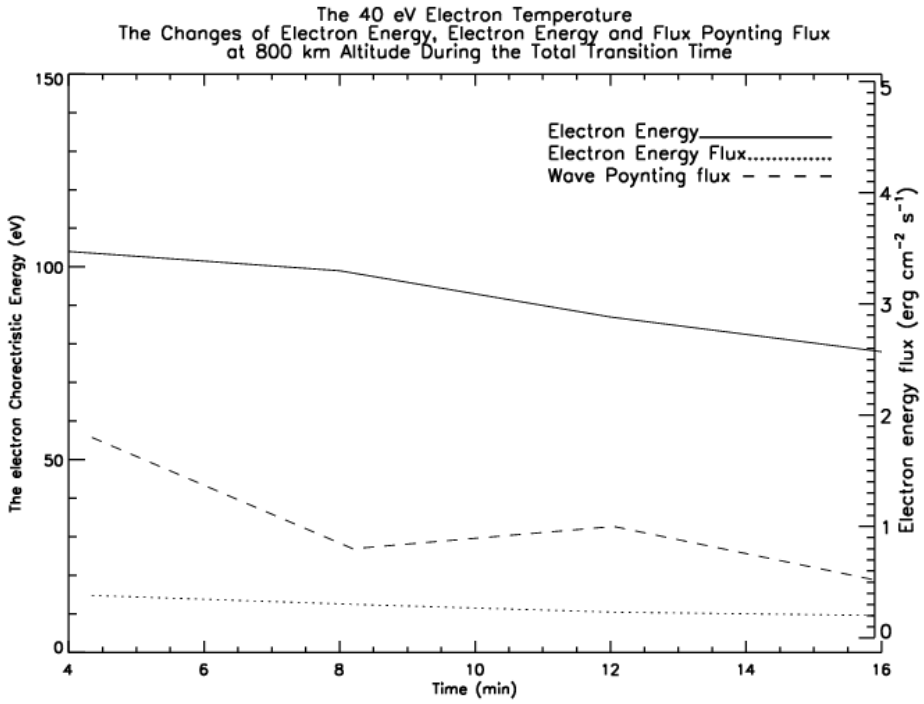

Figure 5.14 The changes of electrons energy and the electron energy flux and wave energy flux of 40 eV electron temperatures through ~ 16 minutes of transition time of 4 iterations of Alfvén wave propagation.

During the following series of propagating Alfvén wave events, the effect of the auroral processes presented by precipitating electrons (due partially to the Alfvén waves) and the transverse wave heating, caused evolution in the background plasma density profiles. That in turn, caused significant changes with the Alfvén wave phase speed profiles.

The ion density enhancement was due to the increase in ionospheric plasma outflow and mass density in M-I coupling region. The plume in O^+ densities expanded upward along the flux tube as shown in Figure 5.15. For comparison, we chose fixed point such as FAST spacecraft altitudes (~ 4000 km) to display the simulated results of O^+ densities; Den(1) = 3.4 cm^{-3} increased to Den(2) = 12.8 cm^{-3} in the second event then Den (3)= 48.92 cm^{-3} in the third event to the fourth Den(4)= 97.5 cm^{-3} . Then plugging the fourth base moments in DyFK to get the last O^+ density profile Den (5)= 135 cm^{-3}.

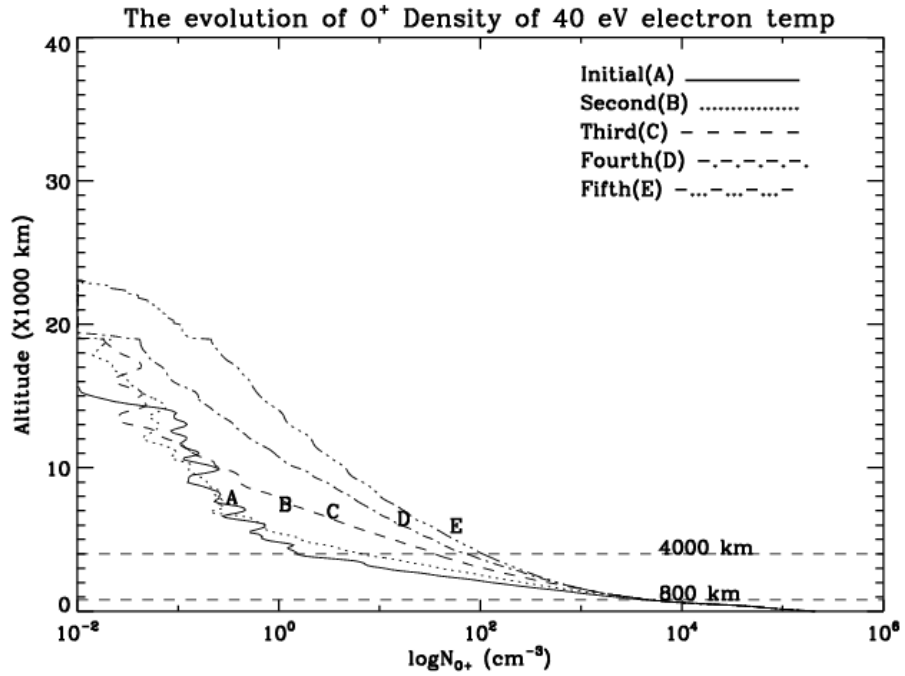

Figure 5.15 The evolving new O^+ ion structure, incorporating precipitating electrons and wave-driven ion heating, where the simulated O^+ ions driven upward to above 4000 km (FAST spacecraft location) after 4 iterations or total transition time ~ 16 min.

On the other hand, the H^+ ion densities showed weak response to the implied conditions and parameters as seen Figure 5.16. The H^+ ions are mainly affected by O^+ ion production in the surrounding environment, but slightly affected by the transverse ion heating (discussed in details in chapter 4). This shows the increase in the plasma mass is mainly due to the increase of the heavy O^+ ion densities.

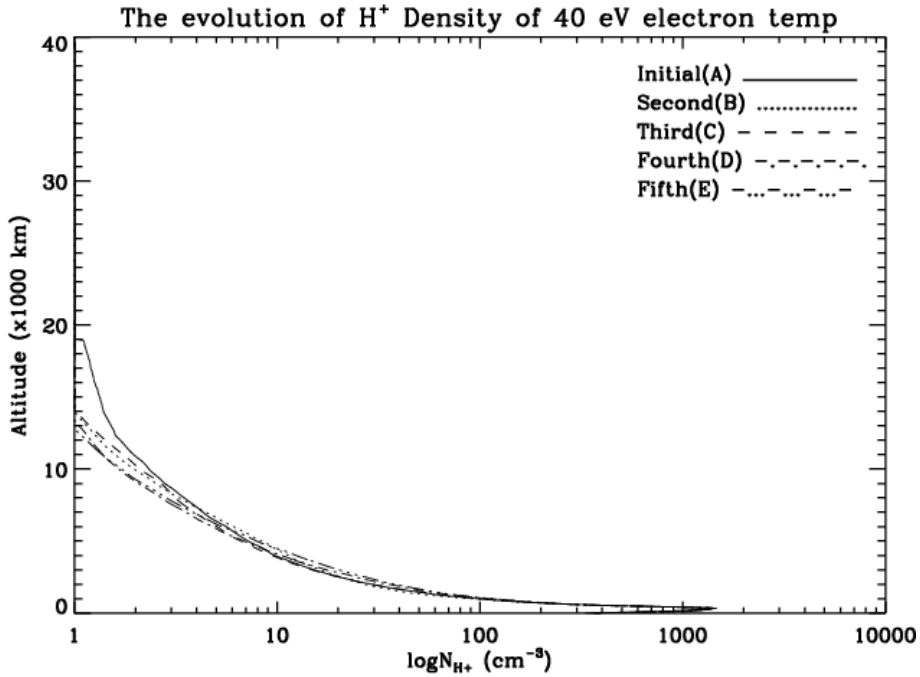

Figure 5.16 The evolving new H^+ ion structure, incorporating precipitating electrons and wave-driven ion heating, where the simulated H^+ ions are not modified significantly above 4000 km (FAST spacecraft location) after 4 iterations or total transition time ~ 16 min.

Alfvén phase speed profiles modifications were manifested by reduction in all its values along the field line through the transition time. This reduction in Alfvén wave speed in the acceleration region is associated with the O^+ ion density enhancement. The local Alfvén phase speed became slower and the profile became flatter. The Alfvén phase speed evolving profiles are shown in Figure 5.17. The peak of Alfvén speed dropped gradually from ~ 20.2 x 10^3 km/s in the initial run to 19.5 x 10^3 km/s then 13.5 x 10^3 km/s in the third run to 10.2 x 10^3 km/s in the fourth and finally (the fifth profile) is 8.5 x 10^3 km/s. The simulation time span corresponded to Alfvén wave propagation during every iteration step were as follows, the initial transit time t (1)= 1.9 sec, increased to t(2)=2.05 sec, extending to t(3)=3 sec, t(4)= 4 sec, finally t(5)= 4.7 sec t(5) is a result of incorporating the values of the fourth base moments in the DyFK model to produce

final density and Alfvén phase profiles). As noted in previous studies [e.g., *Su et al.,* 2004]. Lower Alfvénic speeds can enhance particle acceleration over a larger acceleration region. In the region of flatter phase speed, electrons with V_{te} near V_A maintain more acceleration along the flux tube. Also the parallel electric field maintains its amplitude in this region.

As mentioned, the implication of the extension of the acceleration region in the upward direction is moving the burst event location upward during the transition time. However, the intensity of the electron burst signature started to decrease gradually and the intensity of electron acceleration became slightly weaker at later iterations. Loading the system with heavy ions has significant implications; increasing the O^+ mass widens the acceleration region and reduces the magnitude of $E_{||}$. Otherwise, a larger increase in electrons energies and energy fluxes would exist during the transition time.

To demonstrate the continuous changes in the electron energies at the same fixed point (4000 km) altitude, Figure 5.18 shows snapshots for the same simulation time of the evolving electron phase speed distributions at ~ 4000 km after the Alfvén wave passed by. The plots correspond to the following energies, ECE(a)=83 eV and EEF(a)=0.56 erg $cm^{-2}s^{-1}$, ECE(b)= 84 eV and EEF(b)=0.59 erg $cm^{-2}s^{-1}$, ECE(c)=79 eV and EEF(c)=0.64 erg $cm^{-2}s^{-1}$, finally ECE(d)= 68 eV and EEF(d)=0.53 erg $cm^{-2}s^{-1}$. As seen, from the plots and the calculations, the intensity of electron acceleration increased slightly from (a) to (b) then decrease in (c) and (d) where the acceleration in the last event started later on in time. These changes are due to the changes in $E_{||}$ amplitudes which are again affected by the increase in the O^+ ion densities in the upper altitudes.

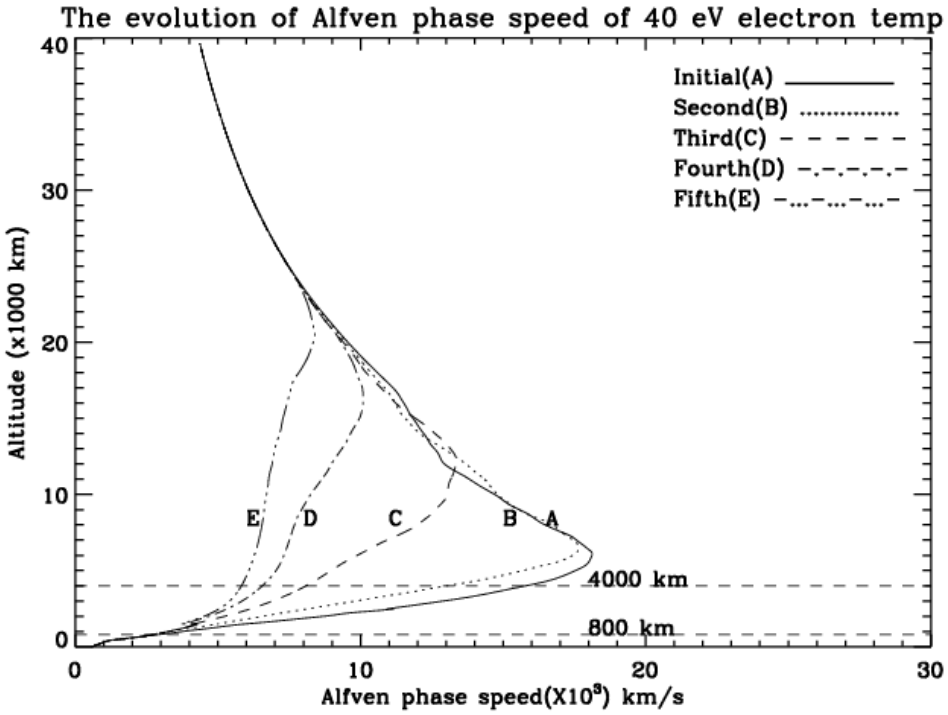

Figure 5.17 The evolution of Alfvén phase speed during the same time, and the change of the electron burst location for each step were the implications of the increase in local mass densities, the location of electron burst was gradually moving upward toward higher altitudes.

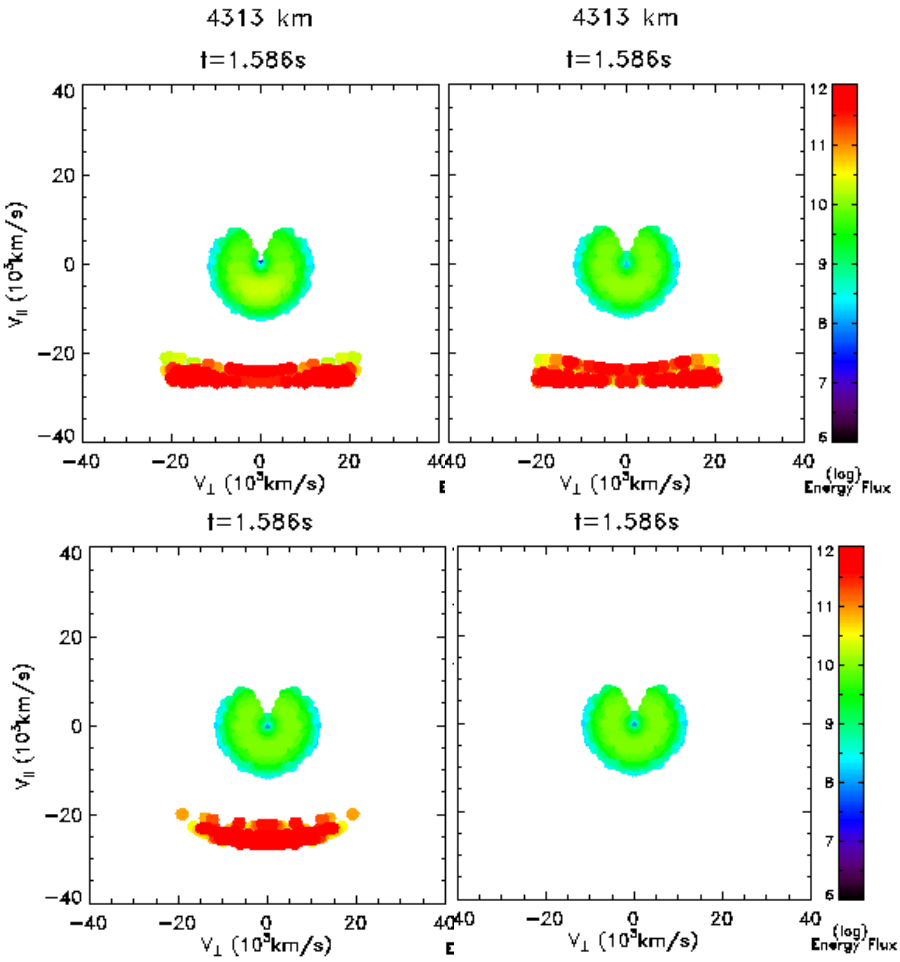

Figure 5.18 Four snapshots of electron distributions at 4000 km as the Alfvén wave passed through this location 4000 km altitude. As the O^+ density increases the $E_{||}$ amplitude decrease to a point where it weakly accelerates electrons even though the Alfvén speeds decreased over the same period of time.

5.5 Simulation Results of 40 eV Electron Temperature With Fixed S=0.2 at 8000 km Altitude

In all previous simulations, we had the same initial density perturbation A=0.5 cm^{-3} to launch Alfvén wave. For further simulation and to explore other regions of wave potentials that would allow for continuous Alfvén wave propagation, the simulation initiated different density perturbation for generating Alfvén wave; the suggestion was to launch the propagating waves with the same wave energy or Poynting flux at some location. The simulation forced the waves during each event to carry Poynting flux S=0.2 erg $cm^{-2}s^{-1}$ at 8000 km altitude. The purpose of this step is to follow the nature of the evolving densities and phase speed profiles including the base moments of the 40 eV test particles.

Such waves are also capable of raising the O^+ densities and consequently decrease the Alfven wave velocities as seen in table 5.6. However, the $E_{||}$ values sharply increased (from the second event) more than the previous cases. The electron energies experienced significant fluctuation also but their fluxes kept steady until the last iteration where it had sudden increase and its value became comparable to the wave energy. In this case, the particle acceleration is not valid (highlighted events). The increase in $E_{||}$ magnitudes increased the electron fluxes to higher intensities. The high wave energy increases the parallel electric field amplitudes despite the increase supply in the surrounding plasma mass.

Table 5.6 The simulation results of 40 eV electrons. The initial condition is S=constant S=0.2 erg cm^{-2} s^{-1} at 8000 km

Event #	1	2	3	4
Transition time (sec)	1.9	2.7	2.06	1.35
Max V_A (x 10^3 km/s)	20.2	13.5	17.75	27.32
O^+ Density (4000 km) cm^{-3}	3.4	15.3	50.16	99.86
Max $E_{\|\|}$ (mV/m)	0.27	0.25	0.39	0.65
ECE (eV)	104.27	179.6	101	252
EFE (erg cm^{-2} s^{-1})	0.38	0.4	0.36	1.6
S at 4000 km (erg cm^{-2} s^{-1})	0.2	0.2	0.2	1.8

5.6 Conclusions

We have presented the simulation results of characteristic properties of Alfvén wave's propagation in different density scenarios. Three coupled models were employed; the DyFK model for the ionospheric plasma transport, the Gyro-Fluid model for launching Alfvén wave propagation and the associated electric field, then the test particle code for tracking the electron acceleration and calculating their base moments. The three models were linked but not self consistently. We investigated the role of the Alfvén phase speed evolution on the field-aligned electron acceleration, where the phase speed evolved through the transition time.

The DyFK model was able to generate a density profile of O^+, H^+ and e^- which successfully reproduced field-aligned electron burst along with the propagation of Gyro-Fluid Alfvén wave. Certain factors played a significant role of generating Alfvén waves that carry energy to field-aligned electrons for acceleration downward to the ionosphere region. The wave potential was controlled by the magnitude and the phase of the initial density perturbation. The phase of the initial perturbation used in this study was positive for the same wave amplitude. A negative perturbation created small Poynting flux S. Also, the slope of the density profile and the number of the background H^+ in the upper altitudes determine the values of the wave energy or Poynting flux along the flux tube. Consequently, these factors control the magnitude of the generated parallel electric field that accelerate electrons and produce the electrons burst signature. The accelerated electrons carry flux and should not exceed the wave energy flux. We conclude that the surrounding density structure controls behavior of the Gyro-Fluid Alfvén wave. Using the test particle method to study the accelerated electron distributions given different electron temperatures, the simulation results showed that for given plasma density, limited groups of magnetosheath electrons would be affected by the generated Alfvén wave. We showed the evolution of field-aligned ionosphere-magnetosphere O^+ densities along with the Alfvén phase speed profiles using test particle results. The development of density structures created conditions of flattened and reduced Alfvén speeds for enhanced electron acceleration.

This property allowed a wider region for electron acceleration. However, the increased mass in the surrounding plasma, reduced $E_{||}$ slightly for the 40 eV electrons, but it sustained its value for 20 and 30 eV electrons. The reduction in $E_{||}$ countered effect the wider acceleration region and the electrons did not gain significant energies during the downward acceleration in this region. However, in the constant initial S case we noticed different behavior of the $E_{||}$, it increased significantly during the transition time which in turn caused eventually higher electron energies and energy fluxes. The high wave energy fluxes generated strong parallel electric field. However, given this situation, the electrons accelerated with high fluxes beyond the capability of our three coupled models to simulate.

At the end, our simulation results showed a successful link between the DyFK, Gyro-Fluid and the test particle models that produced physical results. The most interesting conclusions were that, the continually propagating Alfvén waves in a fixed flux tube caused continuous increase in the O^+ outflow, this lead to constant mass load in the surrounding plasma. The evolution ion density affected the properties of the subsequent Alfvén wave properties with the same initial configuration. The simulation results showed evolution in the Alfvén phase speed. As the O^+ densities increased the Alfvén waves become slower and its profiles became more flat promoting wider region of electron acceleration.

CHAPTER 6

SUMMARY AND FUTURE WORK

The polar cap magnetosphere-ionosphere region is a continuous dynamic and physical process, governed by the constant transformations of energy through waves and particles. The plasma densities in turn significantly fluctuate temporally and spatially, where ion depletion and ion outflow is very common. In the auroral region, the magnetic field lines are the main channels for heavy ion outflows and the ionosphere is considered as major plasma supplier to the magnetosphere system through ion transport processes. Electrostatic and traveling waves are also a significant aspect of this region; Broad-Band Extreme Low-Frequency BBELE waves are a cause of ion resonance/outflow and Alfvén waves which provide the means of transport energies to the surrounding particles.

In this dissertation, we have investigated two different topics and both are related to O^+ ion out flow and O^+ ion density structures at high-latitude ionosphere-magnetosphere region.

6.1 Summary of Results of Simulation of the Formation of O^+ Density Troughs

Using simulations and spacecraft observations in this work, we have explored the processes that controlling the O^+ density levels at ~ 6000 km altitude region. The observations have indicated considerable variability in O^+ densities in the polar cap ionosphere-magnetosphere region. The data reflected fluctuations in O^+ densities from above 10 cm^{-3} to below 0.01 cm^{-3}. The data showed significant declines in O^+ densities over the polar cap referred to as O^+ density troughs. The densities that are lower than 0.01 cm^{-3} are considered troughs [*Zeng et al*., 2004]. We examined four different cases for observation and simulation comparison. They are; August 20 1998, August 02 1998, June 26 1998, and December 02 1997 covering the O^+ trough regions.

The simulation of the ionospheric plasma outflow from the lower ionosphere region to high altitudes presented in this work were obtained with the UT Arlington 1.5-dimension time-dependent Fluid-Kinetic (DyFK) model. The DyFK model simulates ionospheric plasma transport dynamics along a magnetic flux tube at high-latitude.

In every analyzed case, we started off by simulating many different convection trajectories.

The high-latitude ionospheric electric potentials or the convection trajectories used were based on the empirical ionospheric electric potential model [*Weimer*, 2001]. The Weimer trajectories include the effects of corotation and accept inputs of solar wind density, velocity, and interplanetary magnetic field (IMF) as its driving parameters. The convection trajectories were reverse convected backward for approximately 6 hours prior to the observation time.

Then we constructed a flux tube at the initial point of each of the trajectories. Each of the flux tubes and before convection reached a quasi-steady state.

To determine the auroral boundaries, we constrained the measurements from the Defense Meteorological Satellite Program (DMSP), Polar/HYDRA and Polar/TIDE. In the auroral region, two processes were present and incorporated in DyFK model every time the flux tube enters this region. For every flux tube and in all 4 cases, the two processes included the soft electron precipitation stream that was taken to be a streaming Maxwellian energy spectrum, with peak at 100 eV and the flux of the soft electron precipitation was taken to be 1 erg cm^{-2} s^{-1} at 800 km altitude The second process is the auroral electric field wave spectral density profile with the "benchmark" spectral density at 6.5 Hz selected to be 0.3×10^{-6} V^2 m^{-2} Hz^{-1}, and the Broad-Band Extreme Low-Frequency BBELF wave power spectral index was 1.7. We note that the wave spectral density parameter was used in all the DyFK simulation through this dissertation simulation work.

6.2 Conclusions

The investigated cases showed different results, 3 out of 4 cases of O^+ density simulation results showed a reasonable agreement with the observations, the three cases are for the following dates August 20 1998, August 02 1998, June 26 1998.

In the 3 cases there were discrepancies with few points with the observed O^+ density. However, the simulated troughs were in a reasonable agreement with the observed troughs. Possible reasons for the discrepancy are the real flux tube convection history intersecting with the Polar track may actually did (didn't) pass through the auroral oval earlier and for longer period of time than the simulated one. Although the Ovation auroral oval was not adjusted and/or the electric field pattern was modified, the Ovation auroral oval maybe did not present the actual boundaries for the real auroral region at the time of Polar pass. Other possibility, the Weimer trajectories were not accurate for the time of observations. The fourth case simulation results had a strong disagreement with the observations. We can conclude that for the above reasons, it could be the trough in this case was temporal not spatial, and the processes that produced such depletion might be different of what we referred to earlier.

As we concluded, in the polar cap, the principal competing processes controlling the O^+ density levels at the ionosphere-magnetosphere coupling region altitudes are first the auroral processes, which elevate the O^+ densities in the ~6000 km altitude region, besides the effects of *F* region O^+-electron recombination in darkness which decrease the O^+ densities at higher altitudes through draining to the reduced *F* region ionosphere.

6.3 Summary of Results of Electron Energization by Alfvén Waves and Its Effects on Auroral Ionospheric Plasma Transport

In the auroral region Alfvén waves have been observed and their effects on the ionosphere-magnetosphere region. Alfvén waves under certain conditions generate a field-aligned parallel electric field $E_{||}$ and precipitating electrons in the auroral region can be occasionally associated with Alfvén parallel electric field. Studies of dispersive Alfvén waves showed that these waves accelerate electrons down toward the ionosphere region which drives the electron acceleration downward. These electrons might experience burst events when their velocities exceed Alfvén phase speed.

The second part of this dissertation was the search for the mechanisms that contribute to O^+ ion outflow through the interaction of Alfvén waves with the ionosphere-magnetosphere plasma.

Also, we explored the behavior and the effects of continuous Alfvén wave propagation with its associate parallel electric field through simulation. The simulation started by generating a density profile of O^+, H^+ and e^- which successfully reproduced field-aligned electron resonance/burst along with the propagation of Gyro-Fluid Alfvén wave. This profile allowed for a certain properties of Alfvén waves where its Poynting flux and phase speed profile controlled the process of the downward electron precipitation and electron burst event occurrence and intensity. This study showed the effect of produced parallel electric field on the evolution of the magnetosheath electrons by applying test particle method. Then we explored the subsequent evolution of O^+ ions densities and their outflows development in the ionosphere-magnetosphere region by employing the three models working in iteration. The process was based on the calculations of the base moments of the precipitating electrons using the test particle method. We assigned different temperatures for accelerated electrons in this code that evolved with their phase space distributions. The different electron temperatures with 10, 20, 30, 40 eV and higher

gave different results. We showed for given plasma density, limited groups of magnetosheath electrons would be affected by the generated Alfvén wave.

Linking the three models together was not self consistent, but allowed us to study the effects of the Alfvénic electrons precipitations on the existing density profile and the follow the evolving of Alfvén wave properties such as the Alfvén phase speed profiles.

6.4 Conclusions

The simulation results showed that, the electrons precipitations along with the wave heating incorporated in the DyFK model increased the O^+ ion out flows and densities along the magnetic field line. The development of density structures and loading the magnetosphere with mass created the conditions for flattened Alfvén speed profile, which enhanced electron acceleration. This property allowed a wider region for electron acceleration. However, the increased mass in the surrounding plasma also lead to increase in $E_{||}$ magnitude but mostly for magnetosheath electrons with high temperature > 30 eV.

In Summary, we were successfully able to link the DyFK, Gyro-Fluid and the test particle models to produce physical results. The propagating Alfvén waves in a fixed flux tube caused continuous increase in the O^+ outflow. This lead to evolution in phase speed, as the O^+ densities increased the Alfvén waves become slower and its profiles became more flat promoting wider region of electron acceleration.

6.5 Future Work

The DyFK model was able to explore the effects of the auroral and nominal polar cap processes which lead to either normal or trough O^+ density and replicated the Polar/TIDE observations for much of the Polar pass density distributions. However, as for case four, a sharp discrepancy had occurred and the simulation could not explain it. On the other hand, the H^+ ion simulation results were also not consistent with the observations (wasn't shown in

chapter 2), which indicates an association with O^+ density troughs. However, the H^+ density simulations did not result in such structures.

Our goal for the future is the explore more mechanisms that might be involved in O^+ and H^+ out flow and incorporate in the simulation models that are involved.

Also based on the work of Alfvén wave simulation, we were able to link the three models, the DyFK, Gyro-Fluid and the test particle method, but that was in non self consistent way. One of the goals for research in Alfvén wave arena is to link these three models self consistently, where we expect to have more simulation results in agreement with observations, and be able to explain different phenomenon that are linked to Alfvén waves dynamics.

REFRENCES

Abe, T., A. Whalen, A. W. Yau, R. E. Horita, S Watanabe, E. Sagawa (1993), EXOS D (Akebono) Superthermal mass spectrometer observations of the polar wind, *J. Geophys. Res.,* 98, 11,191.

Aikio, A. T., L. G. Blomberg, G. T. Marklund, and M. Yamauchi (1996), On the origin of the high-altitude electric field fluctuations in the auroral zone, *J. Geophys. Res*., 101(A12), 27,157–27,170.

Arnoldy, R. L., M. J. Engebretson, J. L. Alford, R. E. Erlandson, and B. J. Anderson (1996), Magnetic impulse events and associated Pc 1 bursts at dayside high latitudes, *J. Geophys. Res.*, 101(A4), 7793–7799.

Andersson, L., N. Ivchenko, J. Clemmons, A. A. Namgaladze, B. Gustavsson, J.-E. Wahlund, L. Eliasson, and R. Y. Yurik (2002) Electron signatures and Alfvén waves, *J. Geophys. Res.,* 107(A9), 1244, doi:10.1029/2001JA900096.

Andre, M., and A. W. Yau (1997), Theories and observations of energization and outflow in the high latitude magnetosphere, Space Sci. Rev., 80, 27. Brown, S. R., H. W. Stockman, and S. J. Reeves (1995), Applicability of the Reynolds Equation for modeling fluid flow between rough surfaces, *Geophys. Res. Lett*., 22(18), 2537–2540.

Axford, W. I.(1968), The polar wind and the terrestrial helium budget, *J. Geophys. Res*., 73, 6855.

Beer, M. A., and G. W. Hammett (1996), Toroidal gyrofluid equations for simulations of tokamak turbulence, *Phys. Plasma*, 3, 4046.

Boehm, M. H., C. W. Carlson, J. P. McFadden, J. H. Clemmons, and F. S. Mozer (1990), High-Resolution Sounding Rocket Observations of Large-Amplitude Alfvén Waves, *J. Geophys. Res.*, 95(A8), 12,157–12,171.

Brown, D. G., J. L. Horwitz, and G. R. Wilson (1995), Synergistic Effects of Hot Plasma-Driven Potentials and Wave-Driven Ion Heating on Auroral Ionospheric Plasma Transport, *J. Geophys. Res.,* 100(A9), 17,499–17,514.

Carlson, C. W., et al. (1998), FAST observations in the downward auroral current region: Energetic upgoing electron beams, parallel potential drops, and ion heating, *Geophys. Res. Lett.,* 25(12), 2017–2020.

Chandler, M. O., J. H. Waite Jr., and T. E. Moore (1991), Observations of Polar Ion Outflows, *J. Geophys. Res.*, 96(A2), 1421–1428.

Chandler, M. O. (1995), Observations of Downward Moving O+ in the Polar Topside Ionosphere*, J. Geophys. Res*., 100(A4), 5795–5800.

Chandler, M. O., S. A. Fuselier, M. Lockwood, and T. E. Moore (1999), Evidence of component merging equatorward of the cusp, *J. Geophys. Res.,* 104(A10), 22,623–22,633.

Chandler, M. O., and T. E. Moore (2003), Observations of the geopause at the equatorial magnetopause: Density and temperature, *Geophys. Res. Lett*., 30(16), 1869, doi:10.1029/2003GL017611.

Chappell, C. R., T. E. Moore, and J. H. Waite Jr. (1987), The Ionosphere as a Fully Adequate Source of Plasma for the Earth's Magnetosphere, *J. Geophys. Res*., 92(A6), 5896–5910.

Chaston, C. C., C. W. Carlson, W. J. Peria, R. E. Ergun, and J. P. McFadden (1999), FAST observations of inertial Alfvén waves in the dayside aurora, *Geophys. Res. Lett*., 26, 647.

Chaston, C. C., C. W. Carlson, R. E. Ergun, and J. P. McFadden (2000), Alfvén waves, density cavities and electron acceleration observed from the FAST spacecraft, *Phys. Scr*., T84, 64.

Chaston, C. C., J. W. Bonnell, C. W. Carlson, M. Berthomier, L. M. Peticolas, I. Roth, J. P. McFadden, R. E. Ergun, and R. J. Strangeway (2002a), Electron acceleration in the ionospheric Alfvén resonator, *J. Geophys. Res*., 107(A11), 1413, doi:10.1029/2002JA009272.

Chaston, C. C., J. W. Bonnell, L. M. Peticolas, C. W. Carlson, J. P. McFadden, and R. E. Ergun (2002b), Driven Alfvén waves and electron acceleration: A FAST case study, *Geophys. Res. Lett.,* 29(11), 1535, doi:10.1029/2001GL013842.

Chaston, C. C., J. W. Bonnell, C. W. Carlson, J. P. McFadden, R. J. Strangeway, and R. E. Ergun (2003), Kinetic effects in the acceleration of auroral electrons in small scale Alfvén waves: A FAST case study, *Geophys. Res. Lett*., 30(6), 1289, doi:10.1029/2002GL015777.

Chaston, C. C., J. B. Bonnell, C. W. Carlson, J. P. McFadden, R. E. Ergun, and E. J. Lund (2004), Ion acceleration in dispersive Alfvén waves, *J. Geophys. Res*., 109, A04205, doi:10.1029/2003JA010053.

Clark, A. E., and C. E. Seyler (1999), Electron beam formation by small-scale oblique inertial Alfvén waves, J*. Geophys. Res*., 104, 17,233.

Craven, P. D., D. L. Gallagher, and R. H. Comfort (1997), Relative concentration of He+ in the inner magnetosphere as observed by the DE 1 retarding ion mass spectrometer, *J. Geophys. Res.*, 102(A2), 2279–2289.

Crew, G. B., T. Chang, J. M. Retterer, W. K. Peterson, D. A. Gurnett, and R. L. Huff (1990), Ion cyclotron resonance heated conics: theory and observations, *J. Geophys. Res*., 95, 3959.

Estep, G. M., J. L. Horwitz, Y.,-J. Su, P. G. Richards, G. R. Wilson, and D. G. Brown (1999), A dynamic fluid-kinetic model for ionosphere-magnetosphere plasma transport: Effects of ionozation and thermal electron heating by soft electron precipitation, *Terr. Atmos. Oceanic Sci.,* 10, 491-510.

Ganguli, S. B., H. G. Mitchell, and P. J. Palmadesso (1994), Auroral Plasma Transport Processes in the Presence of kV Potential Structures, *J. Geophys. Res*., 99(A4), 5761–5770.

Ganguli, S. B., (1996), The polar wind, *Rev. Geophys*., 34, 311.

Goertz, C. K., and R. W. Boswell (1979), Magnetosphere-ionosphere coupling, J. *Geophys. Res*., 84, 7239.

Hallinan, T., et al., Relation between optical emissions, particles, electric fields, and Alfvén waves in a multiple rayed arc (2001), *J. Geophys. Res*, 106, 15,445.

Hasegawa, A. (1976), Particle acceleration by MHD surface wave and formation of aurora, *J. Geophys. Res*., 81, 5083.

Heelis, R. A., and W. R. Coley (1992), East-West Ion Drifts at Mid-Latitudes Observed by Dynamics Explorer 2, J. Geophys. Res., 97(A12), 19,461–19,469.

Ho, C. W., J. L. Horwitz, N. Singh, G. R. Wilson, and T. E. Moore (1992), Effects of Magnetospheric Electrons on Polar Plasma Outflow: A Semikinetic Model, *J. Geophys. Res*., 97(A6), 8425–8437.

Ho, C. W., J. L. Horwitz, and G. R. Wilson (1997), Dynamics of the H^+ and O^+ polar wind in the transition region as influenced by ionospheric convection and electron heating, *J. Geophys. Res.*, 102(A1), 395–406.

Horita, R. E., A. W. Yau, B. A. Whalen, T. Abe, and S. Watanabe (1993), Ion depletion zones in the polar wind: EXOS D superthermal ion mass spectrometer observations in the polar cap, *J. Geophys. Res*., 90, 11,439.

Horwitz, J. L., C. R. Baugher, C. R. Chappell, E. G. Shelley, and D. T. Young (1982), Conical Pitch Angle Distributions of Very Low-Energy Ion Fluxes Observed by ISEE 1, *J. Geophys. Res.*, 87(A4), 2311–2320.

Horwitz, J. L., and M. Lockwood (1985), The Cleft Ion Fountain: A Two-Dimensional Kinetic Model, *J. Geophys. Res*., 90(A10), 9749–9762.

Horwitz, J. L. (1987), Parabolic Heavy Ion Flow in the Polar Magnetosphere, *J. Geophys. Res*., 92(A1), 175–185.

Horwitz, J. L, C. J. Pollock, T. E. Moore, W. K. Peterson, J. L. Burch, J. D. Winningham, J. D. Craven, L. A. Frank, and A. Persoon (1992), The polar cap environment of outflowing O^+, *J. Geophys. Res*., 8361.

Horwitz, J. L., C. W. Ho, H. D. Scarbo, G. R. Wilson, and T. E. Moore (1994), Centrifugal acceleration of the polar wind, *J. Geophys. Res*., 99, 15,051.

Horwitz, J. L., C. W. Ho, H. D. Scarbro, G. R. Wilson, and T. E. Moore (1994), Centrifugal Acceleration of the Polar Wind, *J. Geophys. Res*., 99(A8), 15,051–15,064.

Horwitz, J. L. (1995), The ionosphere's wild ride in outer space, *Rev. Geophys*., 33, 703.

Horwitz, J. L., and T. E. Moore (1997), Four contemporary issues concerning ionospheric plasma flow to the magnetosphere, *Space Sci. Rev*., 80, 49.

Ivchenko, N., G. Marklund, K. Lynch, D. Pietrowski, R. Torbert, F. Primdahl, and A. Ranta (1999), Quasiperiodic oscillations observed at the edge of an auroral arc by auroral turbulence 2, *Geophys. Res. Lett*., 26(22), 3365–3368.

Jaafari, F., J. L. Horwitz, and W. Zeng (2008), Simulation of the formation of O^+ density troughs at 6000 km altitude in the polar cap ionosphere-magnetosphere region, *J. Geophys. Res.*, 113, A07207, doi:10.1029/2007JA012690.

Jones, S. T., and S. E. Parker (2003), Including electron inertia without advancing electron flow, *J. Comput. Phys*., 191, 322.

Jones, S. T. (2004), Gyrofluid simulation of Alfvén waves in the magnetosphere and ionosphere, Ph.D. dissertation, Dep. of Phys., Univ. of Colo., Boulder, Colo.

Kivelson, M. G and C.T. Russell (1997). Introduction to Space Physics. Cambridge University Press.

Kletzing, C. A., and S. Hu (2001), Alfvén wave generated electron time dispersion, *Geophys. Res. Lett.*, 28, 693.

Knudsen, D. J., M. C. Kelley, and J. F. Vickrey (1992), Alfvén Waves in the Auroral Ionosphere: A Numerical Model Compared with Measurements, *J. Geophys. Res.,* 97(A1), 77–90.

Knudsen, D. J. (1996), Spatial modulation of electron energy and density by nonlinear stationary inertial Alfvén waves, *J. Geophys. Res*., 101(A5), 10,761–10,772.

Knudsen, D. J., B. A. Whalen, T. Abe, and A. Yau (1998), Temporal evolution and spatial dispersion of ion conics: Evidence for a polar cusp heating wall, in Solar System Plasmas in Space and Time, *Geophys. Monogr. Ser*., vol. 84, edited by J. L. Burch and J. H. Waite Jr., p. 163, AGU, Washington, D. C.

Lemaire, J. (1972),Effect of escaping photoelectrons in a polar exospheric model, *Space Res.,* 12, 1413.

Lemaire, J., and K. I. Gringauz (1998), The earth's plasmasphere, Cambridge Univ. Press, Cambridge.

Lepping, R. P., M. Acuna, L. Burlaga, W. Farrel, J. Salvin, K. Schatten, F. Mariani, N. Ness, FNeubauer, Y. C. Whang, J. Byrnes, R. Kennon, P. Penetta, J. Scheifele, and E. Worley (1995), The WIND magnetic field investigation, *Space Sci. Rev*., 71, 207.

Loranc, M., W. B. Hanson, R. A. Heelis, and J. .-P. St.-Maurice (1991), A Morphological Study of Vertical Ionospheric Flows in the High-Latitude F Region, *J. Geophys. Res*., 96(A3), 3627–3646.

Lotko, W., A. Streltsov, and C. W. Carlson (1998), Discrete auroral arc, electrostatic shock and suprathermal electrons powered by dispersive, anomalously resistive field line resonance, *Geophys. Res. Lett*., 25, 4449.

Louarn, P., J. E. Wahlund, T. Chust, H. de Feraudy, A. Roux, B. Holback, P. O. Dovner, A. I. Eriksson, and G. Holmgren (1994), Observation of kinetic Alfvén waves by the FREJA spacecraft, *Geophys. Res. Lett*., 21(17), 1847–1850.

Lysak, R. L., and C. W. Carlson (1981), The effect of microscopic turbulence on magnetosphere-ionosphere coupling, *Geophys. Res. Lett*., 8, 269.

Lysak, R. L., and W. Lotko (1996), On the kinetic dispersion relation for shear Alfvén waves, J. Geophys. Res., 101, 5085.

Lysak, R. L. (1998), Comment on “Theory of nearly perpendicular electrostatic plasma waves and comparison to Freja satellite observations” by C. E. Seyler and J.-E. Wahlund, *J. Geophys. Res*., 103(A4), 7043–7047.

Moore, T. E., C. R. Chappell, M. Lockwood, and J. H. Waite (1985), Superthermal ion signatures of auroral acceleration processes, *J. Geophys. Res*., 90(A2), 1611-1618.

Moore, T. E., M. Lockwood, M. O. Chandler, J. H. Waite Jr., C. R. Chappell, A. Persoon, and M. Sugiura (1986), Upwelling O+ Ion Source Characteristics, *J. Geophys. Res*., 91(A6), 7019–7031.

Moore, T. E., et al. (1995), The thermal ion dynamics experiment and plasma source instrument, *Space Sci. Rev*., 71, 409.

Moore, T. E., M. O. Chandler, C. J. Pollock, D. L. Reasoner, R. L. Arnoldy, B. Austin, P. M. Kintner, and J. Bonnell (1996), Plasma heating and flow in an auroral arc*, J. Geophys. Res.,* 101(A3), 5279–5297.

Mitchell, H. G., Jr., S. B. Ganguli, and P. J. Palmadhesso (1992), Diodelike Response of High-Latitude Plasma in Magnetosphere-Ionosphere Coupling in the Presence of Field-Aligned Currents, *J. Geophys. Res*., 97(A8), 12,045–12,056.

Newell, P. T., Yasha I.Feldstein, Yuri I. Galperin, and Ching-I. Meng (1996), Morphology of nightside precipitation, *J. Geophys. Res*., 96, 10,737-10,748.

Newell, P. T., T. Sotirelis, J. F. Carbary, K. Liou, J. P. Skura, C. –I. Meng, C. Deehr, D. W.lkinson, and F. J. Rich (2002), OVATION: oval variation, assessment tracking, intensity, and on line nowcasting, *Ann. Geophy.*, 20, 1039-1074.

Norqvist, P., M. Andre, and M. Tyrland (1998), A statistical study of ion energization mechanisims in the auroral region, *J. Heophys. Res*., 103, 23, 459-23,474.

Nsumei, P. A., X. Huang, B. W. Reinisch, P. Song, V. M. Vasyliunas, J. L. Green, S. F. Fung, R. F. Benson, and D. L. Gallagher (2003), Electron density distribution over the northern polar region deduced from IMAGE/radio plasma imager sounding, *J. Geophys. Res.,* 108(A2), 1078, doi:10.1029/2002JA009616.

Ogilvie, K. W., D. J. Chorney, R. J. Fitzenreiter, F. Hunsaker, J. Keller, J. Lobell, G. Miller, J. D. Scudder, E. C. Sittler Jr., R. B. Torbert, D. Bodet, G. Needel, A. J. Lazarus, J. T. Steinberg, J. H. Tappan, A. Mavretic, and E. Gergin (1995), SWE, a comprehensive plasma instrument for the WIND spacecraft, *Space Sci. Rev*., 71, 55.

Pierrard, V., and J. Lemaire (1998), A collisional kinetic model of the polar wind, *J. Geophys. Res.,* 103(A6), 11,701–11,709.

Pfaff, R., et al. (1998), Initial FAST observations of acceleration processes in the cusp, *Geophys. Res. Lett*., 25(12), 2037–2040.

Reiff, P. H., T. W. Hill, and J. L. Burch (1977), Solar Wind Plasma Injection at the Dayside Magnetospheric Cusp, *J. Geophys. Res*., 82(4), 479–491.

Rich, F. J.,and M. Hairston (1994), Large-scale convection patterns observed by DMSP,*J. Geophys. Res.*, 99, 3827.

Richards, P. G., and D. G. Torr (1990), Auroral modeling of the 3371 A emission rate: Dependence on characteristic electron energy, *J. Geophys. Res*., 95, 10,337.

. Richards, P. G., D. G. Torr, M. E. Hagan, and M. J. Buonsanto (1995), A new algorithm for improved ionospheric electron density modeling*, Geophys. Res. Lett*., 22(11), 1385–1388.

Russell, C. T., G. L. Siscoe, and E. J. Smith, Comparison of ISEE-1 and -3 interplanetary magnetic field observations (1980), *Geophys. Res. Lett*., 7, 381-384.

Schunk, R. W., and J. J. Sojka (1989), A three dimensional time dependent model of the polar wind , *J. Geophys. Res*., 94, 8973.

Schunk, R. W., and J. J. Sojka, (1997), Global ionosphere-polar wind system during changing magnetic activity, *J. Geophys. Res*., 11,625.

Scudder, J., et al. (1995), A 3-dimensional electron and ion hot plasma instrument for the polar spacecraft of the GGS mission, *Space Sci. Rev*, 71, 459-495.

Shelley, E. G., W. K. Peterson, A. G. Ghielmetti, and J. Geiss (1982), The polar ionosphere as a source of energetic magnetospheric plasma, *Geophys. Res. Lett*., 9(9), 941–944.

Seo, Y., R. Caton, and J. L. Horwitz. (1997), Statistical relationships between High- latitude ionospheric F region/topside upflows and their drivers: DE-2 observations, J. Geophys. Res., 102, 7439.

Sojka, J. J, R. W. Schunk, M. D. Bowline, J. Chen, S. Slinker, and J. Fedder (1997), Driving a physical ionosphereic model with magnetospheric MHD model. *J. Geophys. Res.,* 22,209-22,220.

Stasiewicz, K., G. Gustafsson, G. Marklund, P.-A. Lindqvist, J. Clemmons, and L. Zanetti (1997), Cavity resonators and Alfvén resonance cones observed on Freja, *J. Geophys. Res.*, 102(A2), 2565–2575.

Stasiewicz, K., et al. (2000), Small scale Alfvénic structure in the aurora, *Space Sci. Rev*., 92, 423.

Stevenson, B., A. J. L. Horwitz, G. Germany, T. E. Moore, B. L. Giles, P. D. Craven, M. O. Chandler, Y.-J. Su, G. K. Parks (2001), Polar observations of the topside field-alighed O^+ flows and auroral forms, *J. Geophys. Res*., 106, 18, 969-18, 979.

Streltsov, A. V., W. Lotko, J. R. Johnson, and C. Z. Cheng (1998), Small-scale, dispersive field line resonances in the hot magnetospheric plasma*, J. Geophys. Res*., 103, 26,559.

Su, Y-J., J., L. Horwitz, G. R. Wilson, P. G. Richards, D. G. Brown, and C. W. Ho (1998a), Self-consistent simulation of the photoelectron-driven polar wind from 120 km to 9 R_E altitude, *J. Geophys. Res*., 103, 2279.

Su, Y-J., J., L. Horwitz, T. E. Moore, B. L. Giles, M. O. Chandler, P. D. Craven, M. Hirahrara, C. J. Pollock (1998b). Polar wind survey with the thermal ion dynamics experiment/plasma source instrument suite aboard Polar. *J. Geophys. Res*., 103, 29,305-29,337.

Su, Y-J., J. L. Horwitz, G. R. Wilson, and P. G. Richards (1999), Systematic modeling of soft-electron precipitation effects on high-latitude F region and topside ionospheric upflows, *J. Geophys. Res*., 104, 153.

Su, Y.-J., R. E. Ergun, W. K. Peterson, T. G. Onsager, R. Pfaff, C. W. Carlson, and R. J. Strangeway (2001), Fast Auroral Snapshot observations of cusp electron and ion structures, *J. Geophys. Res*., 106, 25,595.

Su, Y.-J., R. E. Ergun, F. Bagenal, and P. A. Delamere (2003), Io-related Jovian auroral arcs: Modeling parallel electric fields, *J. Geophys. Res*., 108(A2), 1094, doi:10.1029/2002JA009247.

Su, Y.-J., S. T. Jones, R. E. Ergun, and S. E. Parker (2004), Modeling of field-aligned electron bursts by dispersive Alfvén waves in the dayside auroral region, *J. Geophys. Res*., 109, A11201, doi:10.1029/2003JA010344.

Su, Y.-J., S. T. Jones, R. E. Ergun, F. Bagenal, S. E. Parker, P. A. Delamere, and R. L. Lysak (2006), Io-Jupiter interaction: Alfvén wave propagation and ionospheric Alfvén resonator, *J. Geophys. Res*., 111, A06211, doi:10.1029/2005JA011252.

Tam, S. W., Y., F. Yasseen, and T. Chang (1995), Self-consistent kinetic photoelectron effects on the polar wind*, Geophys. Res. Lett*., 22, 2107.

Thompson, B. J., and R. L. Lysak (1996), Electron acceleration by inertial Alfvén waves, *J. Geophys. Res.*, 101, 5359.

Tsunoda, R. T., R. C. Livingston, J. F. Vickrey, R. A. Heelis, W. B. Hanson, F. J. Rich, and P. F. Bythrow (1989), Dayside Observations of Thermal-Ion Upwellings at 800-km Altitude: An Ionospheric Signature of the Cleft Ion Fountain*, J. Geophys. Res*., 94(A11), 15,277–15,290.

Tu, J.-N, J. L. Horwitz, P. A. Nsumi, P. Song, X.-Q. Huang, and B. W. Reinisch (2004a). Simulation of polar cap field-aligned electron density profiles measured with IMAGE Radio plasma Imager, *J. Geophys. Res*., 109, A07206, doi:10,1029/2003JA010310.

Tu, J.-N., J. L. Horwitz, and T. E. Moore (2005). Simulating cleft ion fountain at Polar perigee altitudes, J. Atmos. *Solar-Terr. Phys*., 67, 465-477.

Wahlund, J.-E., et al. (1994), Observations of ion acoustic fluctuations in the auroral topside ionosphere by the FREJA S/C, *Geophys. Res. Lett*., 21(17), 1835–1838.

Wahlund, J.-E., P. Louarn, T. Chust, H. de Feraudy, A. Roux, B. Holback, P□O. Dovner, and G. Holmgren (1994), On ion acoustic turbulence and the nonlinear evolution of kinetic Alfvén waves in aurora, *Geophys. Res. Lett*., 21(17), 1831–1834.

Waite, J. H., Jr., T. Nagai, J. F. Johnson, C. R. Chappel, J. L. Burrch, T. L. Killeen, P. B. Hays, G. R. Carigan, W. K. Peterson, and E. G. Shelly (1985). Escape of superthermal O^+ ions in the polar cap, *J. Geophys. Res*., 90, 1619.

Weimer, D.R. (2001), An improved model of ionospheric electric potential including substorm perturbations and application to the Geospace Environment Modeling November 24 1996, event*, J. Geophys. Res*.,106, 407.

Wilson, G. R. (1992), Kinetic modeling of O^+ upflow of ionospheric plasma through the topside collisional to collisionless transition region*, J. Geophys. Res*., 97, 10,551.

Wilson, G. R. (1994), Kinetic modeling of O^+ upflows resulting from ExB convection heating in the high-latitude F region ionosphere*, J. Geophys. Res* , 99, 17,453.

Whitteker, J. H.(1997), The transient response of the topside ionosphere to precipitation, *Space Sci.*, 25, 773.

Wu, X.-Y., J. L. Horwitz, G. M. Estep, Y.-J. Su, D. G. Brown, P. G. Richards, and G. R. Wilson (1999), Dynamic fluid-kinetic (DyFK) modeling of auroral plasma outflow driven by soft electron precipitation and transverse ion heating, *J. Geophys. Res*, Vol. 104, 17,263.

Wu, X.-Y., J. L. Horwitz, and Y. Seo (2000), Statistical analysis of F region and topside ionospheric ion field-aligned flows at high latitudes, *J. Geophys. Res*., 105(A2), 2477–2494.

Wu, X.-Y., J. L. Horwitz, and J.-N. Tu (2002), Dynamic Fluid Kinetic (DyFK) simulation of auroral ion transport: Synergistic effects of parallel potentials, transverse ion heating, and soft electron precipitation, *J. Geophys. Res*, Vol. 107, No. A10, 1283, doi:10.1029/2000JA000190.

Wygant, J. R., et al., Polar spacecraft based comparisons of intense electric fields and Poynting flux near and within the plasma sheet tail lobe boundary to UVI images: An energy source for the aurora (2000), *J. Geophys. Res*., 105, 18,675.

Yamauchi, M., et al. (1996), Dynamic response of the cusp morphology to the solar wind: A case study during passage of the solar wind plasma cloud on February 21, 1994*, J. Geophys. Res.*, 101(A11), 24,675–24,687.

Yau, A.W., B. A. Whalen, T. Abe, T. Mukai, K. I. Oyama, and T. Chang (1995), Akebono observations of electron temperature anisotropy in the polar wind, *J. Geophys. Res*., 100, 17, 451.

Young, E. R., D. G. Torr, P. Richards, and A. F. Nagy (1980), A computer simulation of the midlatitude plasmasphere and ionosphere, *Planet. Space Sci.*, 28, 881.

Zeng, W., J. L. Horwitz, P.D. Craven, F. J. Rich, and T. E. Moore (2004), The O^+ density trough at 5000 km altitude in the polar cap, *J. Geophys. Res.,* 109, A03220, doi:10.1029/2003JA010210.

BIOGRAPHICAL INFORMATION

Fajer Jaafari born Fajer Bitar in the late sixties is the second of her five siblings, all girls. Her dad an electrical and Mechanical engineer that worked for British Oil Company IPC. Her Mom a dedicated homemaker.

Fajer's love of science propelled her to pursue a Bachelors of Science degree that combined physics, chemistry and math, in her native country Syria. She met her future husband while vacationing in Petra Jordan in 1992, later joined him in her new homeland in the states. They resided both in Tulsa Oklahoma, had two children Hana and Deena. In the late nineties, her husband aspired to move back to the state of Texas as he practiced engineering with the city of Fort Worth. Fajer enrolled at the University of Texas in Arlington to pursue higher education in physics. She attained a master's degree in high energy and later enrolled in space physics for her Doctoral degree. All along higher powers intervened and her family expanded with the additions of Rami and Selma.